Transport of Protonic Charge Carriers in Methyl-Sulfonic-Acid / Water Mixtures: A Model for Lowly Hydrated Sulfonic Acid Based Ionomers

Dissertation

Von der Fakultät Mathematik und Physik der Universität Stuttgart zur Erlangung der Würde eines Doktors der Naturwissenschaften (Dr. rer. nat.) genehmigte Abhandlung

Vorgelegt von

Ahmad D. S. Telfah

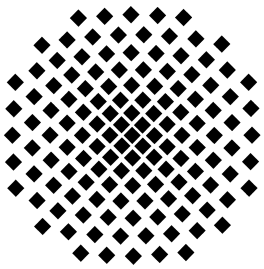

Universität Stuttgart
2008

Transport of Protonic Charge Carriers in Methyl-Sulfonic-Acid / Water Mixtures: A Model for Lowly Hydrated Sulfonic Acid Based Ionomers

Von der Fakultät Mathematik und Physik der Universität Stuttgart zur Erlangung der Würde eines Doktors der Naturwissenschaften (Dr. rer. nat.) genehmigte Abhandlung

Vorgelegt von

Ahmad D. S. Telfah

geboren in Juhfieh-Irbid, Jordanien

Hauptberichter	Priv. Doz. Dr. G. Majer
Mitberichter	Prof. Dr. D. Schweitzer
Mitberichter	Priv. Doz. Dr. K.-D. Kreuer

Tag der Einreichung: 02.06.2008
Tag der mündlichen Prüfung: 18.07.2008

Max-Planck-Institut für Metallforschung, Stuttgart

Max-Planck-Institut für Festkorperforschung, Stuttgart

2008

Contents

Abbreviations and Symbols 5

Kurzfassung 13

Abstract 15

1 Introduction 17

2 NMR Theory 21

2.1 Fundamentals of NMR 21
2.1.1 Origin of Nuclear Magnetization 21
2.1.2 Boltzmann Distribution 22
2.1.3 Description of Spin Motion and Bloch Equation 26
2.1.4 Free Induction Decay (FID) and NMR-Signal 27
2.1.5 Chemical Shift 28

2.2 Relaxation Mechanisms 29
2.2.1 Spin-Lattice Relaxation 29
2.2.2 Spin-Spin Relaxation Rate 33
2.2.3 Motional Narrowing 34

2.3 Pulsed Field Gradient NMR 35
2.3.1 NMR Self-Diffusion and Magnetic Gradients as Spatial Labels 35
2.3.2 Spin Echos 37
2.3.3 Bloch Equation Including Diffusion 38
2.3.4 Measuring Diffusion with Magnetic Field Gradients 40

3 Proton Conductivity and Proton Transport Mechanisms 45

3.1 Formation of Protonic Charge Carriers 45

3.2 Dielectric Constant in Dipolar Liquids 48

3.3 Mobility of Protonic Charge Carriers 48

3.4 Proton Transport Mechanisms 50

4 Experimental Section 53

4.1 Experimental Setups 53
4.1.1 NMR Spectrometer 53
4.1.2 PFG-NMR Spectrometer 54
4.1.3 High Resolution NMR Spectrometer 58
4.1.4 AC-Impedance Analyzer 58
4.1.5 Conductivity Cell for Liquids 58

4.1.6 Conductivity Cell for Membranes 59
4.1.7 Thermogravimetric Analysis (TGA) Spectrometer 61
4.2 Samples Preparation 63
4.2.1 NMR Samples 63
4.2.2 High Resolution NMR Samples 63
4.2.3 Conductivity Samples (Liquids and Membranes) 63
4.2.4 TGA Samples 64
4.3 Experimental Details 65
4.3.1 Spin-Echo Experiment with Pulsed Magnet Field Gradients 65
4.3.2 Spin-Lattice Relaxation Time (T_1) Measurement 66
4.3.3 Conductivity Measurements 68
4.3.4 Thermogravimetric Analysis (TGA) Measurement 72

5 Results and Discussion 73

5.1 MSA-Water System 73
5.1.1 ^{1}H-NMR Spectrum of Pure MSA and MSA-Water Mixtures 73
5.1.2 MSA Dissociation and Formation of the Protonic Charge Carriers $H^+(H_2O)_n$ 76
5.1.3 Proton Diffusion 93
5.1.4 Proton Conductivity Mechanism 99

6 Summary and Conclusions 103

Appendix 108

References 121

Abbreviations and Symbols

PEM-FCs	Polymer-electrolyte-membrane fuel cells
SO_3H	Sulfonic acid group
H_2SO_4	Sulfuric acid
CH_3SO_3H	Methanesulfonic acid
MSA	Methanesulfonic acid
$H^+(H_2O)_n$	Protonated water clusters (protonic charge carriers)
NMR	Nuclear magnetic resonance
PFG-NMR	Pulsed Filed Gradient NMR
TGA	Thermo Gravimetric Analyzer
χ	Magnetic susceptibility
μ_n	Nucleus magneton
$\hbar$	Reduced Planck constant $\hbar = \frac{h}{2\pi} \simeq 1.0547 \times 10^{-34}\,\mathrm{J \cdot s}$
m_p	Proton mass, 1.6726×10^{-27} kg
e	Elementary charge = $1.602\,176\,487 \times 10^{-19}$ coulombs
I	Spin number
μ	Magnetic moment of magnitude
γ	Nuclear gyromagnetic ratio
m_I	Spin state
B_0	External magnetic field in NMR
ΔE	The energy difference between the two allowable states of nuclei $\Delta E = \gamma \hbar B_0$.

ω_0	The resonance frequency in radians per second, or Larmor frequency
N^+	Population of the spin-up states
N^-	Population of the spin-down states
k_B	Boltzmann constant
T	The absolute temperature
r.f.	Radio frequency
CW	Continuous wave
M_0	The equilibrium magnetization
$\vec{B}$	A longitudinal field of amplitude B_0
$\overrightarrow{M}$	Nuclear magnetization
T_1	Spin lattice relaxation time constant
T_2	Spin-spin relaxation time constant
$M_{x,y}$	Magnetization component in x-y plane
B'	The extra field B' is caused by the field B_0 including an electric current in the electron cloud surrounding the
σ	Shielding constant (dimensionless number)
Γ_1	Spin lattice relaxation rate
BPP	Bloembergen, Purcell and Pound model
$\Gamma_{1,el}$	Electronic contribution in spin lattice relaxation rate
C_K	Korringa constant (frequency-independent)
$\Gamma_{1,quad}$	The quadruple relaxation rate
$\Gamma_{1,para}$	Paramagnetic relaxation rate
$\Gamma_{1,dip}$	Dipolar relaxation rate

$G^{(\mathrm{p})}$	Pair correlation functions
$J^{(\mathrm{p})}$	Spectral density functions
$P(r_{jk}(0),r_{jk}(t),t)$	Probability that a spin pair
$r_{jk}(0)$	A connection vector
$r_{jk}(t)$	Distance vector
$F_{jk}(p)$	A mathematical formulation of the dipole-dipole interaction
r_{jk}	Connecting vector between the spin carriers *j* and *k*
$Y_{2p}(\Omega_{jk})$	Normal spherical harmonics.
τ_d	Mean dwell time of the migration hydrogen atoms
M_2	Second moment of the dipole-dipole interaction
Γ_2	Spin-spin relaxation rate
$\Gamma_{2,inh}$	Inhomogeneous part of the spin-spin relaxation rate
$\Gamma_{2,hom}$	Homogeneous part of the spin-spin relaxation rate
PGSE	Pulsed field gradient spin echo
D	Self-diffusion coefficient
J	Particle flux
$c(r, t)$	Concentration in number of particle per unit volume
$P(r_o\|r, t)$	Conditional probability
S	The gradient coil constant
δ	Duration of the gradient pulse
G	Strength of the gradient
$M_+ = M_x + iM_y$	Complex magnetization
$\varphi_i(\tau)$	Phase shift

Δ	The time from the first gradient pulse a second gradient pulse
$P(\phi,2\tau)$	$P(\phi,2\tau)$ is the relative phase-distribution function.
$\psi(2\tau)$	Diffusion attenuating factor
H^+	Hydrogen ions
K_C	Acid dissociation constant
$[A^-]$	Molar concentration of the acidic ions
$[H^+]$	Concentration of hydrogen ions
[HA]	Concentration of undissociated acid.
a_{A^-}	Activities of A^+ dissociation component
a_{B^+}	Activities of B^- dissociation component
a_{BA}	Activities of AB dissociation component
K_a	Thermodynamics dissociation constant
f	Activity coefficients
f_{A^+}, f_{B^-}	Activity coefficients of the ions A^+, B^-
OH^-	Hydroxide group
H_3O^+	Hydronium ions
m_i	Ions molality
c_i	Ions concentrations
x_i	Mole fractions
z_i	Elementary charges
ε	Dielectric constant
P	The polarization of the dielectric, and E is the field intensity
F	Cavity field

$\nabla\mu$	Chemical potential gradient
$H_5O_2^+$	Zundel dihydronium ions
$H_7O_3^+$	Protonated trimer
Λ_m	Molar conductivity
κ	Ionic conductivity
c	Molar concentration
λ_+	The limiting molar conductivity of the cations
λ_-	The limiting molar conductivity of the anions
Λ_m^0	Independent migration of ions states
ν_+ , ν_-	Numbers of cations and anions per formula unit of electrolyte
T_g	Glass transition temperatures
VTF	Vogel–Tammann–Fulcher
T_o	Temperature at which the conductivity goes to zero
$\boldsymbol{F}$	Faraday's constant ($\boldsymbol{F}$ = $N_A e$)
Λ_m	Limiting molar conductivity
D_2O	Deuterium Oxide (heavy water)
$CDCl_3$	Deuterated chloroform
σ	Electrical conductivity
Z	The conductivity cell constant
A	Electrode surface area in the conductivity cell
L	The distance between the electrodes in the conductivity cell
$\boldsymbol{R}$ [Ω]	The measured resistance in the conductivity cell
H_a	The activation enthalpy

$n^{i}_{H_2O}$	Initial water mole number
n^{i}_{MSA}	Initial MSA mole number
x	The ratio of water mole number n_{H_2O} to the MSA mole number n_{MSA} ($x = n^{i}_{H_2O} / n^{i}_{MSA}$).
$CH_3SO_3^-$	MSA anion
pK_a	Acidity constant
K_c	Dissociation constant
H_{OH}	Protons in OH group
H_{CH_3}	Protons in CH_3 group
$C^{i}_{CH_3SO_3H}$	MSA initial concentration (added concentration)
$C^{i}_{H_2O}$	Water initial concentration (added concentration)
$C_{CH_3SO_3H}$	MSA concentration (after equilibrium)
C_{H_2O}	Water Concentration (after equilibrium)
$C_{H_3O^+}$	Hydronium ion concentration (after equilibrium)
$C_{CH_3SO_3^-}$	MSA anion concentration (after equilibrium)
$x^{i}_{H_2O}$	Initial water proton mole fraction
$x^{i}_{CH_3SO_3H}$	Initial MSA proton mole fraction
λ	Water molecule per sulfonic acid molecule ($\lambda = \frac{n^{i}_{H_2O}}{n^{i}_{SO_3H}}$)
X_{H2O}	water proton mole fraction (after equilibrium)
$X_{H_3O^+}$	Hydronium proton mole fraction (after equilibrium)
$X_{CH_3SO_3H}$	MSA proton mole fraction (after equilibrium)
$X_{CH_3SO_3^-}$	MSA anion proton mole fraction (after equilibrium)
V_m	Molar volumes

M_{H_2O}	Molecular weight of water
$M_{CH_3SO_3H}$	Molecular weight of MSA
$\delta^{H(OH)}_{Total}$	Total chemical shift of H in OH group
$\delta^{OH}_{H_3O^+}$	chemical shift of H in OH group of Hydronium ion
$\delta^{OH}_{H_2O}$	chemical shift of H in OH group of water
δ^{OH}_{MSA}	chemical shift of H in OH-group of MSA
$\delta^{H_{CH_3}}_{MSA}$	chemical shift of H in CH_3 group of MSA
$\delta^{H_{CH_3}}_{Total}$	Total chemical shift of H in CH_3 group
$H^+(H_2O)_n$	Protonic charge carriers
$D(H_{OH})$	Diffusion of proton in OH group
$D(H_{CH_3})$	Diffusion of proton in CH_3 group
S-C7	Heptyl-sulfonic acid

Kurzfassung

Polymer-Elektrolyt-Membran-Brennstoffzellen (PEM-FCs) liefern eine hohe Energiedichte und haben gegenüber anderen Brennstoffzellensystemen den Vorteil eines geringen Gewichtes und geringen Volumens. Modernste Separatormaterialien in PEM-PCs sind sulfonsäurefunktionalisierte Polymere, wie das perfluorierte Polymer Nafion. Die Eignung von protonenleitenden Materialien als Separator in einer bestimmten Brennstoffzelle hängt entscheidend von seinen Transporteigenschaften, seiner Haltbarkeit und seiner Reaktivität ab. Schwerpunkt dieser Arbeit sind daher die protonischen Transporteigenschaften und das Entstehen protonischer Ladungen. Aufgrund der Komplexität von protonenleitenden Materialien auf der Basis von Polymeren wurden in dieser Arbeit Mischungen aus Methylsulfonsäure (MSA) und Wasser untersucht. Dies sind geeignete Modellsysteme um die grundlegenden Mechanismen der protonischen Ladungserzeugung und der protonischen Transportmechanismen zu verstehen.

Um aufzuklären, ob bei geringen Wasserkonzentrationen die Strukturdiffusion eine Rolle spielt, führten wir Messungen der Kernspinresonanz (NMR) und der elektrischen Leitfähigkeit an unterschiedlichen sulfonsäurebasierten Modellsystemen wie beispielsweise dem System MSA-Wasser durch. Diese Studien erstreckten sich über weite Bereiche der Temperatur und des Wassergehaltes. Die NMR Methode der gepulsten magnetischen Feldgradienten (PFG-NMR) erlaubt es uns, die weitreichende Protonendiffusion direkt zu messen, während die NMR Daten der Spin-Gitter-Relaxation es ermöglichen, die lokalen Bewegungsprozesse zu identifizieren. Es ist wichtig zu erwähnen, dass aufgrund der unterschiedlichen chemischen Verschiebungen der NMR Signale von Protonen die C-H und O-H Bindungen bilden, die Diffusionskoeffizienten von beiden Arten von Protonen in MSA und MSA-Wasser Mischungen mit der PFG-NMR getrennt gemessen werden konnten. Ergänzend zu den Diffusionsuntersuchungen wurden Messungen der AC-Impedanz

durchgeführt, um die Transportmechanismen aufzuklären. Die Abhängigkeit der chemischen Verschiebung vom Wassergehalt der MSA-Wasser Systeme, die mit Hilfe der hochauflösenden Protonen-NMR bestimmt wurde, liefert wichtige Informationen über die Dissoziationskonstante des Systems und damit auch über die protonische Ladungsträgerdichte. Wenn die Ladungsträgerdichte bekannt ist, ermöglich es der Vergleich von Diffusions- und Leitfähigkeitsdaten, die über die Nernst-Einstein Beziehung miteinander verknüpft sind, den Mechanismus der Protonenleitung zu analysieren.

Wir berichten über umfassende Messungen der Diffusion, der Spin-Gitter-Relaxation und der Leitfähigkeit von Methylsulfonsäuren mit unterschiedlichem Wassergehalt. Die Ergebnisse zeigen, dass in Methylsulfonsäure-Wasser Systemen und ähnlichen sulfonierten Systemen bei geringem Wassergehalt der Vehikelmechanismus der dominierende Mechanismus darstellt.

Als ein kompelentäres Modellsystem zur Untersuchung des Effekts der Hydrophobizität in realen Membranen von Brennstoffzellen wurden MSA-Wasser-Alkohol Systeme untersucht. Messungen der hochaufgelösten ^{1}H-NMR Spektren sowie der elektrischen Leitfähigkeit erfolgten an MSA-Wasser-[Ethanol, Isopropanol], zwei unterschiedlichen Alkoholen mit verschieden ausgeprägten Hydrophobizitäten.

Die Protonenleitfähigkeit wurden an realen sulfonierten Brennstoffzellen-membranen (Nafion-1100, Dow-858 und $SPSO_2$-360) bestimmt und mit den MAS-Wasser Systemen gemessenen Werten verglichen.

Die Protonenleitfähigkeiten dieser sulfonierten Membrane wurden auch unter einem Wasserdampfdruck von einer Atmosphäre (10^5 Pa) im Temperaturbereich zwischen 100 und 160°C gemessen.

Abstract

Polymer-electrolyte-membrane fuel cells (PEM-FCs) deliver high power density and offer the advantages of low weight and volume, compared to other fuel cell systems. State-of-the-art separator materials in PEM-FCs are sulfonic acid functionalized polymers, like the perfluorinated polymer Nafion.
The suitability of proton-conducting materials as separators in a particular fuel-cell application is essentially dependent on its transport properties, durability, and reactivity. Thus, this thesis has focused on the protonic transport properties and the protonic charge formation. Owing to the complexity of polymeric proton-conducting materials, we have studied Methanesulfonic acid (MSA)-water as a suitable model system in order to understand the basic mechanisms of protonic charge formation and proton transport in such systems.
In order to clarify whether structure diffusion plays a major role at low degree of hydration, we performed nuclear magnetic resonance (NMR) and electrical conductivity measurements on different sulfonic acid model systems, including MSA-water system. These studies have been extended over wide ranges of temperature and water content. Pulsed-field-gradient (PFG) NMR provides a direct access to the long-range diffusivity, while the spin-lattice-relaxation rate allows identifying local transport processes. It is important to note that due to the different chemical shift of protons forming C-H and O-H bonds, the diffusivities of both kinds of protons in MSA and MSA-water mixtures could be measured separately by PFG-NMR. Complementary to diffusion studies, AC-impedance spectroscopy has been applied to investigate charge transport. The dependence of the chemical shift on the water content of MSA-water systems, as observed by high-resolution ^{1}H-NMR, provides information on the dissociation constant of the system, and thus on the protonic charge carrier density. If the charge carrier density is known, a comparison of conductivity and diffusion data, which are related via the Nernst-Einstein relation, permits analyzing the proton conduction mechanism.

We report on comprehensive diffusion, spin-lattice relaxation and conductivity measurements on MSA at different degrees of hydration. The results indicate that the vehicle transport mechanism is the dominant proton conduction mechanism in MSA-water system and similar sulfonated systems at low degrees of hydration.

MSA-water-alcohol system has been used as a complementary model system to investigate the effect of hydrophobicity of the real fuel cell polymer backbone. Data on high resolution ^{1}H-NMR spectra and electrical conductivity have been obtained on MSA-water-[ethanol, isopropanol] as two different alcohols with different degree of hydrophobicity. The results suggest that the main effect of hydrophobic interactions on the proton conductivity is a reduction of the -SO_3H dissociation.

Proton conductivity data on examples of real sulfonated fuel cell membranes (Nafion-1100, Dow-858, and $SPSO_2$-360) have been measured and compared to the conductivity of the MSA-water system.

The protonic conductivity of these examples for sulfonated membranes have also been investigated at a water vapor pressure of p = 10^5 Pa at temperature from T = 100 to 160 °C.

1 Introduction

Polymer-electrolyte-membrane fuel cells (PEM-FCs) are considered as the most promising fuel cell technique for mobile and portable applications. They deliver high power density and offer the advantages of low weight and volume, compared to other fuel cell systems. State-of-the-art separator materials in PEM-FCs are commonly sulfonic acid functionalized polymers, like the perfluorinated polymer Nafion. The proton transport takes place through a thin water-swollen co-polymer film that contains sulfonic acid (SO_3H) groups. The efficiency of the proton conduction process depends upon water content. However, these materials show the required high proton conductivity only at high degree of hydration, i.e. high water content. But at elevated temperatures (T > 80 °C) and low relative humidity these membranes show low proton conductivity and poor mechanical stability.[1,2]

This hydration water solvates the acidic protons of the sulfonic acid functional groups and promotes proton mobility by structure diffusion (especially at high water contents) and predominantly vehicle-type transport at low water content. In any case, water is essential for the formation and mobility of protonic charges.[3,4]

Because of the poor connectivity (percolation) of the water structures in these polymers and the strong local retardation of the water diffusion, fast proton conduction according to a vehicle mechanism is not possible at low degrees of hydration. But there is experimental indication that high proton conductivity in sulfonic acid based systems may be possible even at low hydration levels, provided that the sulfonic acid groups are spatially less separated. The observation that the proton conductivity of aqueous highly concentrated sulfuric acid H_2SO_4 shows a non-linear behaviour with decreasing water content [5] indicates another proton conduction mechanism appearing at low degrees of hydration, e.g. structure diffusion within hydrogen bonded network formed by sulfonic acid group and water.

Due to the complicity to understand the protonic conductivity, protonic charge formation and the mechanism of the $H^+(H_2O)_n$ diffusion at different

temperatures and relative humidity levels in these real fuel cells polymeric membranes, the current study focus on a suitable model system. Methanesulfonic acid-water [CH_3SO_3H (MSA) -H_2O] as a binary system has been used to simulate the interactions in these real sulfonated membranes. In the second part of the study, the effect of adding alcohols (ethanol, isopropanol) to the binary system (MSA-water) has been investigated. These studies provide information on the effect of $H^+(H_2O)_n$ interaction with the polymer backbone in real fuel cell membranes.

The following schematic picture illustrates the connection between the real sulfonated fuel cells membrane and the selected model system.

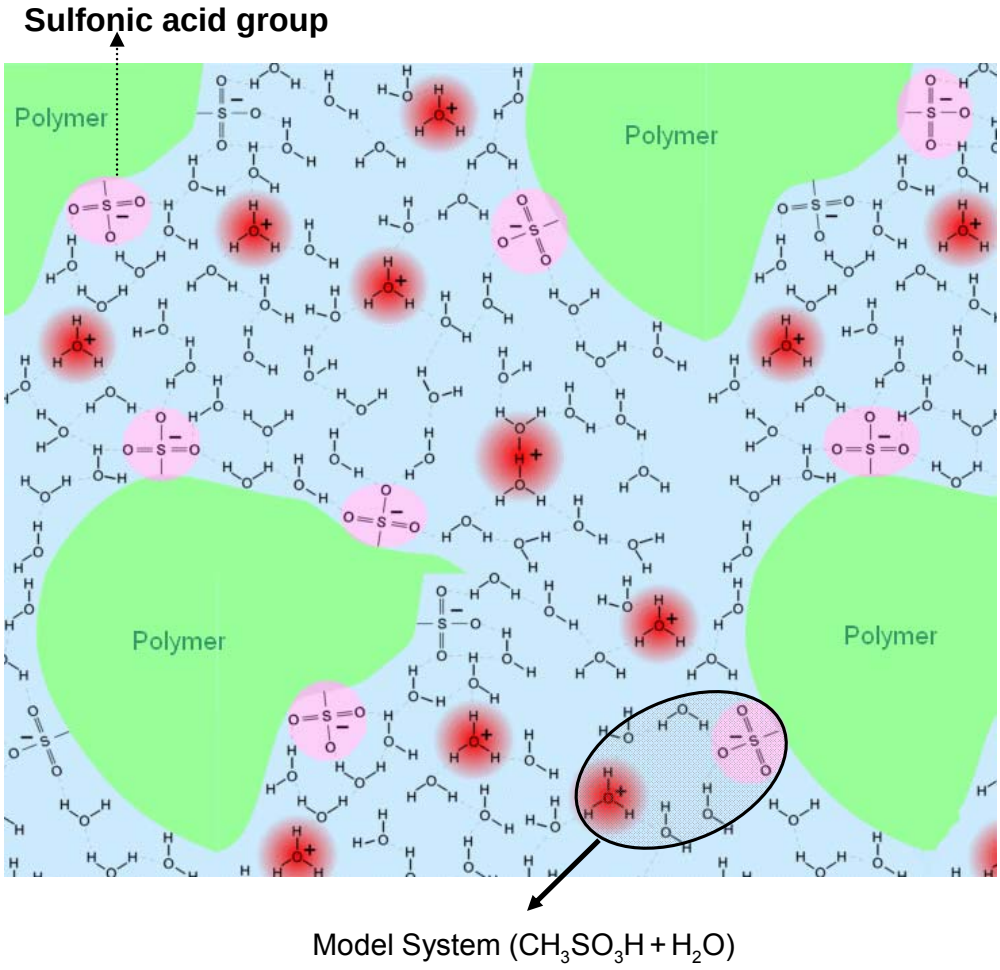

In order to clarify whether structure diffusion plays a major role at low degree of hydration, nuclear magnetic resonance (NMR) and conductivity measurements have been performed on different sulfonic acid model systems, including CH_3SO_3H (MSA). These studies have been extended over wide ranges of temperature and water content.

NMR allows us to investigate the diffusivity both on a macroscopic and on a microscopic scale. Pulsed-field-gradient PFG-NMR provides a direct access to the long-range diffusivity, while the spin-lattice-relaxation rate allows identifying local transport processes. It is important to note that due to the different chemical shift of protons forming C-H and O-H bonds, the diffusivities of both kinds of protons in MSA could be measured separately by PFG-NMR. Complementary to diffusion studies, AC-impedance spectroscopy has been applied to investigate charge transport.

The dependence of the chemical shift on the water content of MSA-water systems, as observed by high-resolution ^{1}H-NMR, provides information on the dissociation constant of the system, and thus on the protonic charge carrier density. If the charge carrier density is known, a comparison of conductivity and diffusion data, which are related via the Nernst-Einstein relation,[6] permits analyzing the proton conduction mechanism.

This thesis reports on comprehensive diffusion, spin-lattice relaxation and conductivity measurements on MSA at different degrees of hydration. The data have been used to analyze the proton conduction mechanism in sulfonic acid based systems, with special emphasize on systems with low degrees of hydration. The results indicate that with decreasing water content a change in the conduction mechanism appears, from mainly vehicle diffusion to predominantly structure diffusion.

This thesis is divided into six chapters as follows:

Chapter 1: Introduction and motivation.

Chapter 2: Deals with the theory of Nuclear Magnetic Resonance (NMR). Special emphasizes is put on the pulsed filed gradient NMR. Then the studied materials and some of there properties are introduced.

Chapter 3: The proton conductivity and proton transport mechanisms have been introduced including the formation and the mobility of the protonic charge carriers.

Chapter 4: The experimental setups (NMR, PFG-NMR, AC-Impedance analyzer and TGA) have been explained with the support of schematic drawings. The home-built conductivity cells for different samples (liquids and solid ones) are introduced. The sample preparation and the measurement steps including the required calibrations and procedures are explained in detail.

Chapter 5: The results have been discussed focusing in the following aspects: (^{1}H-NMR spectra, spin lattice relaxation rate Γ_1, translational diffusion *D*, and the electrical conductivity σ). High resolution ^{1}H-NMR results were used to find protonic charge carriers concentration as a function of water content. The Nernst-Einstein relation has been used to calculate the electrical conductivity from PFG-NMR diffusion data. The comparison between the calculated and the experimentally observed ionic conductivity were used to find the transport mechanism in the model system. The absolute water content was measured using TGA in order to compare the results for the corresponding water content in the model system.

Chapter 6: Summary and conclusions are presented.

2 NMR Theory

2.1 Fundamentals of NMR

Nuclear magnetic resonance (NMR) spectroscopy is the study of molecular structure through measurement of the interaction of an oscillating radio-frequency electromagnetic field with a collection of nuclei immersed in a strong external magnetic field. These nuclei are parts of atoms that, in turn, are assembled into molecules. An NMR spectrum, therefore, can provide detailed information about molecular structure and dynamics, information that would be difficult, if not impossible, to obtain by any other method. It was in 1902 that the physicist P. Zeeman got a Nobel Prize for discovering that the nuclei of certain atoms behave strangely when subjected to a strong external magnetic field. Purcell and Bloch shared a Nobel Prize for putting the so-called nuclear Zeeman-effect to practical use by constructing the first (crude) NMR spectrometer. During the succeeding years, NMR has completely revolutionized the study of chemistry and biochemistry, and it had also a significant impact on a host of other areas. Nuclear magnetic resonance has become arguably the single most widely used technique for elucidation of molecular structure. But before we can begin our foray into NMR, we need to review a few fundamental principles from physics.[7]

2.1.1 Origin of Nuclear Magnetization

Magnetism is an inherent physical property of matter in which materials interact with an external magnetic field to establish their own fields. The degree of interaction is characterized by the magnetic susceptibility χ, defined as the ratio of the induced field to the external field. While ferromagnetic materials interact strongly with the external field, the interactions for most materials are weak; with χ in the order of 10^{-5} (e.g. χ of water is -9×10^{-6}). Paramagnetic materials are those whose induced fields are in the same direction as the external field, whereas diamagnetic materials (such as water) have fields in the opposite direction. The magnetism that is of interest to NMR arises from the atomic nuclei. The atomic nucleus, in general, is composed of protons and neutrons. The intrinsic rotational motion

(or spin) and the inertial mass of each proton and neutron give rise to its individual spin angular momentum, which has a spin quantum number I of 1/2. In an ensemble of an even number of protons or neutrons, pairing of angular momenta in equal and opposite directions, resulting in a zero net momentum, occurs since the configuration corresponds to the lowest and most stable energy state. Therefore, atomic nuclei containing either an unpaired proton or neutron exhibit a net nuclear spin, and have *I* in multiples of 1/2 (1/2, 3/2, 5/2, etc.). The actual derivation of the nuclear spin from spins of protons and neutrons follows laws of quantum mechanics. The hydrogen nuclei (protons) are the most commonly used nuclei in NMR studies, and have a nuclear spin of 1/2.

Being a charged particle, a spinning proton acts as a microscopic current-carrying loop and has an associated magnetic moment, or dipole. The magnetic moments of the proton and neutron are $2.79\mu_n$ and $-1.91\mu_n$, respectively, where $\mu_n = e\hbar/2m_p$ denotes the nucleus magneton. These small magnetic moments are indicative of the inherent low sensitivity of NMR experiments. The neutron has a negative magnetic moment to indicate that its angular momentum and magnetic moment are in opposite directions. As the neutron has zero charge, the fact that it has a magnetic moment gives a clue that it must be composed of smaller, charge-bearing and spinning elementary particles. A nucleus with spin I has a magnetic moment of magnitude μ given by $\mu=\gamma\hbar I$, where γ is the nuclear gyromagnetic ratio. The ratio is a constant for each isotope. For the hydrogen nucleus, $\gamma/2\pi$ is 42.58 MHz / Tesla (1 Tesla = 10^4 Gauss).[8]

2.1.2 Boltzmann Distribution

Nuclear magnetic moments in matter are normally oriented in random directions. When placed in an external magnetic field, the dipoles become aligned with the field. Once a particle with $I=1/2$ absorbs a photon, the energy originally associated with the electromagnetic radiation goes into a spin flip. The photon's energy is absorbed by a nucleus in the lower energy spin state m_I = +1/2 (spin-up), and the nucleus is flipped into its higher

energy spin state m_I = -1/2 (spin-down). This situation is depicted in Figure 2-1.

In general, m_I represents $2I$+1 alignment states (from m_I = -I,…,-3/2,-1/2, 1/2,…,I). The different states have slightly different energies, known as the Zeeman splitting of the energy level, given by:

$$E = -\gamma\hbar B_0 m_I \qquad (2-1)$$

γ is the gyromagnetic ratio, B_0 is the external magnetic field.[7,9]

The energy difference between the two allowable states of nuclei is then $\Delta E = \gamma\hbar B_0$.

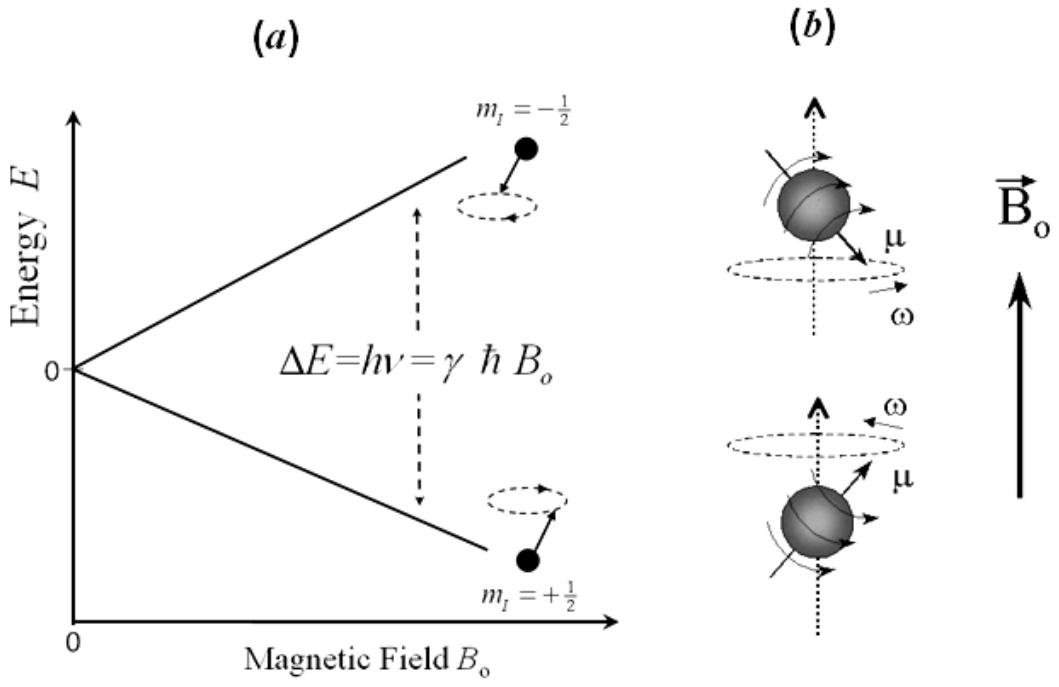

Figure 2-1*: **(a)** Relative energy of both spin states of an I =+1/2 nucleus as a function of the strength of the external magnetic field B_o. **(b)** $\omega_0 = \gamma B_0$ where ω_0 is the resonance frequency in radians per second, also called Larmor frequency.*

The population of spins in these states is determined by the Boltzmann law of statistical mechanics. For N protons split into populations N^+ and N^- in the spin-up and spin-down states, respectively, the populations of the states satisfy,

$$\frac{N^+}{N^-} = \exp(\frac{\gamma\hbar B_o}{kT}) \approx 1 + \frac{\gamma\hbar B_0}{kT} \qquad (2-2)$$

where *k* is the Boltzmann constant and T the absolute temperature of the spin system. It follows that the population difference between two states is:

$$\Delta N = N\frac{\gamma\hbar B_0}{2kT} \qquad (2-3)$$

Figure 2-2 shows the nuclear Zeeman energy splitting for the simplest I = 1/2 case. The nuclear spin up state is energetically more favourable to populate than the spin down

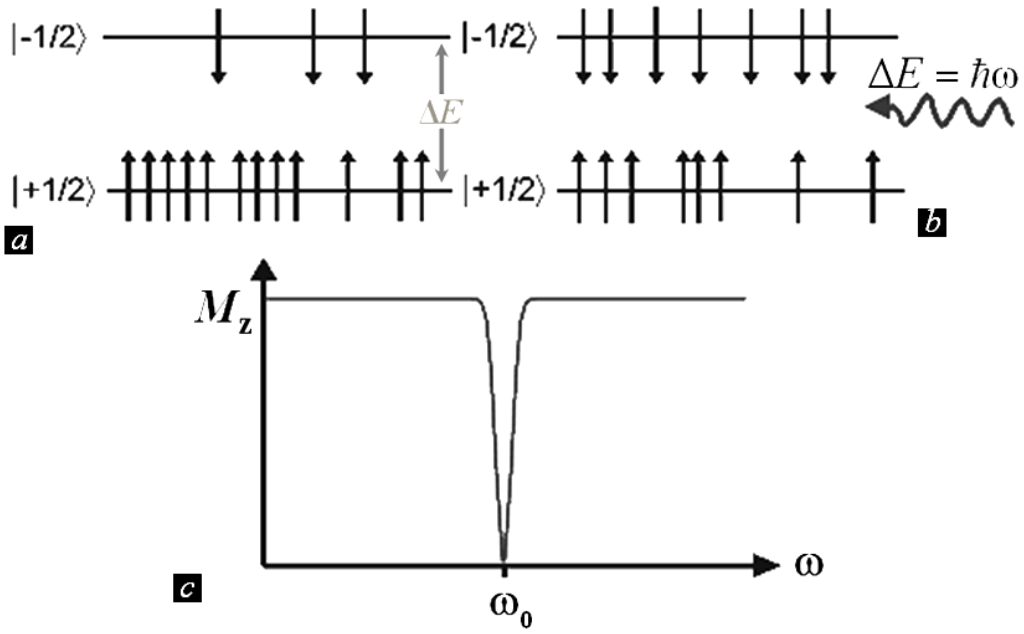

Figure 2-2*: **(a)** Schematic diagram for the energy splitting ΔE of a nucleus with spin I = 1/2 in the presence of a magnetic field B_Z **(b)** Applying an r.f. signal tuned to the Larmor resonance frequency ω_0 induces transitions between the levels. **(c)** In a continuous wave (CW) experiment, the magnetization in z direction, M_Z, decreases as the Larmor frequency is reached.* [10]

Since each proton carries a magnetic moment of $\frac{1}{2}\gamma\hbar$, the proton spin system has a macroscopic magnetic moment, or bulk magnetization:

$$M = \frac{N\gamma^2\hbar^2 B_0}{4kT} \qquad (2-4)$$

In thermal equilibrium, the bi-directional transitions between the two allowable energy states are equally probable. The resulting magnetization is denoted as the equilibrium magnetization M_0. By definition, the corresponding nuclear magnetic susceptibility is:

$$\chi = \gamma^2 \hbar^2 / 4kT \qquad (2-5)$$

The external magnetic field B_0 creates a torque on the nuclear magnetic dipoles. Analogous to the effect of gravity on a spinning top that is tipped away from the vertical, the torque forces the dipoles to precess about the direction of the magnetic field in a motion describing the wall of a cone. The rate of precession is governed by the Larmor relationship

$$\frac{\omega_0}{2\pi} = \frac{\gamma}{2\pi} B_0 \qquad (2-6)$$

where $\omega_0/2\pi$ is the cyclical resonance frequency, and γ is magnetogyric ratio. Although the laws of quantum mechanics dictate that dipoles can precess only at fixed angles to the external magnetic field, and at a constant frequency, the relative phases of the precessing spins are random, resulting in cancellation of their perpendicular components. Since spin 1/2 nuclei have more spins in the spin-up state (the lower energy, hence more stable state), the net equilibrium macroscopic magnetization is a vector pointing in the same direction as the applied field, this picture is illustrated in Figure 2-3.[11]

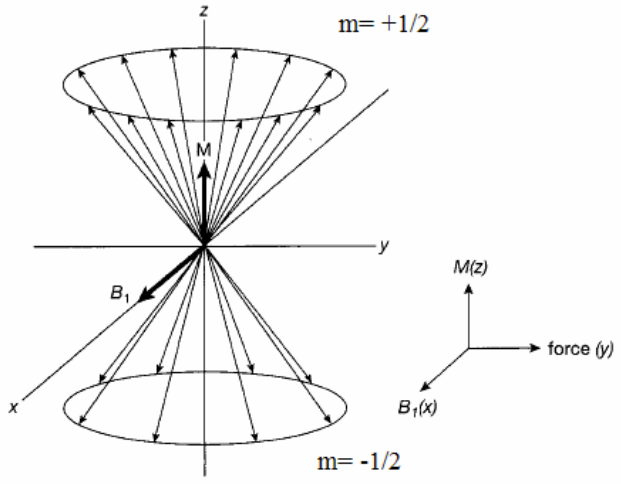

Figure 2-3*: Thermal equilibrium after applying a magnetic field B_0. Net magnetization along the axis of the magnetic field exists which is drawn as a vector, oriented along the magnetic field, representing the average effect of all these nuclei [11].*

2.1.3 Description of Spin Motion and Bloch Equation

The theories of Newtonian or classical mechanics can be used to empirically describe the behaviour of an ensemble of nuclear spins, in particular the bulk magnetization of spin 1/2 nuclei. A magnetic field $\vec{B}$ acts on a magnetization vector $\vec{M}$, with an angular momentum of $\vec{M}/\gamma$, a torque that is equal to the rate of change of the angular momentum,

$$d\vec{M}/dt = \gamma\vec{M} \times \vec{B} \qquad (2-7)$$

When $\vec{B}$ is a longitudinal field of amplitude B_0, the solution to equation (2-7) corresponds to a counter-clockwise precession of $\vec{M}$ about the longitudinal direction (conventionally taken to be the z-axis) at a rate $\omega_0 = \gamma B_0$, the angular Larmor frequency.

The recovery of the nuclear magnetization after a perturbation of the thermal equilibrium state is a process known as spin-lattice or longitudinal relaxation. It involves an exchange of energy between the spin system and its lattice, which is a reservoir of kinetic and potential energies for all degrees of freedom of the system. The rate of restoration is proportional to the difference between the longitudinal magnetization and its equilibrium value. Phenomenologicaly, the process is described by,

$$\frac{dM_z}{dt} = \frac{M_0 - M_z}{T_1} \qquad (2-8)$$

where T_1 is the relaxation time constant. In contrast, the transverse magnetization is governed by a process known as spin-spin T_2 relaxation whereby spins reach thermal equilibrium among themselves. In addition to longitudinal relaxation, transverse magnetization relaxation is affected by dispersion of spin phase coherence. The latter occurs, for example, when spins diffuse via Brownian motion through highly inhomogeneous magnetic fields. This leads to the result $T_2 \leq T_1$. For spins residing in liquid-state molecules, the phenomenological description of transverse relaxation is

$$\frac{dM_{x,y}}{dt} = \frac{-M_{x,y}}{T_2} \qquad (2-9)$$

The relaxation times, in particular T_2, are usually different for spins in different molecular environments. Adding the relaxation terms Equations (2-8) and Equation (2-9) to Equation (2-7), yields the well-known Bloch equation:[12]

$$\frac{d\vec{M}}{dt} = \gamma \vec{M} \times \vec{B} - \begin{pmatrix} M_x/T_2 \\ M_y/T_2 \\ (M_z - M_0)/T_1 \end{pmatrix} \qquad (2-10)$$

The equation provides an essential basis for describing and predicting the motion of nuclear magnetization relevant to NMR.

2.1.4 Free Induction Decay (FID) and NMR-Signal

When the magnetization of a spin system (or the sample) is tipped from its longitudinal equilibrium position by an r.f. pulse, for example one that causes a 90° tipping, an oscillating magnetic field is created.

The precessing transverse magnetization can induce an oscillatory voltage in the coil placed around the sample. This oscillating and decaying constitutes the primary NMR signal that is recorded in the time domain. The signal, induced by the magnetization in free precession, is known as the free induction decay (FID). The Fourier transform of the signal, which presents the signal in the frequency domain, is the NMR spectrum that is used in NMR spectroscopy (see Figure 2-4).[10,13]

The transverse magnetization components after the r.f. pulse have the following form:

$$\begin{aligned} M_y^{nuc} &= -M_{eq}^{nuc} \cos(\omega_0 t) \exp(-t/T_2) \\ M_x^{nuc} &= M_{eq}^{nuc} \sin(\omega_0 t) \exp(-t/T_2) \end{aligned} \qquad (2-11)$$

Both components oscillate at the nuclear Larmor frequency ω_0, and decay with the time constant T_2. The signals represented by Equation (2-11) contain enough information to determine both the magnitude of the Larmor frequency ω_0 and the decay time constant T_2. The larger the Larmor frequency ω_0, the faster the magnetization oscillates, while the larger the decay time constant T_2, the more slowly the signals decay.[13,14]

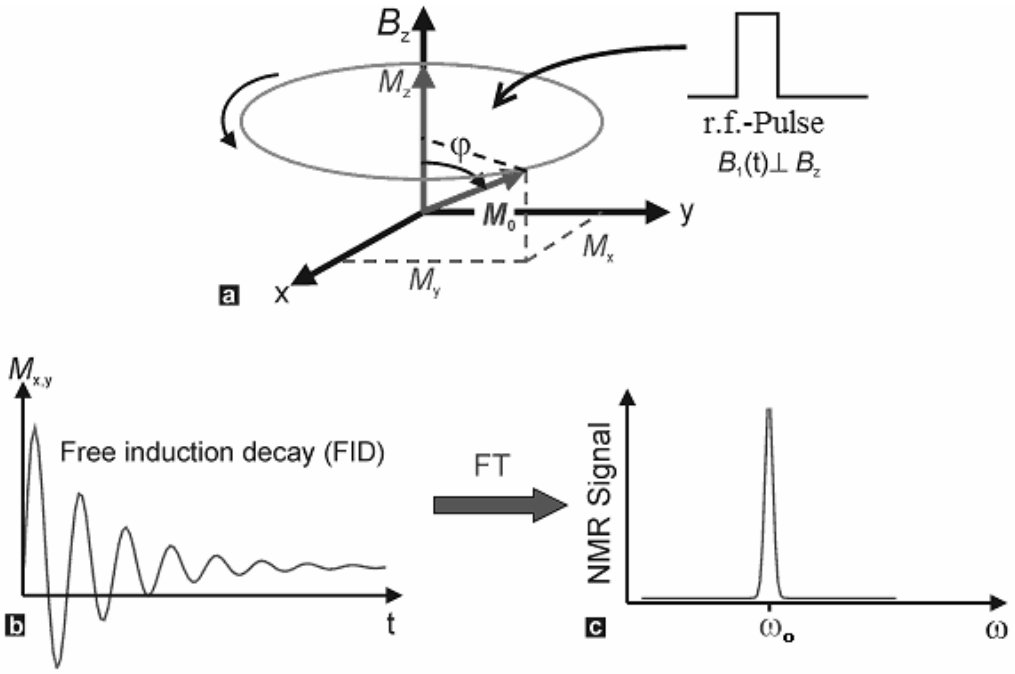

Figure 2-4*: **(a)** If an r.f. pulse tuned to ω_0 is applied perpendicular to the direction of the static magnetic field Bz, the M_z magnetization tips into the xy-plane by an angle φ. **(b)** An oscillating free induction decay (FID) signal of the M_x or M_y magnetization is observed in the NMR spectrum. **(c)** The Fourier transform of the FID gives a peak at the resonance frequency.*

2.1.5 Chemical Shift

The precise frequency absorbed by a given nucleus in a sample depends on its chemical environment. The magnetic field at the site of a given nucleus in a molecule is not the same as the external magnetic field in which the sample is immersed. $B = B_0 - B'$ where the field B' is caused by the field B_0 including an electric current in the electron cloud surrounding the nucleus. The result of chemical shift is that the actual resonance frequency differs slightly from the Larmor frequency, which is written as,

$$\omega = \gamma B_0(1-\sigma) \qquad (2-12)$$

where σ is a small dimensionless number known as the shielding constant. The value of σ depends on the location of the nucleus in the molecule. Further, since the distribution of electrons in a molecule is related to the

orientation of chemical bonds and is therefore anisotropic, shielding depends on the orientation of the molecule with respect to the applied magnetic field. This effect is known as chemical shift anisotropy.[32] The greater the shielding of the nucleus (the larger the value of σ), the lower will be its resonance frequency and the farther to the right it will appear in an NMR spectrum. Conversely, nuclei from which electron density has been withdrawn (resulting in a smaller σ) are said to be *deshielded* and appear toward the left of the spectrum (higher frequency).[7,9]

2.2 Relaxation Mechanisms

2.2.1 Spin-Lattice Relaxation

The spin lattice relaxation time $T_1 = 1/\Gamma_1$ is the characteristic time for a spin-system to return to the thermal equilibrium, after it has been disturbed by an r.f. pulse. The total relaxation rate can in general be written as,[15]

$$\Gamma_{1,tot} = \Gamma_{1,el} + \Gamma_{1,dip} + \Gamma_{1,quad} + \Gamma_{1,para} \qquad (2-13)$$

The contributions are as follows:

- **Electronic Relaxation:**

The electronic contribution $\Gamma_{1,el}$, resulting from the interaction between the magnetic moments of protons and conduction electrons, is usually described by the relationship:

$$\Gamma_{1,el} = \frac{T}{C_K} \qquad (2-14)$$

with the temperature and frequency-independent Korringa constant C_K.[16] In non metallic system $\Gamma_{1,el}$ is zero.

- **Quadrupole Relaxation:**

The quadrupole relaxation $\Gamma_{1,quad}$ is due to the interaction of the electric quadrupolar moment with fluctuating electric field gradients. In the case of protons, which do not have an electric quadrupole moment, this contribution has not to be considered.

- **Paramagnetic relaxation:** The paramagnetic relaxation $\Gamma_{1,para}$ is due to the interaction between the magnetic moments of the protons and paramagnetic impurities.[17]
- **Dipolar Relaxation:** Fluctuating magnetic fields, which are caused by diffusing magnetic dipoles, lead to the dipolar relaxation rate $\Gamma_{1,dip}$. Thus, the rate depends on the time constant of the movement of the nuclei τ_d. The dipolar relaxation depends also on the average distance, gyromagnetic ratios and the nuclear spin quantum numbers of the nuclei involved. The dipolar rate has a maximum, if the atomic jump frequency corresponds approximately to the resonance frequency of the nuclei in the applied magnetic field B_0. In other words, the condition for the maximum is,

$$\omega_0 \tau_{\mathrm{d}} \approx 1 \qquad (2-15)$$

- **Models for Correlation Functions for the Dipolar Relaxation**

As already described in the last section, the dipolar relaxation is caused by fluctuating magnetic fields. These fluctuations are caused by the diffusion movement of the spin carriers. The diffusing protons can interact both with the spins of other protons and with the spins of the other nuclei.[8] The total relaxation rate is given by the sum of the two corresponding contributions

$$\begin{aligned}\Gamma_{1,dip} &= \Gamma_{1,dip}^{\mathrm{HH}} + \Gamma_{1,dip}^{\mathrm{HW}} \\ &= \left(\frac{\mu_0}{4\pi}\right)^2 \left[\frac{3}{2}\gamma_{\mathrm{H}}^4 \hbar^2 I_{\mathrm{H}}\left(I_{\mathrm{H}}+1\right)\left(J_{\mathrm{HH}}^{(1)}\left(\omega_{\mathrm{H}}\right)+J_{\mathrm{HH}}^{(2)}\left(2\omega_{\mathrm{H}}\right)\right)\right. \\ &\left. +\frac{1}{12}\gamma_{\mathrm{H}}^2\gamma_{\mathrm{W}}^2\hbar^2 I_{\mathrm{W}}\left(I_{\mathrm{W}}+1\right)\left(J_{\mathrm{HW}}^{(0)}\left(\omega_{\mathrm{H}}-\omega_{\mathrm{W}}\right)+18J_{\mathrm{HW}}^{(1)}\left(\omega_{\mathrm{H}}\right)+9J_{\mathrm{HW}}^{(2)}\left(\omega_{\mathrm{H}}+\omega_{\mathrm{W}}\right)\right)\right]\end{aligned} \qquad (2-16)$$

The spectral density functions in Equation (2-16) are obtained by Fourier transformation of the pair correlation functions $G^{(\mathrm{p})}$.

$$J^{(\mathrm{p})}(\omega) = 2 \cdot Re \int_0^{\infty} G^{(\mathrm{p})}(t)\, exp(-\mathrm{i}\omega t)\, dt \qquad (2-17)$$

$$G^{(\mathrm{p})}(t) = \sum_{\mathrm{j}} \sum_{\mathrm{k}} F_{\mathrm{jk}}^{(\mathrm{p})}(0)\; F_{\mathrm{jk}}^{(\mathrm{p})^*}(t)\; P\left(r_{\mathrm{jk}}(0), r_{\mathrm{jk}}(t), t\right) \qquad (2-18)$$

where $P(r_{jk}(0), r_{jk}(t), t)$ represents the probability that a spin pair with a connection vector $r_{jk}(0)$ at the time $t = 0$ has the distance vector $r_{jk}(t)$ after a

time *t*. In equation (2-18) the expression $F_{jk}(p)$ represents a mathematical formulation of the dipole-dipole interaction and it can be written as follows:

$$F_{\mathrm{jk}}^{(\mathrm{p})}(0) = d_{\mathrm{p}}\, Y_{2\mathrm{p}}(\Omega_{\mathrm{jk}}) / r_{\mathrm{jk}}^{3}(t) \qquad (2-19)$$

$d_0^2 = 16\pi/15;\ \ d_1^2 = 8\pi/15$ and $d_2^2 = 32\pi/15$. With P=0, 1, and 2;

Here r_{jk} is the connecting vector between the spin carriers *j* and *k*. $Y_{2p}(\Omega_{jk})$ are the normal spherical harmonics.

- **BPP Model:**[18] This model was originally developed by Bloembergen, Purcell and Pound (BPP), for the description of the dipolar relaxation in liquids. The basic assumption of the BPP model is that $G^q(t)$:

$$G^{\mathrm{q}}(t) \propto \exp\left(-\frac{t}{\tau_{\mathrm{c}}}\right) \qquad (2-20)$$

While τ_{c} is the so-called correlation time for the dipole-dipole interaction Thus, the model results in a spectral density function which has a Lorentzian form, and can be written as,

$$J^{(q)}(\omega) \propto \frac{\tau_d}{1+(\omega_0\,\tau_d)^2} \qquad (2-21)$$

This model has the advantage of a simple analytic form and it yields in many cases satisfying results. After spherical averaging of the spectral density functions for powder samples, one gets

$$J^{(0)} : J^{(1)} : J^{(2)} = 6:1:4 \qquad (2-22)$$

with $$J^{(1)}(\omega) = \frac{2}{15}\sum_{k}(r_{\mathrm{jk}})^{-6}\frac{2\tau_{\mathrm{c}}}{1+\omega^2\tau_{\mathrm{c}}^2} \qquad (2-23)$$

In the case of pure proton-proton interaction, the correlation time is

given by, $$\tau_{\mathrm{c}} = \frac{\tau_{\mathrm{d}}}{2} \qquad (2-24)$$

since on the average after the time τ_d /2 one of the two interacting hydrogen atoms jumps on a neighbouring site. Using the Equations [(2-17), (2-22), (2-23) and (2-24)] the following equation is obtained.[19]

$$\Gamma_{1,dip} = \frac{4}{5}\gamma_{\mathrm{H}}^4 \hbar^2 I_{\mathrm{H}}(I_{\mathrm{H}}+1)(\omega_0)^{-1}\sum_{\mathrm{k}}(r_{\mathrm{jk}})^{-6}\left[\frac{y}{4+y^2}+\frac{y}{1+y^2}\right] \qquad (2-25)$$

with $y = \omega_0 \tau_d$, where $\omega_0 / 2\pi$ denotes the NMR frequency and τ_d is the mean dwell time of the migration hydrogen atoms. For a single thermally activated process of diffusion, τ_d is given by

$$\tau_d = \tau_0 \exp(H_a / k_B T) \qquad (2-26)$$

M_2 is the so-called second moment of the dipole-dipole interaction, the definition of M_2 can be written in the following equation.

$$M_2 = \frac{3}{5}\gamma_{\mathrm{H}}^4 \hbar^2 I_{\mathrm{H}}(I_{\mathrm{H}}+1)\sum_{\mathrm{j}}(r_{\mathrm{ij}})^{-6} + \frac{4}{15}\gamma_{\mathrm{H}}^2 \gamma_{\mathrm{w}}^2 \hbar^2 I_{\mathrm{w}}(I_{\mathrm{w}}+1)\sum_{\mathrm{j}^*}(r_{\mathrm{ij}^*})^{-6} \qquad (2-27)$$

Substituting Equation (2-27) into Equation (2-25) the final equation describing the dipole relaxation is obtained and can be written as,[19]

$$\Gamma_{1,dip} = \frac{4}{3}\frac{M_2}{\omega_0}\left[\frac{y}{4+y^2}+\frac{y}{1+y^2}\right] \qquad (2-28)$$

Figure (2-5) shows simulated BPP-curves for $\Gamma_{1,dip}$ curve for two different NMR frequencies ω_1 and ω_2, where $\omega_1 < \omega_2$

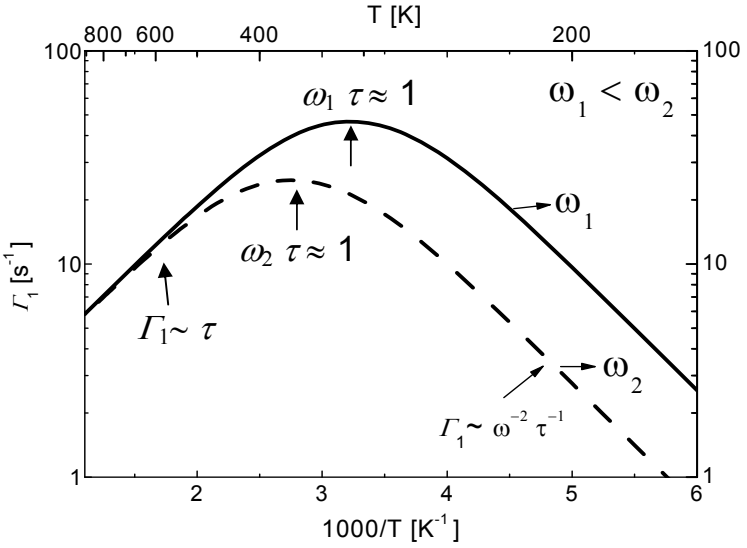

Figure 2-5*: Simulated BPP-curve for two different NMR frequencies (ω_1 and ω_2), where $\omega_1 < \omega_2$.*

We note that the maximum of the curve is obtained when, $\omega_0\tau_d = 1.23$. In the high temperature limit $\omega_0\tau_d \ll 1$, one obtains,

$$\Gamma_{1,dip} \sim M_2.\tau_d \qquad (2-29)$$

In this limit, $\Gamma_{1,dip}$ is frequency independent, as seen in Figure 2-5. In the low temperature limit $\omega_0\tau_d \gg 1$, we obtain:

$$\Gamma_{1,dip} \sim \frac{M_2}{\omega_0^2} \cdot \tau_d^{-1} \qquad (2-30)$$

At the low temperature limit, $\Gamma_{1,dip}$ is frequency depended as it is also evident from the Figure 2-5. The BPP-model yields the activation enthalpy H_a, the second moment M_2, and the pre-exponential factor τ_0.[18]

2.2.2 Spin-Spin Relaxation Rate

The spin-spin relaxation rate Γ_2 often also called transversal relaxation, leads to the loss of phase coherence of nuclear spins. The rate Γ_2 consists of two components:

$$\Gamma_2 = \Gamma_{2,inh} + \Gamma_{2,hom} \qquad (2-31)$$

The inhomogeneous part is due to temporally constant, but locally different values for the precession frequency of the spin particles. These spatial variations are usually caused by magnetic field inhomogeneities. Losses of the phase coherence, which are caused by inhomogeneous processes, can be cancelled by spin echo experiments.[20]

- **Nuclear Dipole-Dipole Interaction**

The magnetic dipolar interaction is usually the most important cause of the line broadening in a rigid lattice of magnetic dipoles.[21] The Hamiltonian of dipole-dipole interaction between two spins is,

$$H_{12} = \frac{\hbar^2\gamma_1\gamma_2}{r_{12}^3}\left[I^{(1)} \cdot I^{(2)} - \frac{3(I^{(1)} \cdot r_{12})(I^{(2)} \cdot r_{12})}{r_{12}^2} \right] \qquad (2-32)$$

where γ_1 and γ_2 are the gyromagnetic ratios, $I^{(1)}$ and $I^{(2)}$ are the spin operators, and r_{12} is the connecting vector from spin 1 to spin 2. Because of

its large anisotropy and relative strong dependence upon *r*, the dipole-dipole interaction can be used to obtain structural information.

At low temperatures with motion frozen out, the dipole-dipole interaction determines the NMR line-width and shape. As diffusive motion of proton increases at higher temperature, the NMR line-width approaches zero by random atomic motion.[22]

2.2.3 Motional Narrowing

The line-width decreases for nuclei in rapid relative motion. The effect in solids is illustrated in Figure 2-6. Diffusion resembles a random walk as atoms jump from one crystal site to another. An atom remains at one site for an average time τ that decreases markedly as the temperature increases. If the atoms are in rapid relative motion, the local field B_i seen by a given spin will fluctuate rapidly in time. The shorter τ, the narrower is the resonance line. This remarkable effect is known as motional narrowing.[21]

The longest value of τ_d observable is of the order of the reciprocal rigid lattice line-width. The shortest value of τ_d corresponds to that point where the narrowed dipolar line-width becomes just less than the inhomogeneity of the applied magnetic field. The simple observation of line narrowing is convincing evidence that diffusion is occurring. In many instances, sufficient data for τ_d are obtained to determine the activation energy for diffusive motion (see e.g. [23]).

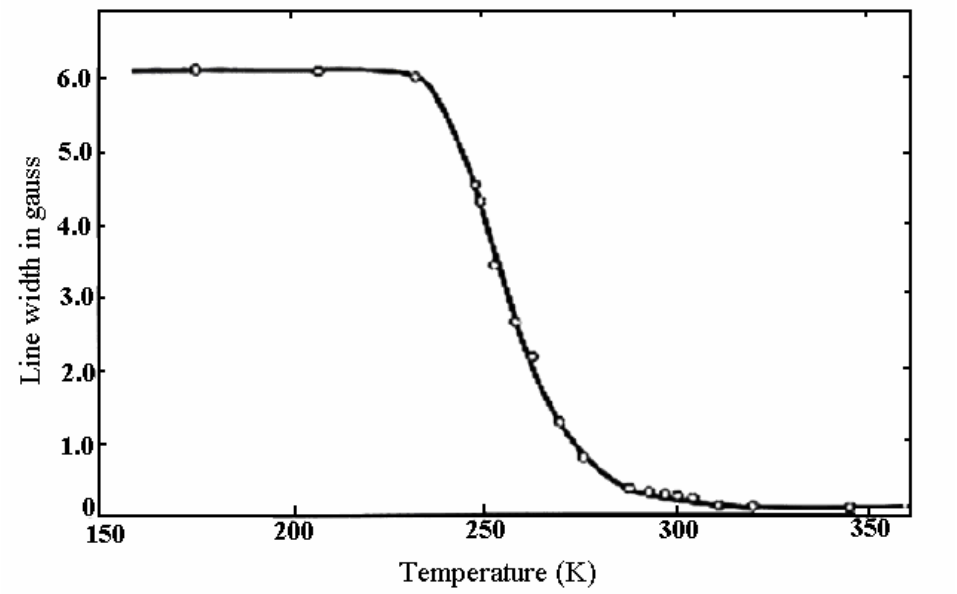

Figure 2-6*: Effect of diffusion of nuclei on the ^{7}Li NMR line-width in metallic lithium. At low temperatures the line-width agrees with the theoretical value for rigid lattice. As the temperature increase the diffusion rate increases and the line-width decreases. The abrupt decrease in line-width above T = 230 K occurs when the diffusion hopping time τ becomes shorter than $1/\gamma B_i$. Thus; the experiment gives a direct measure of the hoping time for an atom to change lattice sites.*[23]

2.3 Pulsed Field Gradient NMR

Pulsed field gradient spin echo (PGSE) nuclear magnetic resonance (NMR) is a powerful method for the study of dynamics in condensed matter since it probes translational motion of molecules selectively, without being affected by vibrational or rotational motions. Due to this advantage it has been widely applied to the dynamics of molecules in liquids. However, applications of this technique to strongly dipole-coupled spin systems with short T_2 or to the study of slow diffusion require rather high magnetic field gradients.[24] In the present study PFG-NMR is applied to the study the self-diffusion in liquid and solid state samples, with the use of a home-built PFG-NMR spectrometer.

2.3.1 NMR Self-Diffusion and Magnetic Gradients as Spatial Labels

Self-diffusion is the random translational motion of molecules (or ions) driven by internal kinetic energy. Translational diffusion (not to be confused with

spin diffusion or rotational diffusion) is the most fundamental form of transport[25,26,27] and is responsible for all chemical reactions, since the reacting species must collide before they can react.[28]

Already in the first spin echo NMR experiments, which were introduced just a few years after the experimental discovery of the NMR phenomenon,[29,30] Hahn[31] realized that the self-diffusion of the molecules carrying the nuclear spins under investigation reduces the intensities of the observed NMR signals. He also noticed that this effect depends on the homogeneity of the polarizing magnetic field and estimated the field gradient of his magnet using the known self-diffusion coefficient. Hahn actually proposed to apply these new spin echo techniques for studies of "relative values of the self-diffusion coefficient *D*, a quantity which is very difficult to measured by ordinary methods".[3]

According to Fick's first law of diffusion, the particle flux *J* at position *r* is proportional to the gradient of the concentration. Thus,

$$J(r,t) = -D\nabla c(r,t) \qquad (2-33)$$

where D is the diffusion coefficient and $c(r, t)$ is the concentration in number of particle per unit volume. The conservation of mass is assured by the equation of continuity,

$$\frac{\partial c(r,t)}{\partial t} = -\nabla \cdot J(r,t) \qquad (2-34)$$

and this equation can be combined with Equation (2-33) to obtain Fick' s second law of diffusion:[32]

$$\frac{\partial c(r,t)}{\partial t} = D\nabla^2 c(r,t) \qquad (2-35)$$

It is assumed that D has at most a weak dependence on the concentration.

In following it is convenient to introduce the conditional probability $P(r_0|r, t)$ that a particle initially at r_0 will be at r at time t, and it is reasonable to assume that $P(r_0|r, t)$ also obeys the diffusion equation so that:

$$\frac{\partial P(r_o \mid r,t)}{\partial t} = D\nabla^2 P(r_o \mid r,t) \qquad (2-36)$$

The solution of Equation (2-36) by standard means for unrestricted diffusion with the initial condition $P(r_o \mid r,t) = \delta(r_o - r)$ yields the expected Gaussian dependence on the displacement:

$$P(r_o \mid r,t) = (4\pi Dt)^{-3/2} \exp\left(-\frac{(r-r_0)^2}{4Dt}\right) \qquad (2-37)$$

The calculation of the average square displacement by means of Equation (2-36) gives the Einstein-Smoluchowski equation:

$$\left\langle (r - r_o)^2 \right\rangle = 6Dt \qquad (2-38)$$

Thus, molecular displacement resulting from diffusion is simply related to the diffusion coefficient.

In a PFG-NMR measurement, motion is measured over the millisecond to second time scale, the ability of NMR to detect translational motion and to image spin density depends on two essential facts: firstly, a nucleus at position *r* precesses with the frequency

$$\omega(r) = \gamma B(r) \qquad (2-39)$$

where $B(r)$ is the magnitude of the local magnetic field (flux density).

The second fact is that the local fields can be manipulated through the use of magnetic field gradients so that the spatial positions of nuclei can be encoded.

2.3.2 Spin Echos

The spin echo experiment is the basis of NMR diffusion measurements, since this experiment involves the refocusing of magnetization in inhomogeneous magnetic fields, a process that is extremely sensitive to the translational motion of spins.[33] Since B_0 is spatially homogeneous, ω is the same throughout the sample. However, if in addition to B_0 there is a spatially

dependent magnetic field (gradient G [$T \cdot m^{-1}$]), ω becomes spatially dependent.[34,35]

$$\omega_{eff}(r) = \omega_0 + \gamma(G \cdot r) \qquad (2-40)$$

where we define G by the field gradient component parallel to B_0

$$G = \nabla B_0 = \frac{\partial B_z}{\partial x}\hat{i} + \frac{\partial B_z}{\partial y}\hat{j} + \frac{\partial B_z}{\partial z}\hat{k} \qquad (2-41)$$

The important point is that if a homogeneous gradient of known magnitude is imposed throughout the sample, the Larmor frequency becomes a spatial label with respect to the direction of the gradient. Usually, it is common to measure diffusion with the gradient oriented along the z-axis parallel to B_0. The use of gradients along more than one axis is used when we consider anisotropic diffusion. In the case of a single gradient oriented along z, the magnitude of B is only a function of the position on the z-axis. We can see from Equation (2-40) that for a single spin the cumulative phase shift is given by

$$\varphi(t) = \underbrace{\gamma B_0 t}_{\text{static field}} + \underbrace{\gamma \int_0^t G(t')z(t')dt'}_{\text{applied gradient}} \qquad (2-42)$$

where the first term on the right-hand side corresponds to the phase shift due to the static field, and the second term represents the phase shift due to the effects of the gradient. Obviously the degree of dephasing due to the gradient pulse is proportional to the type of nucleus (γ), the strength of the gradient (G), the duration of the gradient pulse (δ), and the displacement of the spin along the direction of the gradient. If a pulse of amplitude G and duration δ is applied, we can think of the ‘‘area’’ or ‘‘dephasing strength’’ of the gradient pulse as equaling $\gamma G\delta$. In Equation (2-42) the gradient is written as $G(t)$ to emphasize that the gradient may itself be a function of time.[36,37]

2.3.3 Bloch Equation Including Diffusion

In the standard mathematical description of the Hahn echo experiment, a term describing the rate of translational diffusion of magnetization is added

to the Bloch equation to obtain a macroscopic theory of diffusion effects in NMR. Following the notation of Abragam[8] this gives,

$$\frac{\partial M(r,t)}{\partial t} = \gamma M \times B(r,t) - \frac{M_x i + M_y j}{T_2} - \frac{(M_z - M_0)k}{T_1} + D\nabla^2 M \qquad (2-43)$$

A more convenient equation for the investigation of transverse magnetization is obtained from Equation (2-43) by defining the complex magnetization $M_+ = M_x + iM_y$, setting B_x = B_y = 0, and denoting the magnitude of the average precession frequency in the sample by $\omega_o = \gamma B_o$. The resulting equation is

$$\frac{\partial M_+}{\partial t} = \mathrm{i}\omega_0 M_+ - \frac{M_+}{T_2} - \mathrm{i}\gamma(G.r)M_+ + D\nabla^2 M_+ \qquad (2-44)$$

The uninteresting parts of the time dependence are then transformed away by means of the substitution

$$M_+ = \psi \exp(\mathrm{i}\omega_0 t - t/T_2) \qquad (2-45)$$

to yield the equation[36]

$$\frac{\partial \psi}{\partial t} = -\mathrm{i}\gamma G z \psi + D\nabla^2 \psi \qquad (2-46)$$

In the absence of diffusion Equation (2-46) is easily solved for the magnetization in the rotating frame as a function of *z* and *t*. The complete sequence of r.f. and gradient pulses can be described by an effective *G*(t). With this approach it has been shown that the solution of Equation (2-46) in the presence of diffusion and a time dependent gradient can be written as

$$\ln \psi = -D\left[\int_0^t q^2(t')dt'\right] \qquad (2-47)$$

where

$$q(t') = \int_0^{t'} G(t'')dt'' \qquad (2-48)$$

It is important to note that gradient echos and spin echos have quite different properties in many experiments. The 180° r.f. pulse refocuses phase

dispersion resulting from background gradients, chemical shifts, susceptibility effects in heterogeneous samples etc., while the reversed gradient pulse only refocuses phase dispersion resulting from a previously applied gradient pulse.

2.3.4 Measuring Diffusion with Magnetic Field Gradients

The most common approach to measure diffusion coefficient is to use a simple modification of the Hahn spin-echo pulse sequence in which identical rectangular gradient pulses of duration δ are inserted into each τ period. This so-called ‘‘Stejskal and Tanner sequence’’ or ‘‘PFG sequence’’ is shown in Figure 2-7. Applying the magnetic field gradient in pulses instead of continuously circumvents a number of experimental limitations.[36,37] The basic Stejskal-Tanner experiment has two major advantages over constant gradient method. First, by confining the gradients to relatively narrow time intervals, this experiment permits gradient areas to be varied with out changing the echo time, so that the attenuation resulting from relaxation can be held constant. Second, the echo can be recorded in a homogeneous magnetic field. Spectral information is, therefore, retained and frequency resolved diffusion measurements are possible. These advantages are widely acknowledged, and almost all modem NMR diffusion measurement are made with some form of pulsed gradient experiments. However, a disadvantage of pulsed experiments should be noted. The switched gradient experiments require current pulses that inevitably produce heat, mechanical forces and eddy currents.

The Stejskal-Tanner method is suitable for measuring the diffusion coefficient of more than one species simultaneously since the gradient is not applied during acquisition so the line-width is not broadened. Smaller diffusion coefficients can be measured since it is possible to use larger gradients. As the gradient is applied in pulses it is normally possible to separate the effects of diffusion from spin-spin relaxation. Generally, the applied gradient pulses are much stronger than any background gradients that may be present.

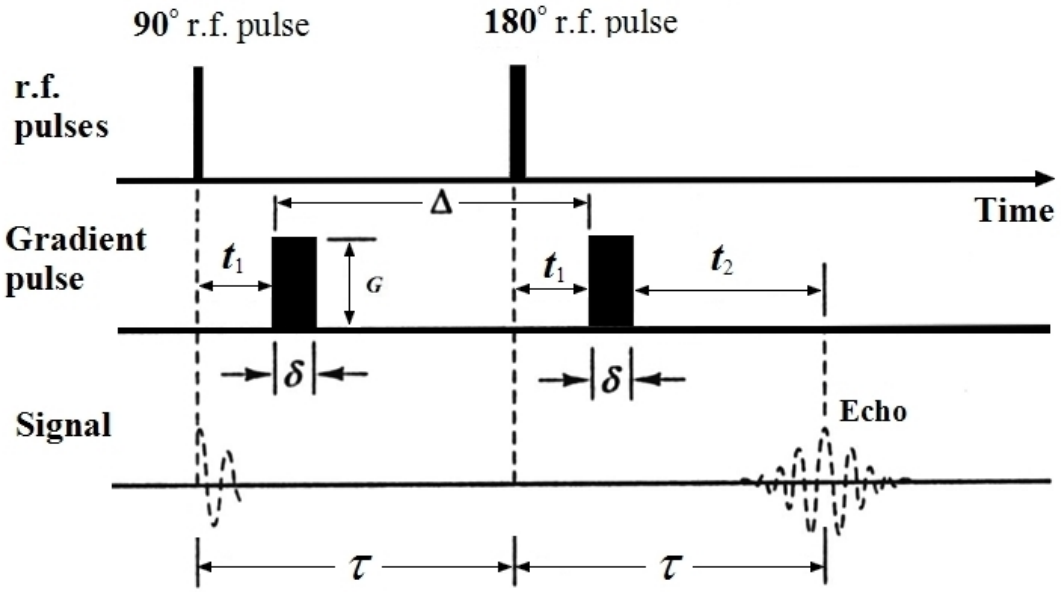

Figure 2-7: The Stejskal-Tanner pulsed field gradient spin echo diffusion experiment

The mechanism is shown schematically in Figure 2-7. Imagine that we have an ensemble of diffusing spins at thermal equilibrium (the net magnetization is oriented along the *z*-axis). A 90° r.f. pulse is applied which rotates the macroscopic magnetization from the *z*-axis into the *x*-*y* plane. During the first τ period at time t_1, a gradient pulse of duration δ and magnitude G is applied so that at the end of the first τ period, spin i experience a phase shift,

$$\varphi_i(\tau) = \underbrace{\gamma B_0 \tau}_{\text{static field}} + \underbrace{\gamma G \int_{t_1}^{t_1+\delta} z_i(t)dt}_{\text{applied gradient}} \qquad (2-49)$$

where the first term is the phase shift due to the main field, and the second one due to the gradient. At the end of the first τ period, a 180° r.f. pulse is applied that has the effect of reversing the sign of the phase angle or, equivalently, the sign of the applied gradients and static field. After time Δ from the first gradient pulse a second gradient pulse of equal magnitude and duration is applied (the 180° pulse has the effect of changing the sign of the first gradient pulse); this leads to the idea of an ‘‘effective’’ field gradient. If the spins have not undergone any translational motion with respect to the z-axis, the effects of the two applied gradient pulses cancel and all spins refocus. However, if the spins have moved, the degree of dephasing due to

the applied gradient is proportional to the displacement in the direction of the gradient (the *z*-direction) in the period Δ (the duration between the leading edges of the gradient pulses). Thus, at the end of the echo sequence, the total phase shifts of spin i relative to being located at $z = 0$ is given by

$$\begin{aligned}\varphi_i(2\tau) &= \underbrace{\gamma B_0 \tau + \gamma G \int_{t_1}^{t_1+\delta} z_i(t)dt}_{\text{first } \tau \text{ period}} - \underbrace{\gamma B_0 \tau + \gamma G \int_{t_1+\Delta}^{t_1+\Delta+\delta} z_i(t')dt'}_{\text{second } \tau \text{ period}} \\ &= \gamma G \left\{ \int_{t_1}^{t_1+\delta} z_i(t)dt - \int_{t_1+\Delta}^{t_1+\Delta+\delta} z_i(t')dt' \right\}\end{aligned} \qquad (2-50)$$

An ensemble of nuclei are concerned in NMR (with different spatial starting and finishing positions), and thus, the real component of the normalized intensity of the echo signal at $t = 2\tau$ is given by

$$S(2\tau) = S(2\tau)_{G=0} \int_{-\infty}^{+\infty} P(\phi, 2\tau)\cos\phi \, d\phi \qquad (2-51)$$

where $P(\phi,2\tau)$ is the relative phase-distribution function.

In the discussion above, we did not consider the relaxation process that occurs during the echo sequence. Thus, in the absence of diffusion and/or the absence of gradients, we would have the signal at $t = 2\tau$ equal to

$$S(2\tau)_{G=0} = M_0 \exp\left(-\frac{2\tau}{T_2}\right) \qquad (2-52)$$

where M_0 is the signal without attenuation due to spin-spin relaxation.

In the presence of diffusion and gradient pulses, the attenuation due to relaxation and the attenuation due to diffusion and the applied gradient pulses are independent, and so we can write,

$$S(2\tau) = \underbrace{M_0 \exp\left(-\frac{2\tau}{T_2}\right)}_{\text{attenuation due to relaxation}} \underbrace{f(\delta, G, \Delta, D)}_{\text{attenuation due to diffusion}} \qquad (2-53)$$

If the PFG measurement is performed whilst keeping τ constant, it is possible to separate the contributions. Hence, by dividing Equation (2-53) by

Equation (2-52) we normalize out the attenuation due to relaxation, leaving only the attenuation due to diffusion,

$$E = \frac{S(2\tau)}{S(2\tau)_{G=0}} = f(\delta, G, \Delta, D) \qquad (2-54)$$

The well-known diffusion term in the expression for the intensity of the Hahn spin-echo sequence[38] is given below for a constant gradient G_0

$$S(2\tau) = \underbrace{S(0)\exp\left(-\frac{2\tau}{T_2}\right)}_{\text{attenuation due to relaxation}} \underbrace{\exp\left(-\frac{2\gamma^2 D G_0^2 \tau^3}{3}\right)}_{\text{attenuation due to diffusion}} \qquad (2-55)$$

In the PFG experiment, we can alter δ, Δ, or G independently of τ and still perform this normalization, although the effects of relaxation are normalized out, since we use E as our experimental measure, the time scale of the experiment is limited by the relaxation time of the probe species. As Δ increases, so must τ, and eventually the signal will become too small to measure [see Equation (2-52)]. The smallest value of Δ will be limited by the performance of the gradient system.

The echo attenuation resulting from diffusion with the sequence shown in Figure (2-7) can be obtained by direct application of Equation (2-45). The total echo amplitude is given by[36]

$$S(2\tau) = S(0)\exp\left(-\frac{2\tau}{T_2}\right)\exp\left[-Dq^2(\Delta - \delta/3)\right] \qquad (2-56)$$

where $q = \gamma G\delta$ and the effect of transverse relaxation has been included. The attenuating factor $\psi(2\tau)$ for diffusion alone is easily isolated by taking the ratio of the echo amplitude with applied gradient switched on, $S(2\tau)$, to the amplitude with gradient switched off, $S_0(2\tau)$.[39,40]

Equation (2-56) is appropriate for the analysis of experimental data when the magnetic field B_o is homogeneous and the gradient pulses are well matched. It may be possible to approximate the effect of an inhomogeneous magnetic field by a constant background gradient G_0. The effective gradient is then $G + G_0$ and a complete analysis gives the diffusion factor:[36]

$$\psi(t) = \exp\left\{-D\gamma^2\left[\begin{array}{l} G^2\delta^2(\Delta-\delta/3)+2G_0^2\tau^3/3- \\ \qquad G.G_0\delta(t_1^2+t_2^2+\delta(t_1+t_2)+2\delta^2/3)\end{array}\right]\right\} \qquad (2-57)$$

Gradient pulse mismatch changes the position and intensity of the echo, some investigators have resorted to adjusting the width of the second gradient pulse to reposition the echo, but this is not a practical solution in experiments where the gradient areas are automatically ramped through a series of values and the signals is recorded starting from the center of the echo.[41,42,43]

3 Proton Conductivity and Proton Transport Mechanisms

3.1 Formation of Protonic Charge Carriers

Dissociation is the process by which a molecule separates into ions. Substances dissociate to different degrees, ranging from substances that dissociate very slightly, such as water, to those that dissociate almost completely, such as strong acids and bases. The extent to which a substance dissociates is directly related to its ability to conduct an electric current.

According to the ionic theory, the characteristic properties of acids are attributed to the hydronium ions which they produce in solution. As a result the solutions are excellent conductors of electricity.

The strength of a weak acid is indicated by its dissociation constant K_C which is defined as

$$K_C = \frac{[A^-][H_3O^+]}{[HA]} \qquad (3-1)$$

where $[A^-]$ is the molar concentration of the acid anions, $[H_3O^+]$ is the concentration of hydronium ions, [HA] is the concentration of undissociated acid. The dissociation constant K_C varies with temperature.

For strong electrolytes the dissociation constant as defined in Equation (3-1) varies considerably with change in concentration. So far it has been assumed that effective concentrations or activities could be expressed by the stoichiometric concentrations but, this is not strictly true. For a binary electrolyte system the correct equilibrium equation is:

$$K_a = \frac{a_{A^-} \times a_{B^+}}{a_{BA}} \qquad (3-2)$$

Where a_{A^-}, a_{B^+} and a_{BA} represent the activities of A^-, B^+ and AB and K_a is the thermodynamic dissociation constant (independent of concentration). The activity is a thermodynamic quantity and it is related to concentration by a factor called the activity coefficient. Using this concept, the thermodynamic activity coefficient is

$$K_a = \frac{[\mathrm{A}^-][\mathrm{B}^+]}{[\mathrm{AB}]} \times \frac{f_{\mathrm{A}^-} \times f_{B^+}}{f_{\mathrm{BA}}} \qquad (3-3)$$

where f refer to the activity coefficients and the square brackets to the molar concentrations. The activity coefficients of unionized molecules do not differ much from unity. For electrolytes in which the ionic concentration, and therefore the ionic strength is low, the error introduced by neglecting the difference between the actual values of the activity coefficients of the ions, f_{A^-}, f_{B^+} and unity is small. The activity coefficient varies with concentration, and for ions it varies with the charge and is the same for all dilute solutions having the same ionic strength. The activity coefficient depends upon the total ionic strength of a solution. The Debye-Hückel limiting law enables one to determine the activity coefficient of an ion in a dilute solution of known ionic strength which can be expressed in the following relation.[44]

$$log(f_i) = -Az_i^2\sqrt{I} \qquad (3-4)$$

where z_i is the charge number of ion species i, I is the ionic strength of the solution and A is a constant that depends on the solvent. The ionic strength of a solution is a function of the concentration of all ions present in a solution,

$$I = \frac{1}{2}\sum_{\mathrm{B}=1}^{n} c_{\mathrm{B}} z_{\mathrm{B}}^2 \qquad (3-5)$$

where c_B is the molar concentration of ion B, z_B is the charge number of that ion.

One factor that can limit the free ion concentration in a strong electrolyte solution is ion pairing, whereby free ions associate with ions of opposite charge to make electrically neutral ion pairs that do not contribute to the conductivity. Ion pairing differs from the process described above for weak electrolytes because the bonding in an ion pair is entirely electrostatic, whereas that in most weak electrolytes involves formation of covalent molecular bonds. Ion pairing may be understood as a competition between the energy of electrostatic attraction of two oppositely charged ions toward each other, which serves to keep the ion pair together, and the thermal

energy in the medium, which serves to break the ion pair apart, and the energy gain of individual solvation. The Bjerrum theory of ion pairing, which is the earliest and simplest theory, predicts that ion pairing will be greatest when the acid concentration is high, the acid ions are small and have high charge, the temperature is low, and the solvent permittivity (dielectric constant) is low.[45,46]

- **Ionization of Water**

In equilibrium, water molecules ionize endothermically due to the entropy gain. The water molecule that loses the hydrogen ion becomes a negatively charged (hydroxide ion). The water molecule that gains the hydrogen ion becomes a positively charged (hydronium ion). This process is commonly referred to as the self ionization of water and can be written as in the following formula:

$$2H_2O \rightleftharpoons H_3O^+ + OH^- \qquad (3-6)$$

Hydrogen ions are produced already hydrated (that is, as hydronium ions (H_3O^+)) and have negligible existence as naked protons in liquid or solid water. All three hydrogen atoms in the hydronium ion are held by strong covalent bonds and are equivalent.

As water is only slightly ionized, the ionic concentrations are small and the activity coefficients of the ions can therefore be regarded as unity. The activity coefficient of the unionized water molecule may also be taken as unity, and then the dissociation constant can be written as follows

$$K_C = \frac{[H_3O^+][OH^-]}{[H_2O]^2} \qquad (3-7)$$

Both ions create order and form strong hydrogen bonds with surrounding water molecules. The concentrations of H_3O^+ and OH^- are very small in pure water (10^{-7} at room temperature). As a sequence the conductivity of pure water is very low.[47]

- **Electroneutrality and Mean Quantity**

The ion-forming molecules have an overall electric charge of zero. If a system contains *s* different ions with molality m_i, (concentrations c_i, or mole

fractions x_i can also be employed), each bearing z_i elementary charges, then the electroneutrality can be descried in equation (3-8),

$$\sum_{i=1}^{s} z_i m_i = 0 \qquad (3-8)$$

The electroneutrality condition is valid on a macroscopic scale for every homogeneous part of the system but not for the boundary between two phases.

3.2 Dielectric Constant in Dipolar Liquids

The capacitance created by the presence of the material is directly related to the dielectric constant of the material. The electrostatic problem in treating hydrogen bonding and other dipolar liquids is to relate properly the molecular properties of the liquid molecules to the fundamental electrostatic equation,

$$(\varepsilon - 1)/4\pi = P/E \qquad (3-9)$$

Here ε is the dielectric constant of the liquid (ε_{water} =80), P is the polarization of the dielectric, and E is the strength of the electric field.[48,49,50,51]

3.3 Mobility of Protonic Charge Carriers

- **Ionic Diffusion in Solutions**

The ability of free ions to move in an electric field is described in terms of the ion mobility. [52,53] Ad hoc, ion mobilities are expected to be highest for highly charged small ions in solvents of low viscosity. But especially in highly polar solvents such as water this is not observed, i.e. the mobilities of small ions, such as Li^+, Mg^{2+} and Al^{3+}, are significantly smaller than the mobilities of large cations (e.g. K^+, Cs^+). The only exception is the protonic charge carrier, which has a mobility in water about five times higher than the average mobility of other monovalent cations. The reason is a special proton transport mechanism, which will be described in 3.4.

- **Ionic Conductivity**

The fundamental measurement used to study the motion of ions is that of the electrical resistance of the solution. The conductivity of a solution depends on the number of ions present, and it is normal to introduce the molar conductivity Λ_m, which is defined as

$$\Lambda_m = \frac{\kappa}{c} \qquad (3-10)$$

where κ is the ionic conductivity and c is the molar concentration of the added electrolyte.

If the limiting molar conductivity (when $c \rightarrow 0$) of the cations is denoted λ_+ and that of the anions λ_-, then the independent migration of ions states that

$$\Lambda_m^0 = \nu_+\lambda_+ + \nu_-\lambda_- \qquad (3-11)$$

where ν_+ and ν_- are the numbers of cations and anions per formula unit of electrolyte.

The conductivity of liquids that contain ions displays significant negative deviation from linear behaviour when the temperatures of these liquids approach their glass transition temperatures (T_g). The observed temperature-dependent conductivity behaviour of glass-forming liquids is often best described by the empirical Vogel–Tammann–Fulcher (VTF) Equation (3-12):

$$\kappa = AT^{-\frac{1}{2}} \exp\left(\frac{-B}{T-T_0}\right) \qquad (3-12)$$

where A and B are constants, and T_o is the temperature at which the conductivity goes to zero.[54,55]

- **Nernst-Einstein Relation**

The mobility of an ion is connected with its diffusion coefficient D, by the Nernst–Einstein relation. The following relation establishes the relation between an ion's mobility and its molar conductivity:[56]

$$\lambda = zuF \qquad (3-13)$$

where F is Faraday's constant ($F = N_A e$).

The link between the molar conductivity of an ion and its diffusion coefficient is given by the Nernst-Einstein relation (3-14),[57]

$$\lambda = zuF = \frac{z^2 DF^2}{RT} \qquad (3-14)$$

for each type of ion. Then, from equation (3-11) the limiting molar conductivity is

$$\Lambda_m = (\nu_+ z_+^2 D_+ + \nu_- z_-^2 D_-)\frac{F^2}{RT} \qquad (3-15)$$

which is the Nernst–Einstein equation. One application of this equation is the determination of ionic diffusion coefficients from conductivity measurements; another is the prediction of conductivities using models of ionic diffusion. From the comparison of data on charge transport (conductivity) and mass transport (diffusion) this contribution suggests some features of the proton conduction process.[58,59]

The applied Nernst-Einstein relation is only valid in the absence of any chemical potential gradient ($\nabla\mu_i$=0) and electrophoretic effects of the mobile species under consideration. This condition is fulfilled for the PFG-NMR diffusion measurement which does not produce any driving force on the mobile species which might disturb thermodynamic equilibrium.[60]

3.4 Proton Transport Mechanisms

• **Hydrogen Bonds:**[61,62] These bonds form between a covalently bound hydrogen atom and electronegative groups. In a water molecule, the two H atoms each provide a local positive region and the O atom provides a negative one. Hence a net attraction between H and O of different molecules results, if their mutual orientation allows this. The so formed hydrogen bond is to some extent like a covalent one, especially in the sense that it is direction dependent: a small deviation from the optimum orientation results in appreciable weakening of the bond.

• **The Hydrophobic Effect.**[63] If two hydrophobic molecules or groups in water come close together, negative solvation is diminished, which implies a decrease in free energy. This works as if an attractive force is acting between these groups, and this is called hydrophobic bonding. Such bonds especially act between aliphatic chains or between aromatic groups. The explanation of the hydrophobic effect and the resulting hydrophobic bonding is still a matter of some dispute. For instance, attraction due to dispersion forces may provide a considerable part of the interaction free energy of a hydrophobic bond, varying with the chemical constitution of the groups

involved. The explanation of the temperature dependence of hydrophobic bonding is especially intricate and controversial. The hydrophobic bonding strongly increases with temperature, especially in the range from 0 to about 60 °C.

- **Grotthuss mechanism (structure diffusion).**

The Grotthuss mechanism,[64,65] whereby protons transfer from one water molecule to the next via hydrogen bonding, is the usual mechanism given for proton mobility and is similar to that of auto-ionization, the mechanism causing the ions (H_3O^+, OH^-) to initially separate.[66,67]

Ions may separate by means of the Grotthuss mechanism but normally recombine within a few femtoseconds. The localized hydrogen bonding arrangement breaks before allowing the separated ions to return,[68,69] and the pair of ions (H_3O^+, OH^-) hydrate independently and continue their separate existence for about 70 μs (this lifetime also dependents on the extent of hydrogen bonding, being shorter at lower temperatures). They tend to recombine when only separated by one or two water molecules.

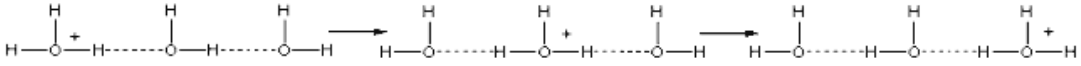

It is noteworthy that this process, although faster than translational diffusion, proves to be much slower than might be expected from its mechanism. This relative sluggishness may be due to the rotation of molecules required for proton movement and the consequential breakage of hydrogen bonds.[70]

After a proton has moved along a chain of water molecules, it is clear that this proton movement must be followed by a reorientation of the hydrogen bonding if further proton transferring through the same molecules and in the same direction is to proceed.[71]

A similar process was proposed for hydroxide mobility:

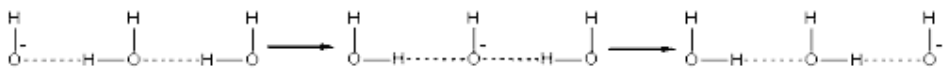

In order to migrate the ions must be associated with hydrogen bonded clusters; the stronger and more extensive the cluster, the faster the migration. Stronger hydrogen bonding causes the O···O distance to be

shorter, so easing the further shortening required for transfer. A limiting factor in the mobility for both ions is the breakage of outer shell hydrogen bonds. As a first step, this enables the hydrogen to transfer from H_3O^+ or, as a last step, the release of water by the newly formed hydroxide ion in H_7O_4.[72] Both transfers involve the additional energy requirements of stretching the outer hydrogen bonds due to the contraction of the O···O distance.

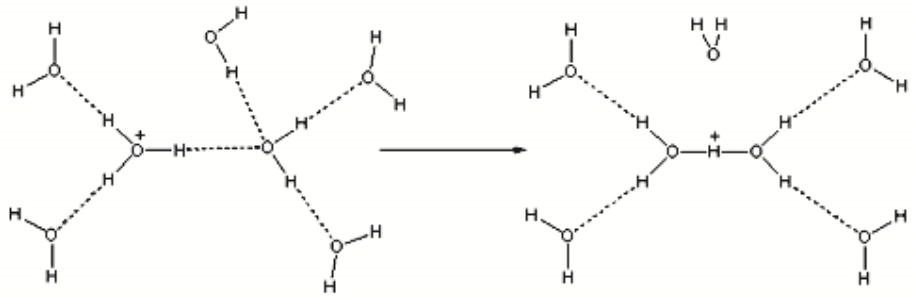

The symmetrical structure during proton transfer (above right), involving a triangular arrangement of water molecules,[73] has also been found in the protonated trimer ($H_7O_3^+$ [74,68]). The presence of the fourth water molecule associated with the $H_9O_4^+$ cluster is seen in a neutron diffraction study as oriented but distant (3.2 Å[75]). Proton transport may also occur using 'Zundel' dihydronium ($H_5O_2^+$) ions only,[76] which involves the concerted movement of two molecules. Such proton jumps may be short or long. This mechanism was favored by *an* ab initio simulation[77] where $H_5O_2^+$ mobility was induced by thermal movement in the second solvation shell. An external electrical field was found to ease the process by orienting the water in its direction.[77]

4 Experimental Section

Several complementary techniques were used in order to study the systems described in this thesis. This chapter gives a short description of the hardware, sample preparations and the experimental methods used in this work, including the schematic setups of the basic parts of the NMR spectrometer, the Pulse Field Gradient unit (PFG), the Thermogravimetric Analyzer (TGA) spectrometer and the home-built cells required for the electrical measurements. High resolution NMR will also be briefly described.
A specification of sample preparations and experimental conditions are given right after the experimental setups.
The experimental details also include the data pre-analysis and the required hardware and software calibrations are provided.

4.1 Experimental Setups

The following subsection gives a short description about the spectrometers and the hardware devices for the NMR, PFG-NMR, TGA analyzer and AC-impedance analyzer.

4.1.1 NMR Spectrometer

The measurements have been performed with a home-built PFG-NMR spectrometer operating at around 50 MHz, ($B_0 \approx 1.2$ T).
The schematic spectrometer setup is shown in Figure 4-1. Besides the magnet, the most important units of any NMR spectrometer are the radio frequency generator, radio frequency mixer, pulse generator, the amplifier, and the receiver. In our machine, the r.f.-pulse generation and the signal detection are achieved with the help of two independent subsystems. Both units are connected and operated by a central VAX computer using the stable operating system VMS (see Figure 4-1). The input of the experimental parameter values can be achieved via the control program on the central computer using a macro programming language.
The r.f. resonant circuit of the sample holder is separated from the r.f. amplifier by a pair of crossed diodes. Due to their large differential resistance only large r.f. amplitudes may reach the resonant circuit. A $\lambda/4$-cable

connecting the signal and the detection unit ensures that the r.f. power is fully absorbed in the resonant circuit. A small NMR signal does not affect the crossed diodes. The entire signal thus arrives through the $\lambda/4$ cable to the acquisition unit.[78]

The r.f. resonant circuit is formed essentially by the r.f. coil and the tuning capacitors. The tuneable capacitor is connected in series to the coil; the resonant frequency can be shifted within a certain range. Additionally, a second ("matching") adjustable capacitor is connected in parallel to the resonant circuit. This capacitor helps to adjust the probe head to have the required wave resistance of 50 Ω which is adjusted at the output impedance of the r.f. amplifier. The electromagnetic radiation in the r.f. coil produces a magnetic field component B_1, which flips the nuclear spins from their equilibrium orientation (B_0 direction) (see Chapter 2). A signal acquisition in time domain is performed using a transient recorder with phase-dependent quadrature detection. This unit can also be operated via the central VAX computer.[79,80] Fourier transformations of the measured free induction decays (FIDs) as well as the initial evaluation of the relaxation times (T_1, T_2), and diffusion coefficients D are all computerised.

4.1.2 PFG-NMR Spectrometer

The home-built spectrometer which is based on predecessor versions was modernized in various steps. Figure 4-1 shows the PFG-NMR spectrometer which essentially consists of three separated parts; the high frequency pulse generator, signal detector and the magnetic field gradient pulse generator. Since the NMR spectrometer was described in the previous section, this section presents only the experimental setup of the PFG unit.[79,80]

The pulsed field gradient generator creates a static and stable current pulse up to 120 A through the gradient coil. The current can be varied is steps of 1.875 A. The coil is an anti-Helmholtz type, which is cooled with water to avoid the overheating due to the pulsed electrical current. This home-built gradient coil can create a magnetic gradient up to 50 T / m corresponding to 120 A through the gradient coil.

The background current can be applied continuously up to 1 A. An external shielding coil is placed to actively shield the gradient coil. The main idea of actively shielding the gradient coil is to prevent the inducted eddy currents in the room temperature bore of the magnet, The gradient coil and the external shielding coil are connected in series to allow the same electrical current to flow in order to shield actively.[78,81]

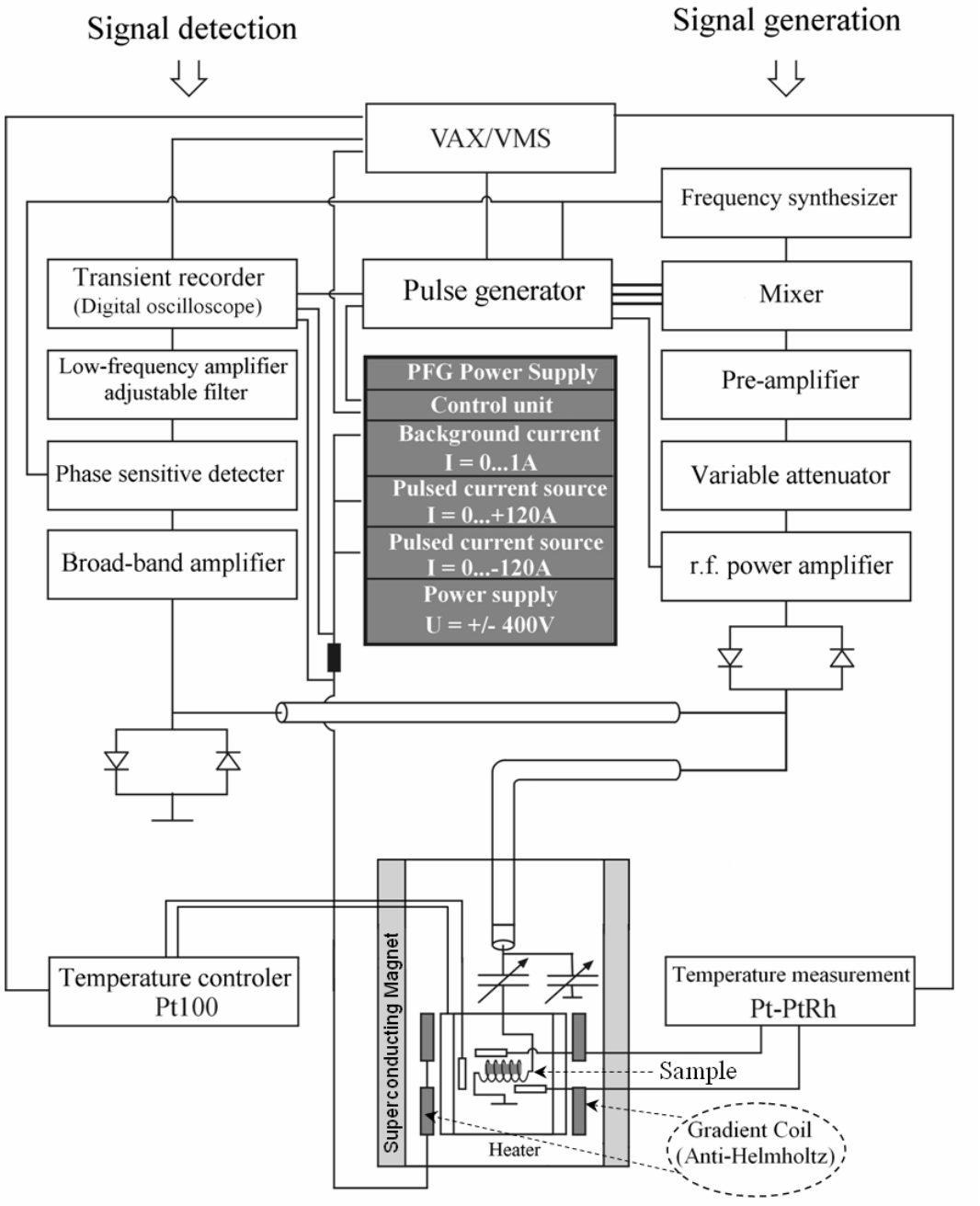

Figure 4-1: *Schematic setup of the home-built PFG-NMR spectrometer.*

Figure 4-2 shows separately the entire setup and the gradient coil.

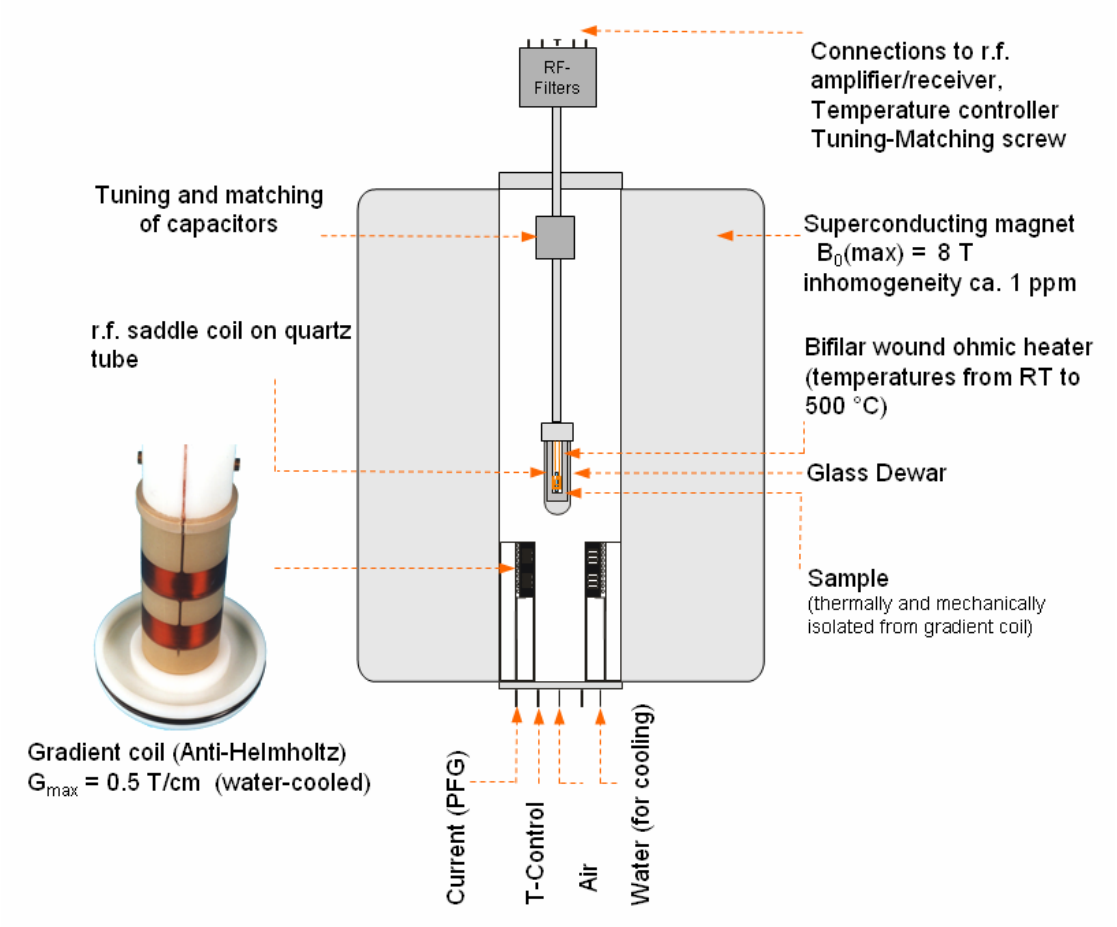

Figure 4-2*: The home-built Anti-Helmholtz gradient coil: left. PFG-NMR setup showing the magnet, water-cooling connections, air-cooling, temperature control, gradient coil position, the probe heat and its connection with the amplifier and the other external connection: right.*

In order to find the exact value of the magnetic field gradient at the sample, it is necessary to calibrate the gradient coil in order to determine the coil constant (*S*). The coil constant is the ratio of the corresponding magnetic gradient to the particular electrical current through the coil.

The calibration is done by using a solid Teflon cylinder with several identical holes made on the surface perpendicular to the main axes. This Teflon cylinder with holes is placed inside the probe-head and a simple FID measurement was done with existing background gradient. The NMR spectrum illustrates the distribution of the spatial magnetic field values which

are different from one hole to the next hole in the Teflon calibrating sample. In other words, different Larmor frequencies are obtained at the position of each hole. Figure 4-3 shows the spectrum of the calibrating sample with nine holes that are filled with D_2O. The intensity of the lines in the NMR spectrum near the ends of the spectrum decreases because the spectrometer's filters filter out frequencies that are outside the spectral width.

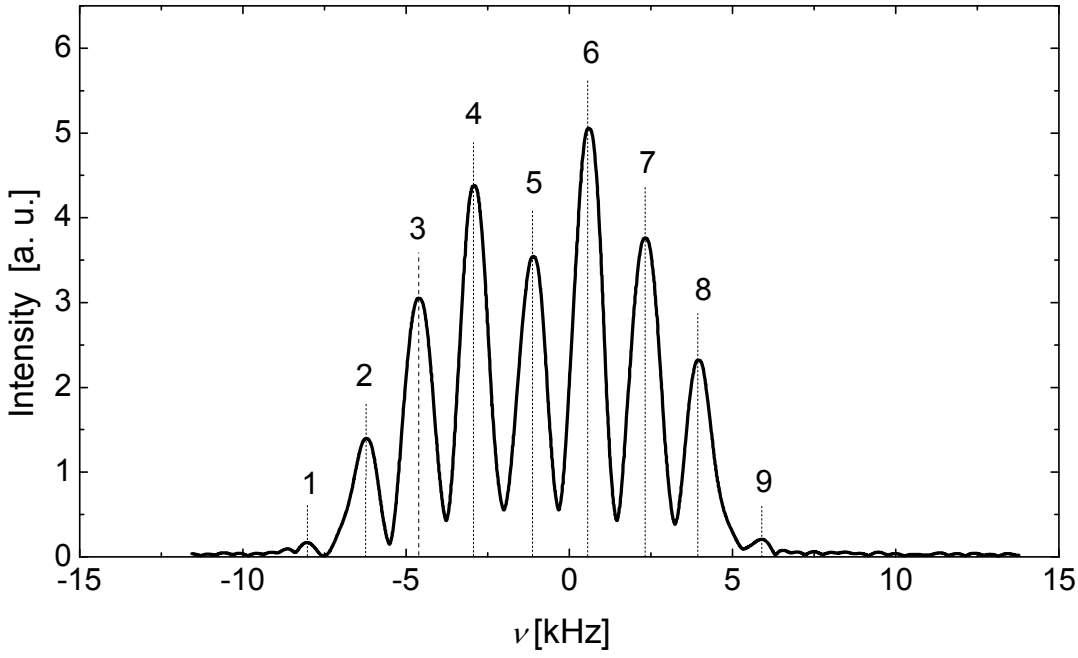

Figure 4-3: *NMR spectrum of the calibration sample D_2O, this multi peak spectrum is used to determine the gradient coil constant (S). Every peak corresponds to an NMR active hole in the calibration sample.*

The gradient coil constant is given by Equation (4-1).

$$S = \frac{\Delta\nu \cdot 2\pi}{\gamma \cdot \Delta r_i \cdot I} = 40.244 \frac{\text{Gauss}}{\text{cm A}} = 0.40244 \frac{\text{Tesla}}{\text{m A}} \qquad (4-1)$$

According to the Figure 4-3, the frequency difference between the two lines is $\Delta\nu$ = 1694.5 Hz, and Δr_i (i = 2 to 8) is the distance between two successive holes which is equal to 0.1988 cm, and the gradient coil electrical current is 0.324 A. So the gradient coil constant (S) is 0.40244 T/mA.

4.1.3 High Resolution NMR Spectrometer

High resolution ^{1}H-NMR samples have been measured by using a 300 MHz (B_0=7.05 T) NMR Bruker spectrometer (AVANCE DPX-300 SB). The probe head is designed for a temperature range from -80° to 100° C. The NMR sample container is a 5 mm borosilicate glass tube; it can be sealed with a cap or sealed permanently with a focused flame.

The high resolution NMR spectra are obtained by Fourier transformation of the FID signal. The processing of the data is done by the Bruker software for NMR signal analysing "XWIN-NMR" and "XWIN-PLOT".[82,83]

4.1.4 AC-Impedance Analyzer

The electrical conductivity measurements were performed using an AC-Impedance analyzer manufactured by HP model 4192A LF. The Impedance Analyzer is a fully automated instrument designed to measure a wide range of impedance parameters, such as phase angle, real and imaginary components of the impedance, admittance, conductance and capacitance. The HP Impedance analyzer gives the impedance and phase angle of the specimen by varying the applied frequency.

4.1.5 Conductivity Cell for Liquids

The home-built conductivity cell for liquids which is mainly based on the two platinum electrode cells has been used to measure the liquid samples. The geometry of the cell including the sample chamber, the electrodes holder, and the heating components are redesigned in order to obtain a closed system such that measurements can be done under a controlled atmosphere such as N_2 or air. The double layer glass sample chamber allows the silicon oil to flow in between the double layer to achieve a proper heating and cooling within high stability and accurate temperature, An external commercial cryostat is connected to the conductivity cell with inlet and outlet pipes, a suitable liquid is chosen to be used in the pump to achieve heating and cooling. The temperature control and the data acquisition are done by an external computer. Figure 4-4 illustrates the cell

with the external commercial cryostat pump and the AC-impedance analyzer.

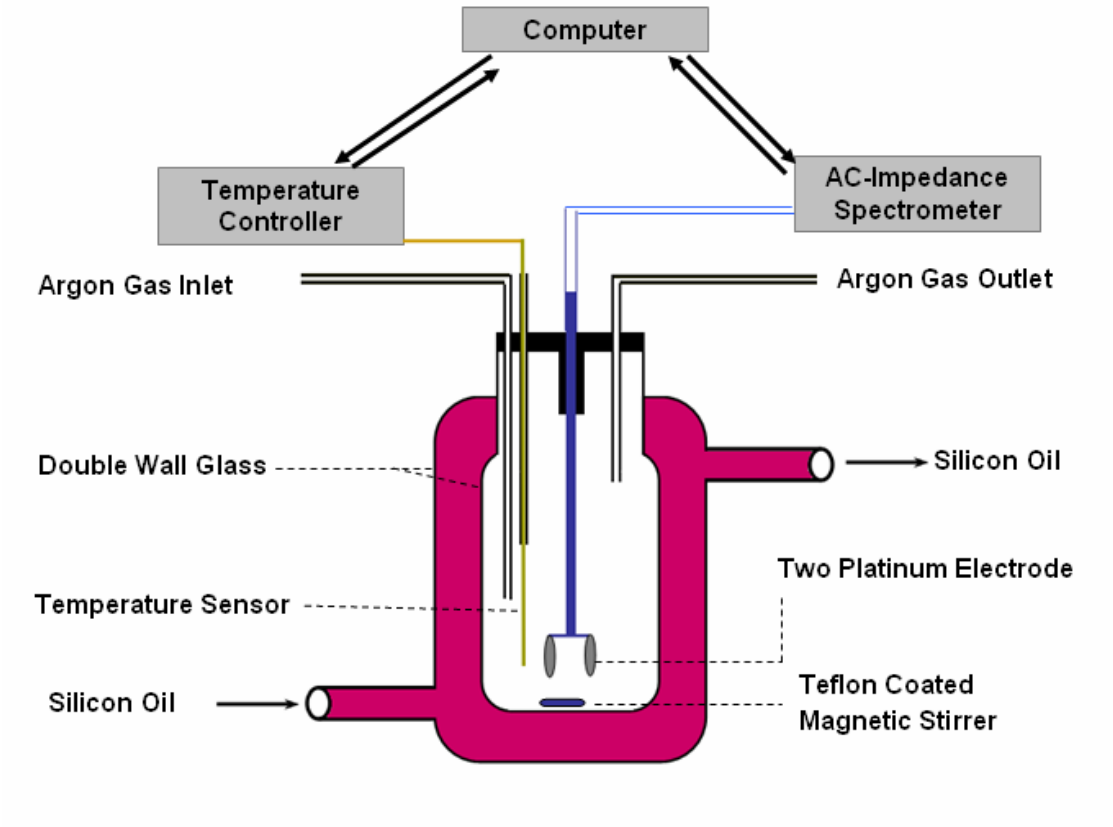

Figure 4-4: *The home-built two platinum conductivity cell for liquids. The cell consists of double layer glass walls, which are connected to the inlet and the outlet of the heating and cooling fluids, two platinum disks as electrodes, sensor for measuring and controlling temperatures, inlet and outlet pipes for injection argon or other gases, a glass electrode holder that also constructed to seal the cell, external cryostat and computer.*

4.1.6 Conductivity Cell for Membranes

The concept of the home-built two platinum electrode cell which is explained in the previous section has been used to measure the electrical conductivity of membranes. The geometry and the design of the cell had been modified in order to achieve variable measuring conditions. Conductivity of the membranes is typically measured at different degree of hydration. Hence, a humidifier has also been built, it is mainly consists of a distilled water container connected to a controllable flow fine pump; the pumped water

passes through a narrow glass tube where it is heated and controlled with an Eurotherm unit, the pumped water evaporates and heated to match the operating temperature of the cell.

The sample is placed in an opened ended cylindrical glass filter to allow the thermal and the water vapor exchange between the sample and the adjusted internal atmosphere, the sample is squeezed between the two gold coated electrodes that are connected to the AC-impedance analyzer. The heating of the sample and the temperature control are done by a thermostat pump; silicon oil is heated and pumped through a particular path in order to heat homogenously the internal parts of the cell and the sample. The electrode holders are used to center the electrodes and to press the sample correctly; they also close the two ends of the cell from the external atmosphere. The electrode holders made of PEEK do not show degradation at the operating temperatures. The details of the conductivity cell of the membranes and pressed powder is shown in the Figure 4-5 including the humidifier.

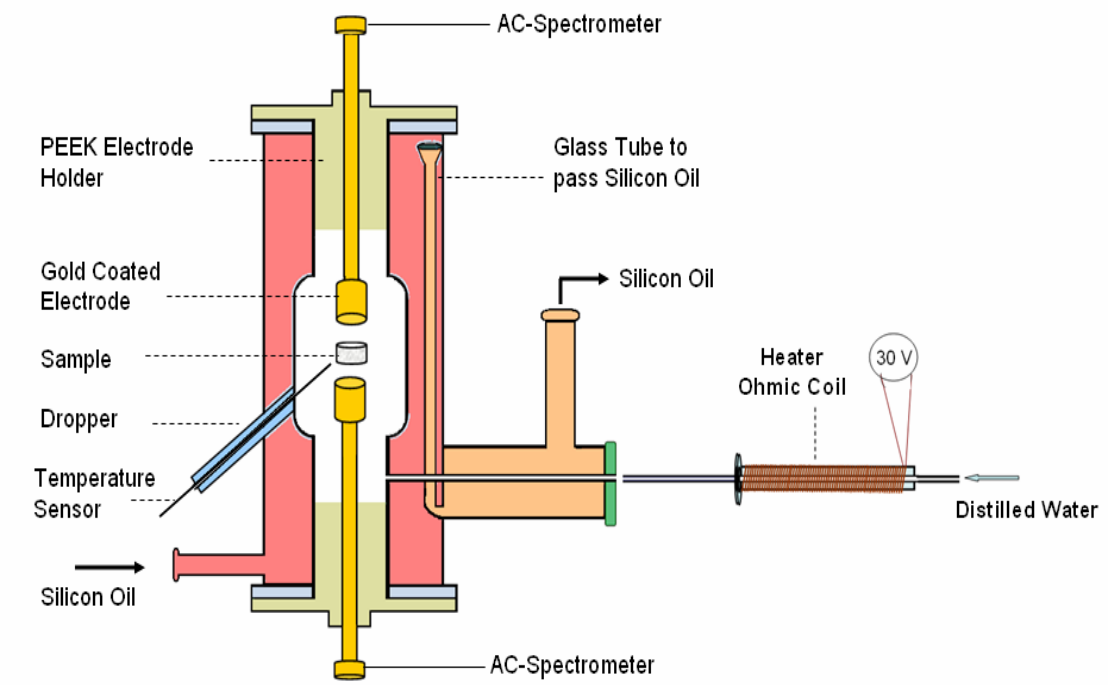

Figure 4-5: *(a) The home-built two gold coated electrode cell for measuring conductivity at different atmospheric pressures, humidity degrees, and atmospheric media such as N_2 or air. (b) The humidifier unit which is mainly a heater controlled by Eurotherm controller, and the controllable water pump with the water vessels.*

4.1.7 Thermogravimetric Analysis (TGA) Spectrometer

TGA spectrometer is a vertical balance from Rubotherm which has a specimen pan hanging from the balance (TA Instruments, etc). This suspension balances makes it possible to weigh samples without physical contact under nearly all environmental conditions. The sample under investigation doesn't hang directly from the balance. Instead the sample is linked is linked to a so-called suspension magnet, which consists of a permanent magnet, a sensor core and a device for decoupling the measuring load (sample). An electromagnet, which is attached to the underfloor weighing hook of a balance, maintains a freely suspended state of the suspension magnet via an electronic control unit. Using this magnetic suspension coupling the measuring force is transmitted contactlessly from the measuring chamber to the microbalance, which is located outside the chamber under ambient atmospheric conditions. Consequently, this arrangement eliminates almost all restrictions which are inherent to conventional gravimetric measuring instruments. A controlled suspended state is achieved by means of a direct analogous control circle (PID controller and position transducer). This modulates the voltage on the electromagnet in such a way that the suspension magnet is held constantly in a vertical position. A microcontroller driven digital set point controller superimposed to the direct PID controller allows various positions of the suspension magnet (see Figure 4-6).

It is necessary to calibrate these instruments in order to compensate for buoyancy effects due to the variation in the density of the purged gases with temperature.

The measurement is normally carried out in air or in an inert atmosphere, such as helium or argon, and the weight is recorded as a function of increasing and decreasing temperature.

The heating and cooling in the homebuilt sample chamber is done by using a cryostat connected to this double layer closed chamber flowed with silicon oil.

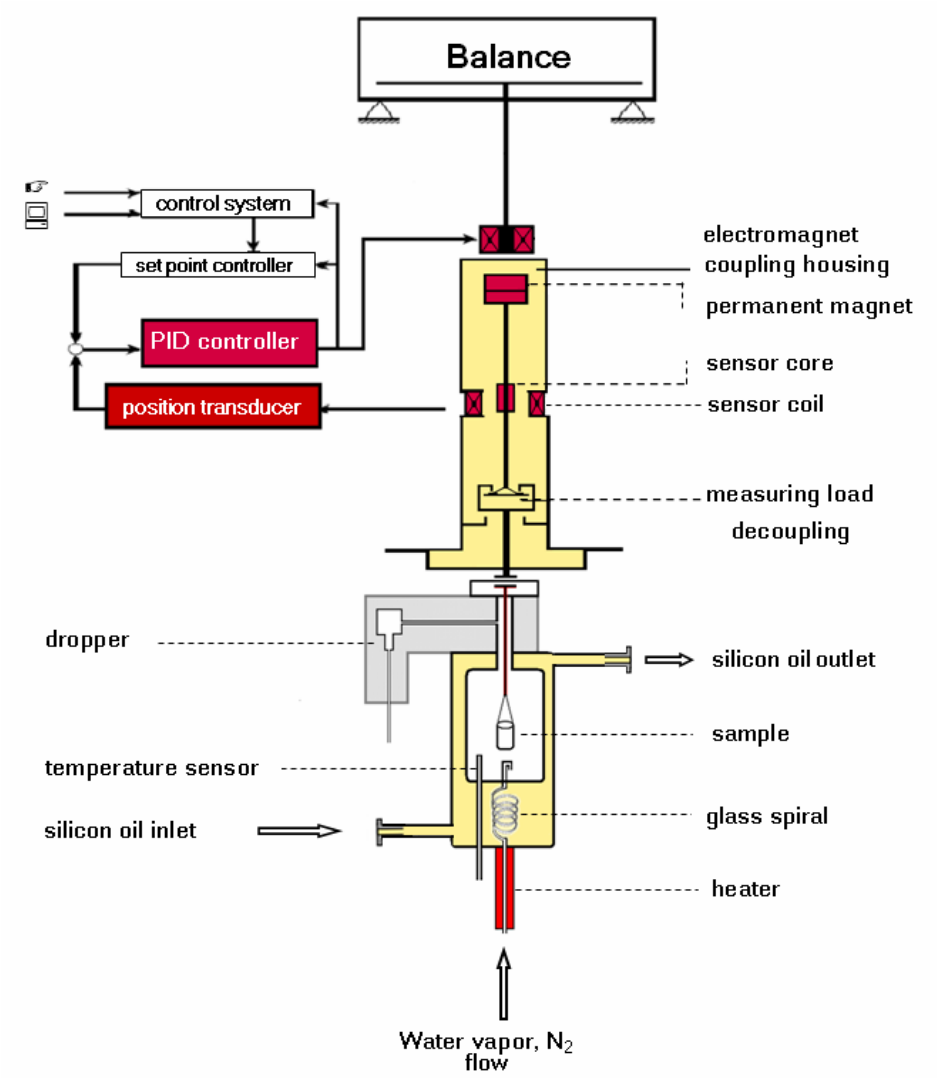

Figure 4-6: A schematic diagram of magnetic suspension balances that it used to weigh samples contactlessly under nearly all environments. Instead of hanging directly at the balance the sample to be investigated is linked to a so-called suspension magnet which consists of a permanent magnet, a sensor core and a device for decoupling the measuring load (sample).

The sample chamber has an inlet for the water vapor which passes from the evaporator in a particular evaporating rate to ensure a full water vapor atomosphere. The outlet of this chamber allows the water vapor or the gas to leave the chamber and condense on the external part of this outlet pipe blocks any possible access of air from outside into the sample. Eurotherm temperature controller is used to control the evaporator temperature.

4.2 Samples Preparation

4.2.1 NMR Samples

Several different samples have been measured using NMR and PFG-NMR like MSA-[water, water-alcohols] and real sulfonated membranes.

The samples for NMR-measurements were prepared carefully from the highest purity materials and solvents. MSA, ethanol and isopropanol have been kept in the argon glove-box. Whenever water has been used, only the freshly prepared deionised bi-distilled water was taken.

The hygroscopic samples have been prepared in the argon glove box to avoid water contamination. For the NMR experiments, the samples have been transferred to 9 mm borosilicate glass NMR tube with a good filling factor. The NMR tubes are connected to a vacuum pump and are subsequently purged with fresh argon gas for several cycles. Finally 800 mb of argon atmosphere pressure was set in the sample tubes. The NMR tubes are sealed using a focused flame in the glass technique service. In order to avoid over heated the samples during the sealing, the NMR tubes have been cooled down sufficiently with liquid N_2.

4.2.2 High Resolution NMR Samples

High resolution NMR samples are prepared from the same materials as the samples for other measurements; by this way we ensure that all samples for different measurements are identical. The samples were filled in standard 5 mm NMR-glass tube. 1 mm glass capillary are filled with deuterated chloroform ($CDCl_3$) and placed inside the NMR tube as a frequency lock to avoid any frequency shift due to different sample or external magnetic field.

All measured high resolution NMR signals are compared to the standard reference signal. The standard reference is Tetramethylsilane $Si(CH_3)_4$ or $SiMe_4$ (Me = CH_3) which is commonly abbreviated (TMS).[84]

4.2.3 Conductivity Samples (Liquids and Membranes)

- **Liquid solution**

MSA-water, MSA-water-(ethanol, isopropanol) mixtures are liquid samples in the temperature range of the measurements. The mixtures are prepared

sufficiently for all different experiments. The conductivity cell (explained in section 4.10) is used to measure the electrical conductivity for these liquid samples. The ideal and the experimental mass densities of the mixtures have been measured during the preparations.

- **Membrane Samples for a Conductivity Measurement under Partial and Full Water Vapor Pressure Atmosphere.**

The sulfonated proton exchange membrane was standardized before measurement. The standardization (transformation in acid form) is a chemical treatment procedure for the polysulfone membranes. The treatment can be abbreviated in the following steps.

1. Soaking in 10 wt % sulfuric acid for 12 hours at room temperature.
2. Immersion of the membranes for 24 hours in distilled water.
3. 1 and 2 are repeated for several cycles.

After standardization the membrane has to be kept under distilled water and sealed environment.

In the case of Nafion Membrane the same concept of treatment has been applied. The entire standardization procedures are as the following:

1. Soaking the Nafion samples in 2N HNO_3 at 70° C for two hours. After that the heating is switched off and the sample is kept in the acid solution around 12 hours.
2. The membranes were immersed for 24 hours in distilled water and the water was changed for 6 times during these hours. The standardized membranes are a stored in closed environment, however under distilled water.

4.2.4 TGA Samples

TGA has been used to measure water uptake in the real sulfonated membranes like Nafion and polysulfonated samples.[85] The samples had been standardized identically like the samples for the conductivity measurements in order to compare and to interpret the results using the same reference treatment conditions.

4.3 Experimental Details

4.3.1 Spin-Echo Experiment with Pulsed Magnet Field Gradients

The standard PFG Hahn echo pulse sequence has been performed to determine the tracer diffusion coefficient for the MSA-water system. Particularly the experimental results of the MSA·$(H_2O)_3$ sample are shown as an example in the following Figure 4-7.

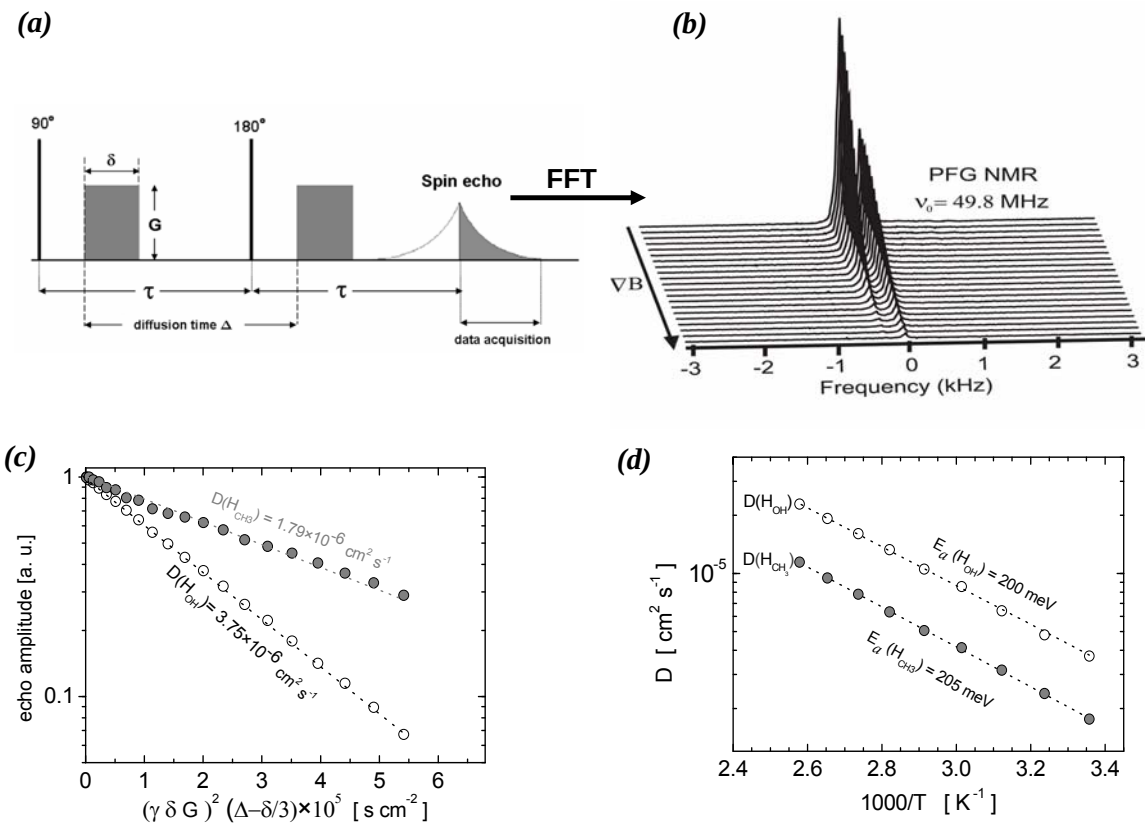

***Figure 4-7**: Hahn echo measurements of the MSA·$(H_2O)_3$ at room temperature at around 50 MHz NMR resonance frequency. **(a)** the standard Hahn echo pulse sequence (see Section (2.3.2)), **(b)** 3D-polt of several NMR echoes generated by using Hahn echo technique, the echoes amplitude was attenuated incrementally with increasing the gradient strength in the measurement, **(c)** The echoes amplitude (magnetization) versus the gradient strength, from the slope of the fitting line of the points to the equation , the coefficient of tracer diffusion can be obtained, in this case two different diffusions are obtained due to the two different types of protons in OH and CH_3 groups, within the single measurements, **(d)** The temperature dependent PFG NMR diffusion measurement, the two different data set belong to the two proton types (H_{OH}, H_{CH_3}), the fitted lines to the two different data sets give the activation energies of the long range diffusion process.*

4.3.2 Spin-Lattice Relaxation Time (T_1) Measurement

The spin-lattice relaxation (T_1) changes the longitudinal component of the magnetization M_z, until the Boltzmann equilibrium is reached. In many cases, the changes in M_z can be described as a simple exponential function with a time constant T_1 (see Equation (2-41)). The most common applied technique for measuring T_1 is the inversion recovery method, which has been used in the experiments. The pulse sequence is shown schematically in Figure 4-8(a). It consists of 180° r.f. pulse which is called the inversion pulse and then after a time interval τ, a 90° r.f. pulse is applied which is called the detected pulse. The first pulse inverts a magnetization along Z-axis from M_z to -M_z, the second 90° pulse turns the magnetization to a transverse plane where it can be detected as FID directly after the second pulse as a function of the time interval τ. The experiment must be repeated for a series of different τ values. In practice, one can replace the initial FID amplitude measured after the 90° pulse by the area under the spectrum. By repeating the measurements using the same pulse sequence and varying the time interval between the two r.f. pulses, several NMR spectra will be obtained, in a 3D-plot which is shown in Figure 4-8(b). From the variation of the nuclear magnetization with the time interval τ, one obtains T_1 by fitting the data to the following equation.

$$M(\tau) = M_0 \left[1 - 2 \cdot \exp\left(-\frac{\tau}{T_1} \right) \right] \qquad (4-2)$$

The measured sample contains two different type of protons which are obvious from the peaks in the NMR spectrum, so from a single T_1 measurement, two T_1 values are obtained for (H_{OH}, H_{CH_3}), this is shown in Figure 4-8(c). The T_1 measurements have been done over a temperature range from room temperature to 380 K. By fitting the temperature dependent data of the relaxation rate to the following Arrhenius equation (4-3), obtained from equation (2-29), the activation energy of motional process will be obtained.

$$\Gamma(T) = \Gamma_0 \exp\left(\frac{E_a}{K_B T} \right) \qquad (4-3)$$

Two different activation energies are expected because of the two different proton types in the measured samples, Figure 4-8(*d*) shows the Arrhenius fitting to the relaxation rate data and the activation energies of (H_{OH}, H_{CH_3}).

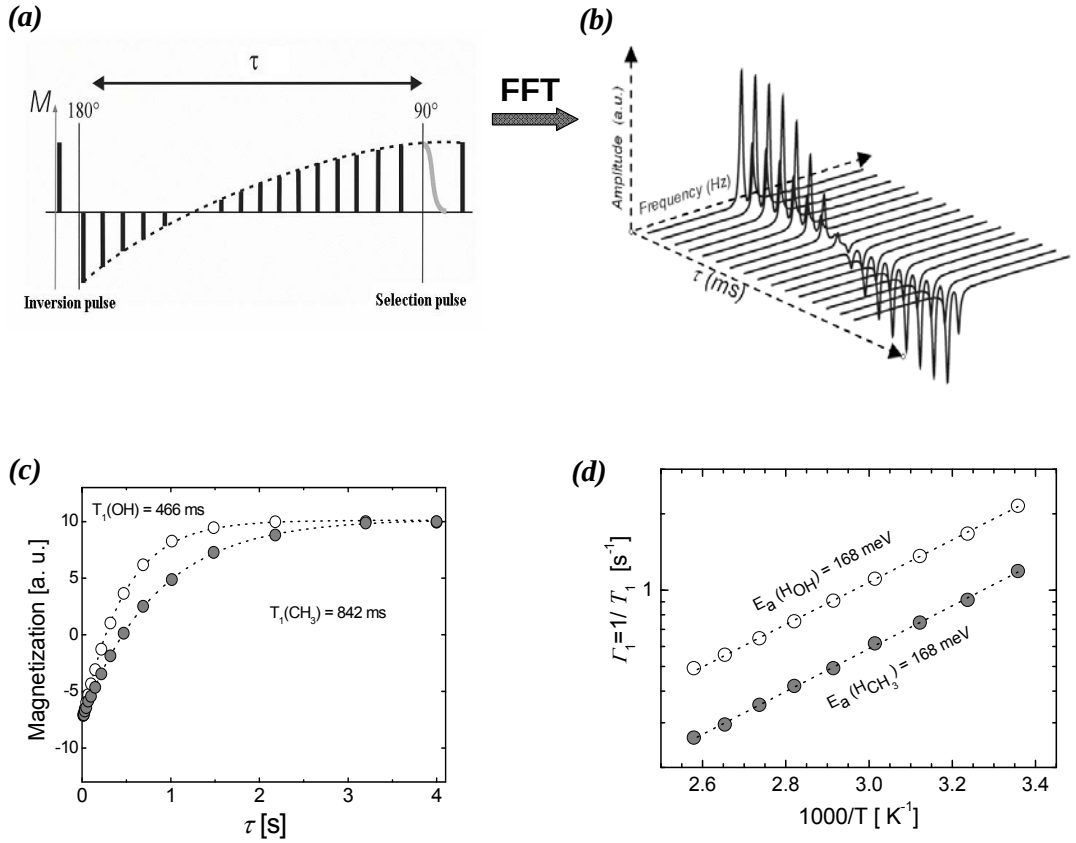

Figure 4-8: ***(a)*** *The inversion recovery pulse sequence for measuring spin-lattice relaxation time (T_1).* ***(b)*** *3D-polt of the NMR spectra for the sample MSA·$(H_2O)_3$, generated by the inversion recovery pulse sequence at room temperature and at about 50 MHz NMR resonance frequency.* ***(c)*** *The magnetizations (the areas under the NMR spectra plotted versus the time between the inversion pulse and the detection pulse (τ)), the sample spectrum has two lines; H in OH group the open circles in the plot and H in CH_3 group the solid circles. Theses two fitted curves to the circles give us the spin lattice relaxation time for H in the two different groups.* ***(d)*** *The temperature dependent T_1 measurement, the fitted lines to the two different relaxation rate data of (H_{OH}, H_{CH_3}) give the activation energies of the local diffusion process.*

The temperature stabilization was achieved by a sufficient waiting time between the successive measurements. The applied 90° pulse length

typically between 3.5-4.5 μs, and a delay time between the detection pulse and the data acquisition of t =10 μs.

4.3.3 Conductivity Measurements

- **Electrical AC-Impedance Experiment**

In experimental process, and in many other applications, electrical parameters such as the electrical conductivity and dielectric constant of certain liquid solutions and dielectrical material fluids have a substantial impact. In such industries and applications, real-time monitoring of the fluid's electrical parameters can be of significant importance.

The AC electrical measurements were taken in the frequency range from 100 kHz to 2 MHz at different temperatures. The measurements were performed using an AC-impedance analyzer.

- **Conductivity Experiments for Liquids**

The conductivity of liquid samples depends on the concentrations of the various ionic species and their abilities to transport electric charges in a solution, i.e. the ion species equivalent conductivity. This conductivity is temperature dependent and increases with increases temperature in aqueous solutions for most ion species.

The samples (MSA-water, MSA-water-(ethanol, isopropanol)), and polymeric fuel cell membranes have been measured. The prepared sample placed in the conductivity cell and then after the cell is sealed and the argon atmosphere is applied. Three hours waiting time was required between the two successive measurements at two different temperatures. The conductivity data derived from the resistance by using the calibration curve of the cell. The calibration process and the calibration cure are explained in the following section.

- **The Calibration of the Conductivity Cell of Liquids**

Conductivity cells and the external electrical connections including the impedance meter must be calibrated before the first use.[86] The measured resistance (R) across the electrodes is proportional to the electrical conductivity (σ) of the fluid with which they are in contact. The proportionality factor, called the cell factor (Z), is theoretically derivable from the geometry

of the electrode configuration, with possible geometries including pairs of parallel plates.[87] Measurements on conducting liquids are complicated by ionic conductivity and by the effects of electrode polarization.[88] The known proportionality factor combined with the measured resistance or conductance yields a determination of the electrical conductivity of the solution. Since the resistance and proportionality factor (cell factor) are known, the electrical conductivity of the liquid is obtained. The cell factor (*Z*) is proportional to the distance between the electrodes (*L*) and inversely proportional to electrode surface area (*A*), which can be written in Equation (4-4).[89,90]

$$Z = \sigma \cdot R = L / A \qquad (4-4)$$

The calibration for the home-built conductivity cell has been done at three different calibration points using a standard commercial solutions of $(KCl)_{aq}$ (Potassium Chloride solution) in certain molarities (see Table 4-1), *R* has been experimentally quantified for the three calibration salt samples using impedance spectroscopy, and then *Z* is calculated from Equation (4-4), the calibration data are shown in Table 4-1.

$(KCl)_{aq}$ [mole/l]	σ [mS·cm^{-1}]	R [Ω]	Z [cm^{-1}]
0.01	1.41	324	0.45684
0.1	12.88	36.4	0.46592
1	106.40	4.62	0.49170

Table 4-1: *The calibration results of the three $(KCl)_{aq}$ calibration salts performed by AC-impedance analyzer, in a frequency range from 10^3 to 10^5 Hz.*

Determining the cell factor from a single calibration point is valid when the current path is invariant with the electrical properties of the investigated liquids and the electrodes, and the cell factor is constant in this case. In the two platinum electrode technique, the current path is not totally confined. Current spreads out in all directions to an extent dictated by the electrical properties of the liquid (electrical conductivity (σ), and dielectric constant (ε)) and the proximity of the electrodes to the cell walls. So the cell factor so

determined is in fact not constant, but an unknown function of the electrical conductivity and the dielectric constant of the investigated liquids.[91] In order to overcome this uncertainty, calibration is carried over a three calibration points, *Z* is considered as a function of the calibration liquid conductivity, by the cell calibration the uncertainty in obtaining (σ) is reduced, furthermore the cell covers a wider measuring range by extrapolation the calibration line. Figure 4-9 shows the plot of *Z* versus *R* for the home-built conductivity cell.

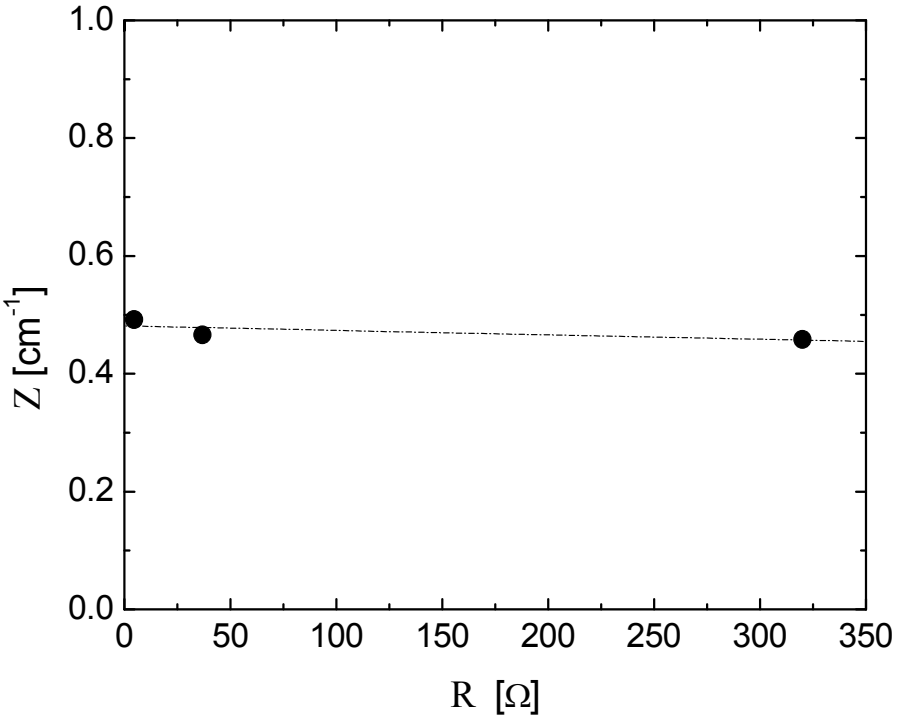

Figure 4-9: *The home-built conductivity cell calibration points from Table 4-1. The calibration including the meters and the connections is carried on frequency range from 10^3 to 10^5 Hz at 25 °C. Calibration points fitted linearly and extrapolated for a wider experimental range of resistance.*

The linearly fitted line to the experimental calibration points is the cell constant, which can be described linearly as in the Equation (4-5).

$$Z = 0.48112\ \ cm^{-1} - 7.5343\times10^{-5} R\ \ \Omega^{-1}\cdot cm^{-1} \qquad (4-5)$$

So the electrical conductivity can be written as follows

$$\sigma = \frac{0.48112\ \ cm^{-1} - 7.5343\times10^{-5} R\ \ \Omega^{-1}\cdot cm^{-1}}{R} \qquad (4-6)$$

A complete standard range of conductivity calibration solutions and a higher frequency range can be performed for highly accurate required measurements.

In the case of (gel like mixtures) the conductivity cell consists of two platinum electrode fixed in a slim glass tube, the heating is done in an external oven, the same calibration procedures are required.

- **Conductivity Experiments of Membranes**

The electrical conductivity of membranes under different atmospheres such as full and partial water vapor pressure, normal atmosphere, and N_2 gas has been measured. The full water vapor atmosphere is demanded for many measurements on protonic conducting materials and media, in order to measure the electrical conductivity at full water pressure, the cell has been fed with a sustainable flow of water vapor, which has been achieved by humidifier (see Figure 4-5).

Several discs with 8 mm diameter of membrane samples are placed over each other in an opened ended cylindrical glass filter to allow the thermal and the water vapor exchange equilibrium between the sample and the adjusted internal atmosphere, the sample is squeezed between the two gold coated electrodes which are parts of the home-built conductivity cell (Figure 4-5). Between the sample and the gold coated electrode, we used two soft and thin carbon-platinum electrodes to improve the electrical contact to the rough surface of the samples.

The cell factor (Z) is calculated from equation (4-4) by using the measured thickness of the sample (L) and the surface area (A) of the electrode disk with a diameter of 8 mm.

The cell has been calibrated in order to determine the effect of cables and the gold coated electrodes and the carbon-platinum electrode. The resistance of the cell without a sample is lower than 0.15 Ω over the entire temperature range covered by the measurements. This value is negligible compared to the electrical receptivity of the samples and has no serious effect on the experimental results.

The required temperature is adjusted directly from the thermostat. The samples need around 12 hours waiting time in order to reach the equilibrium state before acquiring the data. The conductivity data has been obtained from the resistant data by using Equation (4-4). The entire obtained data set has been analyzed and plotted with Origin 7.5 software.

4.3.4 Thermogravimetric Analysis (TGA) Measurement

The measurements have been performed in the temperature range slightly above 100° C to 180° C for several heating and cooling cycles. Heating and cooling are symmetric and linear process with 20° C per hour as a heating and cooling rate. Waiting time of 8 hours is required at the end of the heating or cooling side within a single full cycle in order to stabilize and homogenate the hydration in the sample. Several full cycles are required for every measured sample. At the end of the measurement and before removing the sample out off the its chamber, a stream of dry N_2 flow through the sample chamber at 140° C temperature and for an entire day time. This final procedure is important to dry the sample and then to obtain the absolute water content in the equivalent material weight of the sample.

The heating and cooling process beside the temperature stabilization in the home-built sample chamber is done by using a cryostat connected to this double layer closed chamber flowed with silicon oil that stands high temperature.

The sample chamber has an inlet for the water vapor which passes from the evaporator in a particular evaporating rate to ensure a full water vapor pressure. The outlet of this chamber allows the water vapor or the gas to exit out of the cell. Water vapor condenses in the external part of the cell outlet pipe and blocks the air to access into the cell from outside. Data analysis is processed in different software packages (Sigmaplot 8, Orgin 7.5). Fresh calibration and offset line were done for every single sample individually.

5 Results and Discussion

The NMR spectra give us information about the dynamics of protons in the studied samples.[10] From the spin-lattice relaxation rate Γ_1 some important parameters of proton diffusion such as the activation enthalpy H_a, the relaxation strength (second moment) M_2, and the pre-exponential factor τ_o can be calculated.[10]

The ^{1}H-NMR spectra of MSA-water and MSA-water-alcohol systems at temperature range about 300-360 K have been studied. The line narrowing above room temperature will be explained in terms of motional narrowing. The activation enthalpy H_a for long range proton motion was calculated from Arrhenius plot of temperature dependent self diffusion data.

The protonic charge carriers concentration, and the dissociation constant of the aqueous systems have been calculated from the experimental data of high resolution ^{1}H-NMR chemical shift.

The electrical conductivity calculated from the self diffusion data by using Nernst-Einstein relation are compared with the directly measured electrical conductivity. The transport mechanism type has been obtained and explained based on this comparison. The experimental data of the electrical conductivity are considered as an upper limit for the protonic conductivity of any sulfonated membrane.

Finally, measured conductivity data at different water content and different atmospheric pressure in real sulfonated membranes are presented.

5.1 MSA-Water System

5.1.1 ^{1}H-NMR Spectrum of Pure MSA and MSA-Water Mixtures

^{1}H-NMR spectra of MSA and MSA-water mixtures have been obtained by Fourier transformation of the FID (Free Induction Decay). A low resolution NMR spectrum of dry MSA was enough to distinguish between the individual peaks within the NMR spectrum. Each peak represents a different environment for hydrogen atoms within a MSA molecule. The room temperature ^{1}H-NMR spectrum of water free MSA is presented in Figure 5-1.

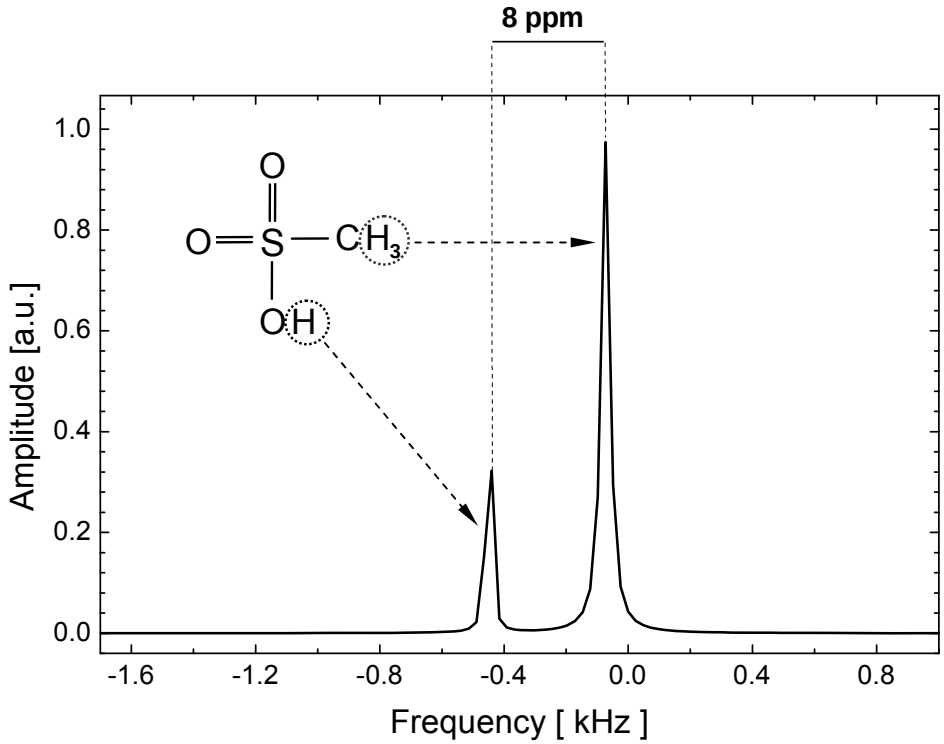

Figure 5-1: *Experimental ^{1}H-NMR spectrum of dry MSA (CH_3SO_3H), at T = 300 K and 49.8 MHz NMR resonance frequency. NMR Spectrum shows two peaks according to the two different proton environments.*

The ratio of the areas under the peaks is used to calculate the ratio of the numbers of protons in the various environments. The areas are in the ratio of 3:1, which is exactly the ratio of three hydrogen atoms in the MSA methyl group to the single hydrogen atoms which is attached to oxygen. The ratio of the areas can be used to find the water content in the acid according to Equation (5-1).

$$\frac{I_{\mathrm{OH}}}{I_{\mathrm{CH}}} = \frac{2x+1}{3} \qquad (5-1)$$

where x is the ratio of initial water mole number $n_{\mathrm{H_2O}}$ to the initial MSA mole number n_{MSA} ($x = n^{\mathrm{i}}_{\mathrm{H_2O}} / n^{\mathrm{i}}_{\mathrm{MSA}}$).

- **^{1}H-NMR Spectrum of MSA-Water Mixtures**

Water has only one type of proton which gives a single peak in the NMR spectrum with 7.3 ppm chemical shift. As mentioned above, MSA shows two ^{1}H-NMR lines, so the NMR spectrum acquired from MSA-water mixtures might be expected to show three lines. But, only two lines are shown in ^{1}H-NMR spectrum, which is due to the fast exchange between the protons in water and H in OH groups of MSA. Because of the fast exchange between the protons, NMR cannot detect them as two different protons and only the average of H_{OH} signals are obtained. Figure 5-2 shows the room temperature NMR spectra of dry MSA, pure water, and the arbitrary chosen mixture MSA•$(H_2O)_3$ as an example. The intensity and the chemical shift of the averaged H_{OH} NMR line are the average of the intensities and the chemical shifts of the initial species in the MSA-water mixture. Several NMR spectra have been obtained for different MSA-water mixtures using 49.8 MHz NMR spectroscopy over the temperature range from 300-370 K. Low resolution ^{1}H-NMR line-widths are in the range of 35-40 Hz, while the line-widths from high resolution NMR spectra of the same mixtures are in the range 3-5 Hz. The reason behind this difference is due to the magnet inhomogeneity in the low resolution NMR, which limits the resolution. As a consequence, the line width of the low resolution NMR spectra shows no temperature dependence above 300 K. Furthermore, the line-widths obtained from high resolution NMR spectra indicates that the system is already in the motional averaging regime.

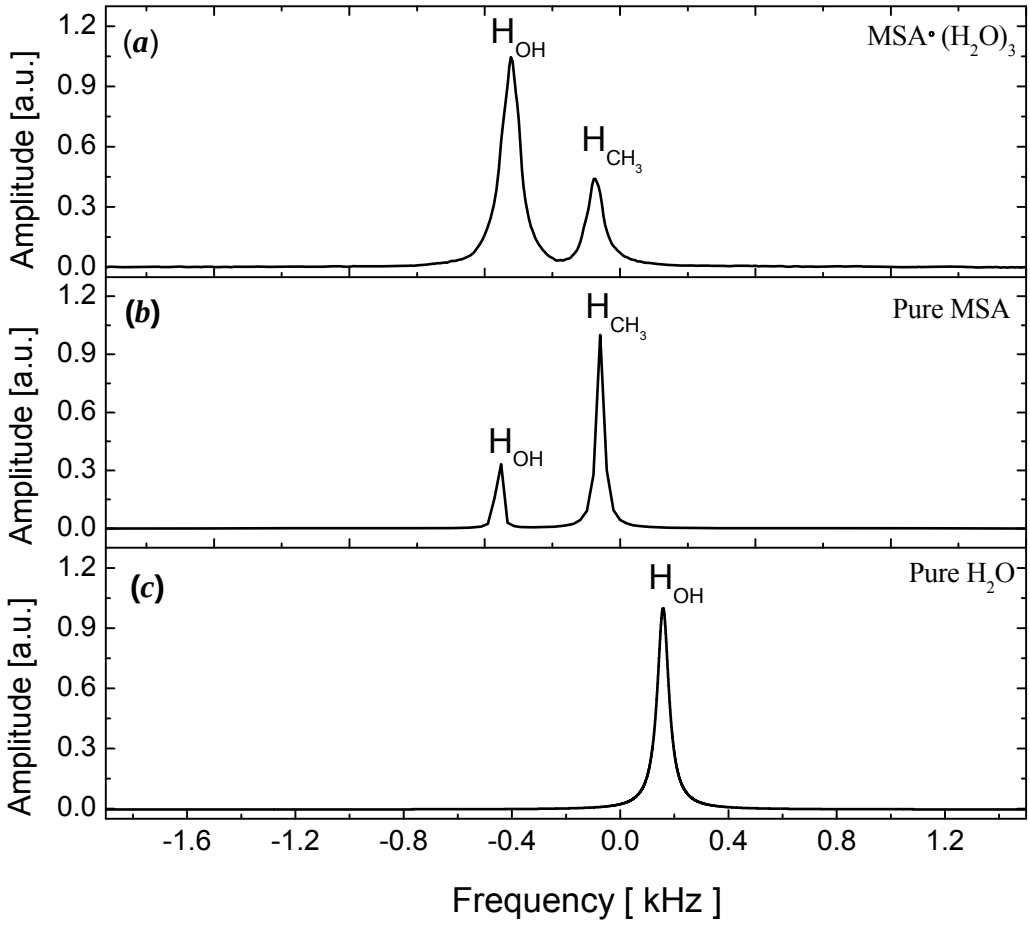

***Figure 5-2**: Experimental ^{1}H-NMR spectra of **(a)** MSA•$(H_2O)_3$ **(b)** dry MSA **(c)** and pure water, at T = 300 K and 49.8 MHz NMR resonance frequency. NMR Spectra of dry MSA and MSA-Water mixture show two peaks according to the two different hydrogen atoms environments.*

5.1.2 MSA Dissociation and Formation of the Protonic Charge Carriers $H^+(H_2O)_n$

MSA is a strong acid[92,93] which is almost completely ionized at 0.1 M in aqueous solution.[92] MSA dissociation in water can be written as follows:

$$CH_3SO_3H + H_2O \rightleftharpoons CH_3SO_3^- + H_3O^+ \qquad (5-2)$$

According to the literature, the values of the MSA acidity constant (pK_a) are around -1.8 in a highly diluted system.[94]

In this thesis, the MSA dissociation constants (K_c) at low water content (high MSA concentration) are required, and in particular, we are interested to obtain MSA dissociation constant as a function of water content in MSA-water system.

A study of the equilibrium in acid-water systems as a function of the water content (stoichiometry) is of interest from the point of view of ascertaining the mechanism of protonic charge carriers formation of aqueous solutions of strong acids.[95,96,97] MSA is classified as a strong monobasic acid, which makes it convenient to study the protonic charge carriers formation as a model to understand the charge formations and transport mechanisms in sulfonated fuel cell membranes.

The degree of dissociation of MSA in water has been determined by IR spectroscopy,[98] Raman spectroscopy,[99] cryoscopy,[100] and conductometry,[101] these studies have not characteristically determined MSA dissociation constant in water as a function of water content. Those studies depend on the optical densities of the chemical bonds absorption bands which are not always unique and precise. However these previous studies supported us with valuable data about the approximate concentration of the dissociated species in MSA-water system.

High resolution NMR chemical shift technique is a unique method to quantitatively determine the concentration of the MSA-water dissociation species for any water content. Not only the concentrations were obtained but the protonic charge carriers transport mechanism type has been determined from the high resolution chemical shift data, self diffusion data and the electrical conductivity data, which are connected to each other via the Nernst-Einstein relation.

- **Protonic Charge Carriers Concentration in MSA-Water System using High Resolution NMR Chemical Shift**

The chemical shifts of H_{OH} and H_{CH_3} in MSA-water aqueous medium are sensitive to the chemical environment of Oxygen and Carbon nuclei. Therefore this experiment is a convenient technique to map the chemical

environmental change due to the water content change and the created protonic charge.

High resolution ^{1}H-NMR spectra of different water content samples of MSA-water systems are presented in Figure 5-3.

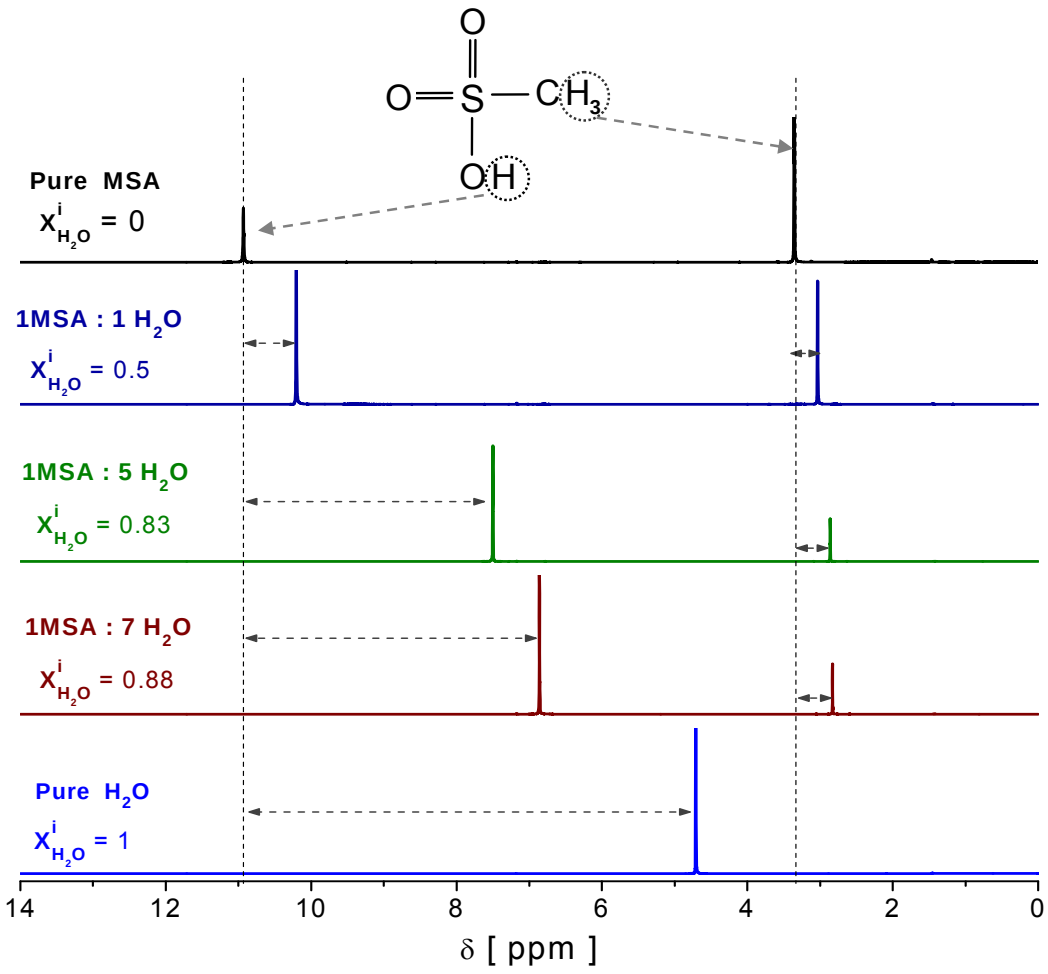

Figure 5-3: *High resolution ^{1}H-NMR spectra at 300 MHz of different MSA-water samples with different water content at room temperature.*

H_{CH_3} chemical shift values decrease monotonously with increasing water content, while the H_{OH} chemical shifts pass through a maximum. The absolute change of H_{OH} chemical shift values is much more obvious than the change in H_{CH_3}. ^{1}H-NMR spectrum of H_{OH} is the average spectrum of ^{1}H in water, hydronium ion and MSA spectra. While H_{CH_3} spectrum is the average of ^{1}H signal of MSA and MSA-anion methyl-groups.

H_{OH} chemical shift in pure MSA is around 11 ppm, and it is around 4.7 ppm in pure water at the same NMR resonance frequency and the measurement conditions.

H_{OH} chemical shift of MSA-water samples are plotted as a function of the water content (Figure 5-4).

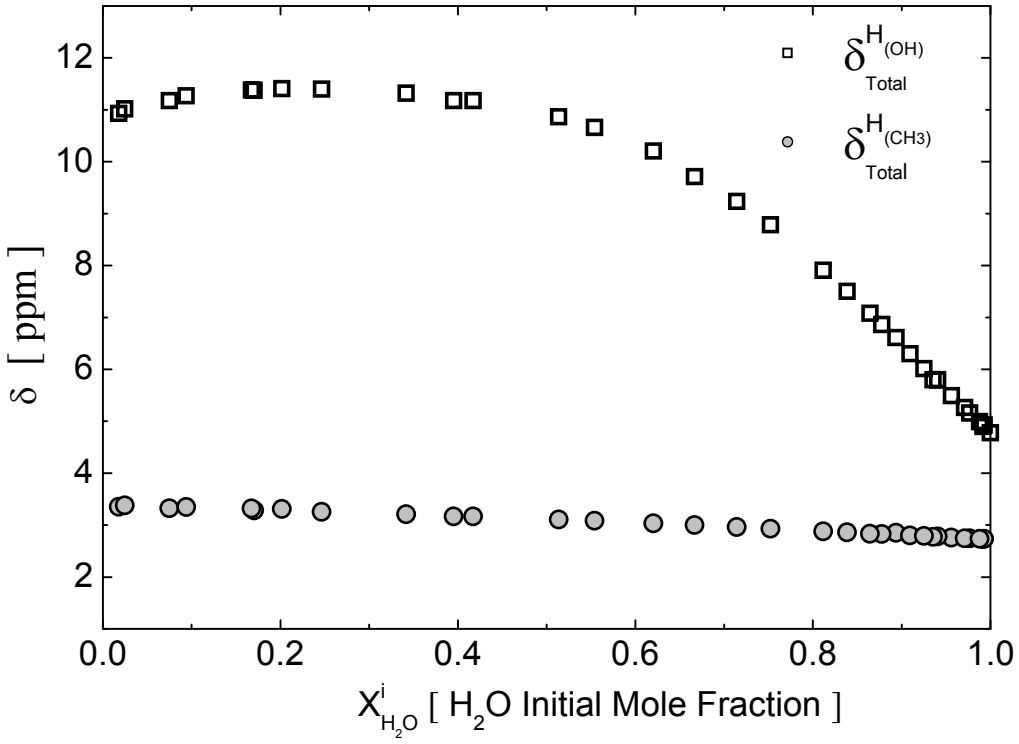

Figure 5-4: *^{1}H-NMR high resolution chemical shift of H_{OH} and H_{CH_3} of MSA-water samples as a function of initial water mole fraction. The measurements have been performed at 300 MHz NMR resonance frequency and at room temperature. $CDCl_3$ is used as a frequency lock in these high resolution NMR measurements.*

The ^{1}H chemical shifts actually pass through maxima, which appear to be the consequence of two effects changing the chemical shift in opposite directions: at very low water content, H_3O^+ ions form progressively with increasing water content, while further addition of water simply leads to the dilution of hydronium ions, the species with the highest ^{1}H chemical shift.

This issue has previously been studied by density functional theory and ab-initio calculations of the MSA-$(H_2O)_n$, n=1-5. The clusters up to three water molecules are dominated by strong hydrogen bond interactions.[102,103] With a minimum of four water molecules, MSA is dissociated as a result of proton transfer from MSA to water.[102] The reason above illustrates the molecular clusters network arrangement existence associated with the entire active hydrogen network in the solution beside the stabilization energies of the MSA-water.[104] Accordingly MSA-water aqueous environment does not depend linearly on water content.

The relation between the chemical shifts and the change of the water content concentration can be used to obtain the species stoichiometries after equilibrium, and consequently MSA dissociation constant for any water content. This approach needs some assumptions to simplify the numerical calculations which are summarized as follows.

- The chemical shifts of H_{OH} in water, hydronium Ion, and MSA are assumed to be constant over the whole water content range.
- Hydronium ions are assumed to be the dominant protonic charge carriers.
- Any excess volume of the MSA-water mixtures is ignored; this is actually smaller than 3% and the effect of this approximation will be discussed later in this chapter.

With these assumptions, the total chemical shift is written as:

$$\delta^{H_{OH}}_{Total} = 3X_{H_3O^+}\,\delta_{H_3O^+} + 2X_{H_2O}\,\delta_{H_2O} + X_{CH_3SO_3H}\,\delta_{CH_3SO_3H} \qquad (5-3)$$

where X are mole fractions and δ chemical shifts.

Further equations are the expressions for the dissociation constat K_C :

$$K_C = \frac{C_{CH_3SO_3^-}\,C_{H_3O^+}}{C_{CH_3SO_3H}\,C_{H_2O}} \qquad (5-4)$$

and the electroneutrality condition: ($C_{CH_3SO_3^-} = C_{H_3O^+}$).

Let us denote the initial concentration of MSA and water as ($C^{i}_{CH_3SO_3H}$, $C^{i}_{H_2O}$) respectively. The initial species dissociate according to Equation (5-2) and equilibrate according to Equation (5-4). Therefore the connection between the initial species and the dissociated ones can be written as follows.

$$\begin{aligned} C^{i}_{CH_3SO_3H} &= C_{CH_3SO_3H} + C_{CH_3SO_3^-} \\ C^{i}_{H_2O} &= C_{H_2O} + C_{H_3O^+} \end{aligned} \qquad (5-5)$$

By substituting Equations (5-5) into Equation (5-4), MSA dissociation constant is obtained in terms of initial species concentration and the hydronium ion concentration at the equilibrium state. Then MSA dissociation constant can be written as

$$K_C = \frac{C^2_{H_3O^+}}{\left(C^{i}_{CH_3SO_3H} - C_{H_3O^+}\right)\left(C^{i}_{H_2O} - C_{H_3O^+}\right)} \qquad (5-6)$$

From Equation (5-6), the hydronium ion concentration $C_{H_3O^+}$ can be written

$$C_{H_3O^+} = \frac{\sqrt{\left(C^{i}_{CH_3SO_3H} + C^{i}_{H_2O}\right)^2 - 4\left(\frac{1}{K_C} - 1\right)C^{i}_{CH_3SO_3H}C^{i}_{H_2O}} - \left(C^{i}_{CH_3SO_3H} + C^{i}_{H_2O}\right)}{2\left(\frac{1}{K_C} - 1\right)} \qquad (5-7)$$

The initial mole fraction of the starting species (water and MSA) can be expressed as

$$\begin{aligned} x^{i}_{H_2O} &= \frac{n^{i}_{H_2O}}{n^{i}_{H_2O} + n^{i}_{CH_3SO_3H}} \\ x^{i}_{CH_3SO_3H} &= \frac{n^{i}_{CH_3SO_3H}}{n^{i}_{H_2O} + n^{i}_{CH_3SO_3H}} \end{aligned} \qquad (5-8)$$

In the literature, the water content is frequently expressed as $\lambda = \frac{n^{i}_{H_2O}}{n^{i}_{SO_3H}}$, with this quantity, $x^{i}_{H_2O}$ may be calculated according to $x^{i}_{H_2O} = \lambda\,(1+\lambda)^{-1}$.

After equilibrating, the species mole fractions are different and can be written as

$$
\begin{aligned}
x_{H_2O} &= \frac{n_{H_2O}}{n_{H_2O} + n_{CH_3SO_3H} + n_{H_3O^+} + n_{CH_3SO_3^-}} \\
x_{H_3O^+} &= \frac{n_{H_3O^+}}{n_{H_2O} + n_{CH_3SO_3H} + n_{H_3O^+} + n_{CH_3SO_3^-}} \\
x_{CH_3SO_3H} &= \frac{n_{CH_3SO_3H}}{n_{H_2O} + n_{CH_3SO_3H} + n_{H_3O^+} + n_{CH_3SO_3^-}}
\end{aligned}
\qquad (5-9)
$$

Since the mole number of water at equilibrium is equal to the initial mole number of water minus the hydronium ion mole number, (the same is true for MSA), we can write the following equations:

$$
\begin{aligned}
n_{H_2O} &= n^i_{H_2O} - n_{H_3O^+} \\
n_{CH_3SO_3H} &= n^i_{CH_3SO_3H} - n_{H_3O^+}
\end{aligned}
\qquad (5-10)
$$

As we have considered earlier that $x = n_{H_2O} / n_{MSA}$ along with Equation $(5-7)$, then hydronium ion mole number after equilibrium for any initial water content can be written as:

$$
n_{H_3O^+} = \frac{\sqrt{(1+x)^2 - 4\left(\frac{1}{K_c} - 1\right)x} - (1+x)}{2\left(\frac{1}{K_c} - 1\right)}
\qquad (5-11)
$$

As we have anticipated earlier, the difference between the summation of the volumes (ideal volume) of the added species and the volume after equilibrium due to the internal interactions is small but exists. Both, equilibrium volume and the ideal volume are plotted as a function of initial water mole fraction in Figure 5-5. The maximum reduction in volume is around 0.06 of the ideal volume.

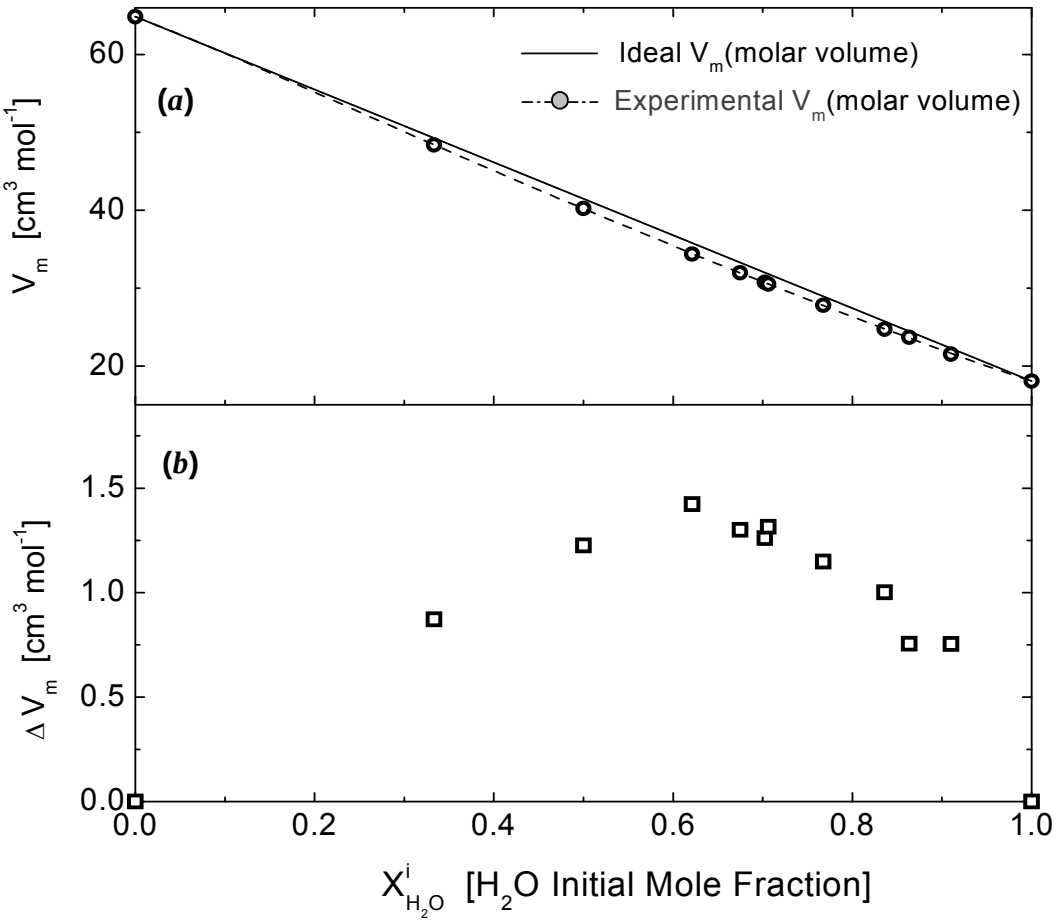

Figure 5-5: (a) *Ideal and experimental molar volumes of MSA-water mixtures as a function of water content.* ***(b)*** *The absolute difference between the experimental and the theoretical molar volumes versus initial water mole fraction content in the same mixtures.*

The ideal volume of MSA-water mixtures can be calculated from the added mole numbers, the molecular weights (M_{H_2O}, $M_{CH_3SO_3H}$) and the individual densities as in Equation (5-12)

$$V \cong V^i_{H_2O} + V^i_{CH_3SO_3H}$$

$$V = \frac{n^i_{H_2O} M_{H_2O}}{\rho_{H_2O}} + \frac{n^i_{CH_3SO_3H} M_{CH_3SO_3H}}{\rho_{CH_3SO_3H}} \qquad (5-12)$$

In a highly diluted system and in the case of strong acid like MSA, acid molecules dissociate almost completely.[105,106] The concentration of the

undissociated form of the acid, which does not enter into the composition of stable complexes (the so-called "free" CH_3SO_3H molecules) is not observed at acid concentrations below 30 mole%.[107,108] Therefore, the chemical shift at high water contents is anticipated to be independent of the water content:

$$\delta^{H_{OH}}_{Total} = 3x_{H_3O^+}\ \delta_{H_3O^+} + 2x_{H_2O}\ \delta_{H_2O} \qquad (5-13)$$

and, therefore this regime allows for a good estimation of the H_3O^+ chemical shift.

For high diluted MSA-water system, the following relations are valid and can be used to solve Equation (5-15).

$$\left.\begin{aligned} n_{CH_3SO_3^-} &= n_{H_3O^+} \\ n_{CH_3SO_3^-} &= n^i_{CH_3SO_3H} \\ n_{H_3O^+} &= n^i_{CH_3SO_3H} \end{aligned}\right\} \textit{total dissociation} \qquad (5-14)$$

Finally, equations ((5-7), (5-13) and (5-14)) can be solved simultaneously for the highly diluted experimental points, these points and the results are shown in Table 5-1.

$n^i_{H_2O}$	$n^i_{CH_3SO_3H}$	$H_2O^i_{MoleFraction}$	$H_2O^i_{MoleFraction}$	$x^H_{H_2O}$	$x^H_{H_3O^+}$	$\delta_{H_{OH}}$	$\delta_{H_3O^+}$
Mole	Mole	Mole/Liter	Mole/Liter	$Mole_H$ /Liter	$Mole_H$ /Liter	ppm	ppm
7.2	1	0.878	0.122	0.805	0.196	6.86	15.43
8.4	1	0.894	0.106	0.831	0.171	6.61	15.38
10.0	1	0.909	0.091	0.858	0.147	6.30	14.96
12.3	1	0.925	0.075	0.883	0.123	6.01	14.59
14.5	1	0.935	0.065	0.900	0.106	5.80	14.10
15.8	1	0.941	0.059	0.908	0.098	5.80	14.87
21.7	1	0.956	0.044	0.932	0.073	5.50	14.15
33.6	1	0.971	0.029	0.956	0.049	5.27	14.35
41.6	1	0.977	0.023	0.964	0.040	5.16	13.92
80.6	1	0.988	0.012	0.982	0.021	4.99	14.45
117.6	1	0.992	0.008	0.987	0.014	4.95	15.98
141.0	1	0.993	0.007	0.989	0.012	4.93	16.42

Table 5-1: *Numerical data of the calculated ^{1}H-NMR chemical shift of H_3O^+ at high diluted system of MSA-water. The table shows numerical data of H_3O^+ mole fraction as well.*

For the limiting case of highly diluted solutions the analytically obtained chemical shift of ^{1}H in H_3O^+ is almost constant with a mean value of 14.89 ppm.

In the general case, i.e. for any water content, Equation (5-3) is solved for the equilibrium condition by using Maple software. For this, the ^{1}H-NMR chemical shift of H_3O^+ was taken as $\delta_{H_3O^+}$ = 14.89 ppm (see above) and the experimentally determined H_{OH} chemical shift of water δ_{H_2O} and MSA δ_{MSA} (10.85 and 4.78 ppm) were used.

The results are presented in Table 5-2 and illustrated in Figure 5-6, in which the species mole fraction are plotted as a function of the initial water mole fraction.

$n^i_{H_2O}$ Mole	$n^i_{CH_3SO_3H}$ Mole	$X^i_{H_2O}$ Mole fraction	$X^i_{CH_3SO_3}$ Mole fraction	X_{H_2O} Mole fraction	$X_{CH_3SO_3H}$ Mole fraction	$X_{H_3O^+}$ Mole fraction	$\delta^{Calculated}_{H_{CH}}$ ppm	$\delta^{Measured}_{H_{CH}}$ ppm	K_C
0.02	1	0.018	0.982	0.007	0.97094	0.011	10.94	10.93	0.02
0.08	1	0.075	0.925	0.029	0.87892	0.046	11.18	11.19	0.09
0.21	1	0.171	0.829	0.073	0.73164	0.098	11.36	11.37	0.18
0.33	1	0.246	0.754	0.110	0.61744	0.136	11.42	11.40	0.27
0.52	1	0.342	0.658	0.167	0.48334	0.175	11.31	11.32	0.38
0.72	1	0.417	0.583	0.215	0.38056	0.202	11.16	11.17	0.50
1.06	1	0.514	0.486	0.284	0.25695	0.229	10.86	10.86	0.72
1.24	1	0.554	0.446	0.318	0.21037	0.236	10.65	10.66	0.83
1.63	1	0.620	0.380	0.380	0.13997	0.240	10.23	10.20	1.08
1.97	1	0.663	0.337	0.431	0.10426	0.232	9.81	9.82	1.20
2.08	1	0.675	0.325	0.445	0.09505	0.230	9.70	9.71	1.25
2.54	1	0.717	0.283	0.498	0.06356	0.219	9.26	9.24	1.52
3.03	1	0.752	0.248	0.550	0.04547	0.202	8.78	8.78	1.64
4.31	1	0.812	0.188	0.647	0.02356	0.165	7.89	7.91	1.78
5.19	1	0.838	0.162	0.692	0.01548	0.146	7.48	7.50	1.99
6.37	1	0.864	0.136	0.739	0.00990	0.126	7.06	7.08	2.16
7.17	1	0.878	0.122	0.763	0.00782	0.115	6.84	6.86	2.20
8.40	1	0.894	0.106	0.793	0.00590	0.101	6.57	6.61	2.16
15.82	1	0.941	0.059	0.883	0.00192	0.058	5.77	5.80	1.95
21.69	1	0.956	0.044	0.913	0.00104	0.043	5.52	5.50	1.95
33.59	1	0.971	0.029	0.943	0.00046	0.028	5.26	5.27	1.85
41.63	1	0.977	0.023	0.953	0.00031	0.023	5.17	5.16	1.80
80.58	1	0.988	0.012	0.976	0.00008	0.012	4.98	4.99	1.80
117.61	1	0.992	0.008	0.983	0.00004	0.008	4.92	4.90	1.80
141.01	1	0.993	0.007	0.986	0.00003	0.007	4.90	4.92	1.80

Table 5-2: *Numerical data of the calculated K_c as a result of fitting the experimental chemical shift of H_{OH} over the water mole fraction content range at room temperature. The table shows also the numerical data of water, MSA, MSA anion and hydronium ion. Initial mole number of water and MSA are also presented.*

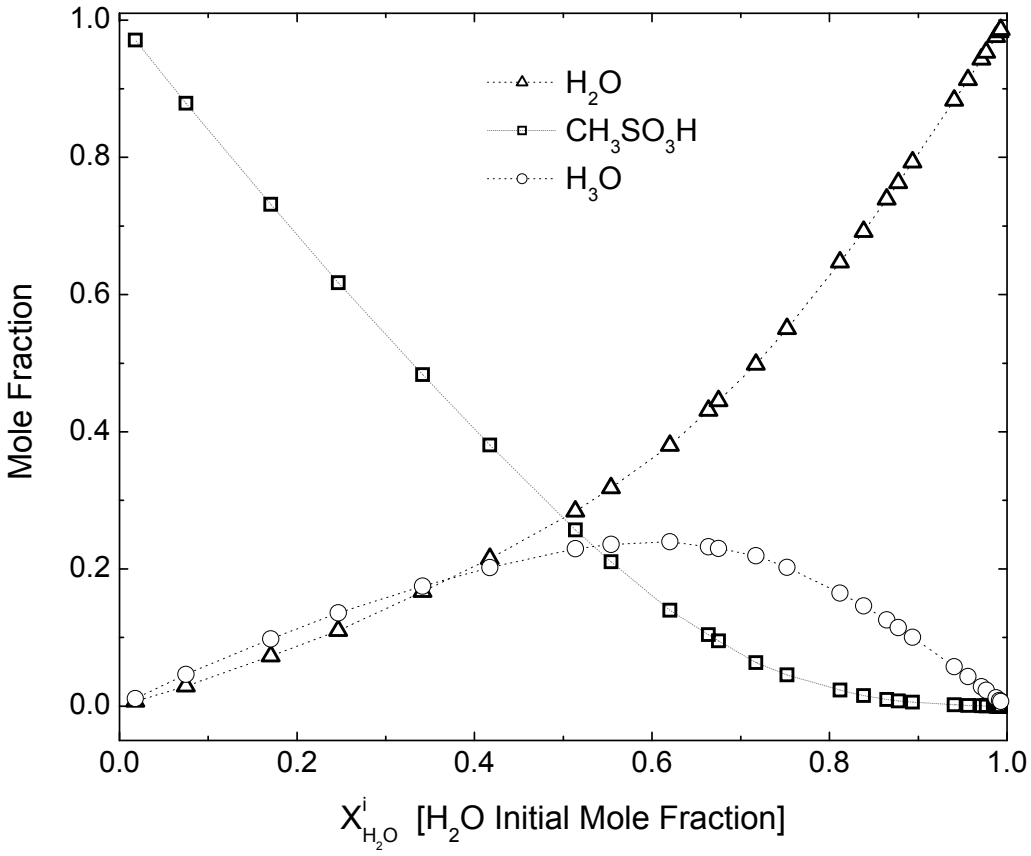

Figure 5-6: *The solution species (H_3O^+, H_2O, and CH_3SO_3H) mole fraction versus the initial water mole fraction. The H_3O^+ mole fraction shows peak at around 0.65 water mole fraction.*

MSA dissociation constant K_c as a function of the water content can be calculated from Equation (5-6) using the species concentrations given in Table 5-2. The results are shown in Figure 5-7.

Experimentally, the reduction in volume after equilibrium is not more than 0.033% of the ideal volume in the highly diluted regime (see Table 5-2 and Figure 5-5).

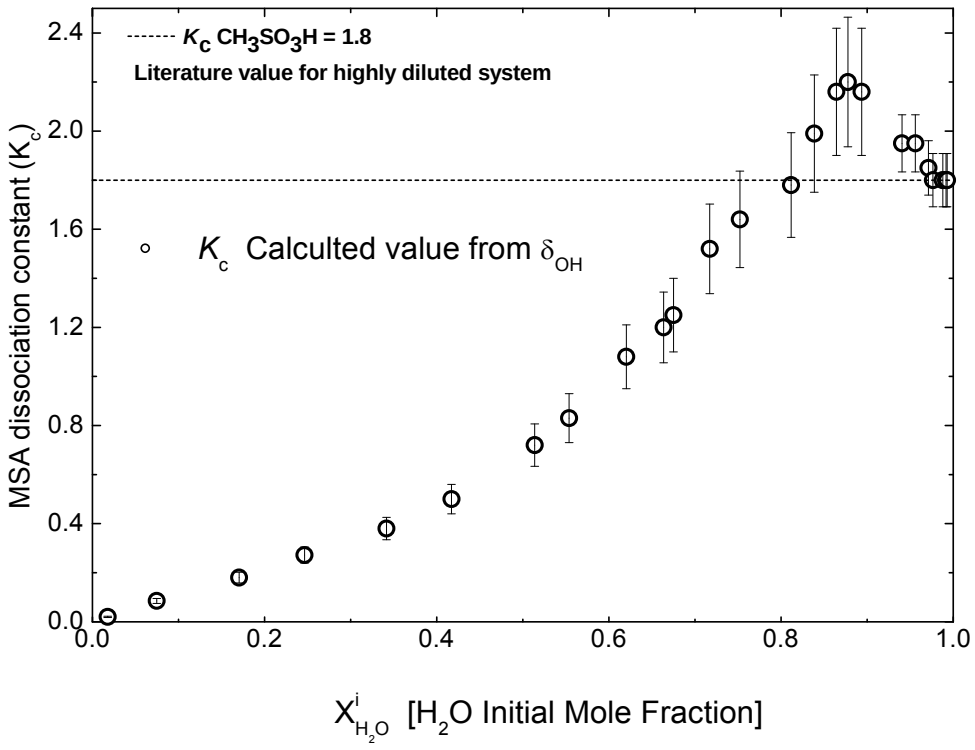

Figure 5-7: *MSA dissociation constant in water as a function of initial water mole fraction, calculations based on the experimental values of H_{OH} high resolution NMR of MSA-water mixture samples, some equations have been derived from the boundary condition of the mixtures equilibrium beside some assumptions. MSA dissociation constant K_c literature values are around 1.8.* [109]

In the earlier calculations, we obtained K_C of MSA from H_{OH} chemical shift changes. In principle one can follow the same method to obtain K_C of MSA from H_{CH_3} chemical shift changes. In order to test the consistency of the obtained K_C values with the H_{CH_3} chemical shift changes, the latter have been calculated from K_C and compared to the experimental data.

The theoretical background of H_{CH_3} chemical shift calculations are similar to H_{OH} chemical shift calculations, which are discussed sufficiently, so we are not going to derive the general equations as we have done in the first part.

Because of the rapid proton exchange, there is only one ^{1}H-NMR line of H_{CH_3} of MSA and MSA anions according to Equation (5-15)

$$\delta^{H_{CH_3}}_{Total} = x^H_{CH_3SO_3H}\ \delta_{CH_3SO_3H} + x^H_{CH_3SO_3^-}\ \delta_{CH_3SO_3^-} \qquad (5-15)$$

MSA and MSA anion proton mole fraction can be written as in Equation (5-16)

$$x^{H_{CH_3}}_{CH_3SO_3H} = \frac{n_{CH_3SO_3H}}{3n_{CH_3SO_3^-} + 3n_{CH_3SO_3H}} = \frac{n^i_{CH_3SO_3H} - n_{H_3O^+}}{n^i_{CH_3SO_3H}}$$

$$x^{H_{CH_3}}_{CH_3SO_3^-} = \frac{3n_{CH_3SO_3^-}}{3n_{CH_3SO_3H} + 3n_{CH_3SO_3^-}} = \frac{n_{H_3O^+}}{n^i_{CH_3SO_3H}} \qquad (5-16)$$

The experimentally obtained values of ^{1}H-NMR chemical shifts of MSA and MSA anions (3.352 and 2.7354 ppm) have been used in solving Equation (5-16). The numerical results of the solved relation are presented in the Table 5-3.

The last two columns in Table 5-3 summarize the experimental and the calculated averaged ^{1}H-NMR chemical shifts of the methyl group protons in MSA and MSA-anions, and they are also plotted in Figure 5-8.

$n^{i}_{H_2O}$ Mole	$n^{i}_{CH_3SO_3H}$ Mole	$X^{i}_{H_2O}$ Mole fraction	$X^{H_{CH_3}}_{CH_3SO_3^-}$ Mole fraction	$X^{H_{CH_3}}_{CH_3SO_3H}$ Mole fraction	K_C Dimensionless	$\delta^{Calculated}_{H_{CH_3}}$ ppm	$\delta^{Measured}_{H_{CH_3}}$ ppm
0.02	1	0.0178	0.033201	0.953960	0.020	3.345	3.352
0.08	1	0.0748	0.129042	0.817719	0.085	3.321	3.325
0.21	1	0.1705	0.250755	0.625052	0.180	3.279	3.286
0.33	1	0.2464	0.327617	0.495360	0.272	3.241	3.255
0.52	1	0.3417	0.391255	0.360249	0.380	3.188	3.209
0.72	1	0.4172	0.428117	0.268529	0.500	3.138	3.169
1.06	1	0.5137	0.454559	0.169747	0.720	3.061	3.110
1.24	1	0.5539	0.455066	0.135377	0.830	3.026	3.084
1.63	1	0.6202	0.444026	0.086391	1.080	2.963	3.034
1.97	1	0.6635	0.418880	0.062673	1.200	2.926	3.000
2.08	1	0.6750	0.411856	0.056748	1.250	2.916	2.999
2.54	1	0.7171	0.383153	0.037016	1.520	2.874	2.964
3.03	1	0.7521	0.346645	0.025952	1.640	2.848	2.932
4.31	1	0.8117	0.272780	0.013007	1.780	2.813	2.879
5.19	1	0.8385	0.238336	0.008421	1.990	2.794	2.863
6.37	1	0.8644	0.202265	0.005312	2.160	2.780	2.834
7.17	1	0.8776	0.183013	0.004162	2.200	2.775	2.830
8.40	1	0.8936	0.159255	0.003115	2.160	2.770	2.854
15.82	1	0.9406	0.088929	0.000990	1.950	2.755	2.782
21.69	1	0.9559	0.066004	0.000532	1.950	2.750	2.760
33.59	1	0.9711	0.043294	0.000235	1.850	2.745	2.746
41.63	1	0.9765	0.035126	0.000158	1.800	2.744	2.746
80.58	1	0.9877	0.018373	0.000042	1.800	2.740	2.735
117.61	1	0.9916	0.012640	0.000020	1.800	2.738	2.733
141.01	1	0.9930	0.010558	0.000014	1.800	2.738	2.735

Table 5-3*: The $\delta^{Measured}_{H_{CH_3}}$ along with the numerical calculated $\delta^{Calculated}_{H_{CH_3}}$ values, which are derived from the K_c which is originally calculated from the $\delta^{Expermental}_{H_{OH}}$ of the model system.*

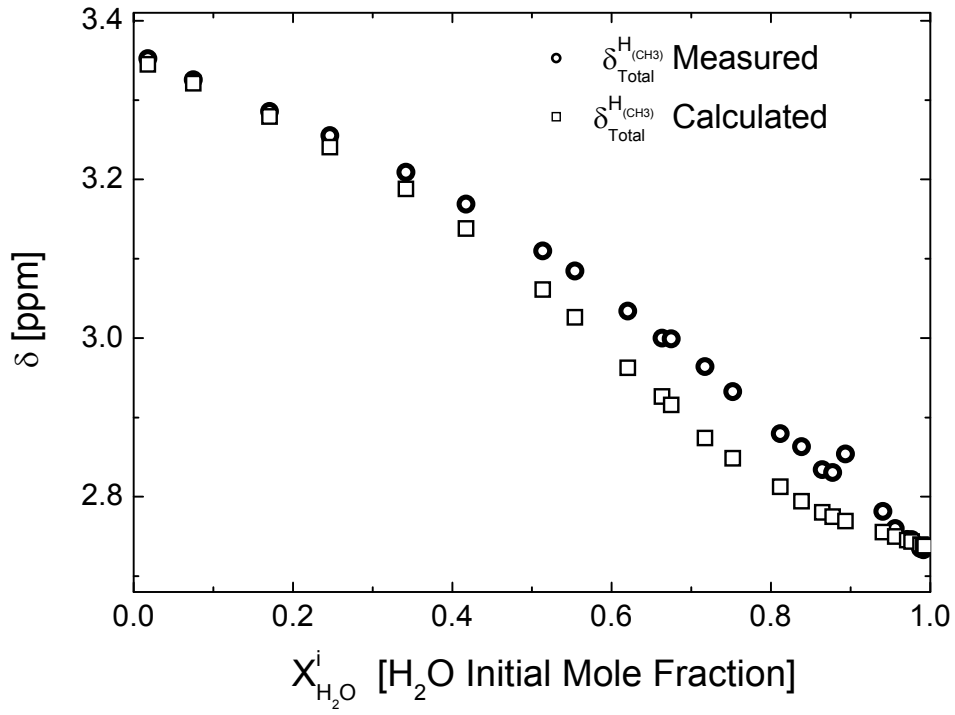

Figure 5-8: *The experimental and the calculated chemical shifts of H_{CH_3} ($\delta^{H_{CH_3}}_{Total}$) in the MSA-water binary system, the calculated $\delta^{H_{CH_3}}_{Total}$ derived from the calculated K_c from ^1H Chemical shift in OH group ($\delta^{H_{OH}}_{Total}$) of the species.*

The calculated $\delta^{H_{CH_3}}_{Total}$ is in a very good agreement with the measured values, which is a strong evidence that the derived K_c from $\delta^{H_{CH_3}}_{Total}$ is reasonable. The small deviation of the calculated from the measured $\delta^{H_{CH_3}}_{Total}$ ranging between 0.5 and 0.9 initial water mole fraction falls within the expected experimental deviation, and is mainly related to the used assumptions. In spite of the small effect of the reduction in volume which was assumed to be ideal in the calculation, the deviation in calculated $\delta^{H_{CH_3}}_{Total}$ follows the small reduction in volumes, this relation is illustrated in Figure 5-9 (a and b), both curves have the same trend over the initial water content which is strong indication that the deviation between the experimental and the calculate values are mainly driven by the deviation between the experimental and the ideal volumes of MSA-water mixtures. The effect of other factors like the non linearity of protonic charge carriers concentration distribution, the created molecular

clusters due to the H-bond network is not excluded and contributes in this deviation.

Taking into account the effect of volume change after equilibration would make calculated MSA K_c closer to the ideal MSA K_c values.

The effect due to the nonlinearity of protonic charge density and the hydrogen bond networks can be clarified more deeply after discussing the activation energies deduced from the spin lattice relaxation rate Γ_1 (short-range), NMR self diffusion (long-range), and electrical conductivity measurements.

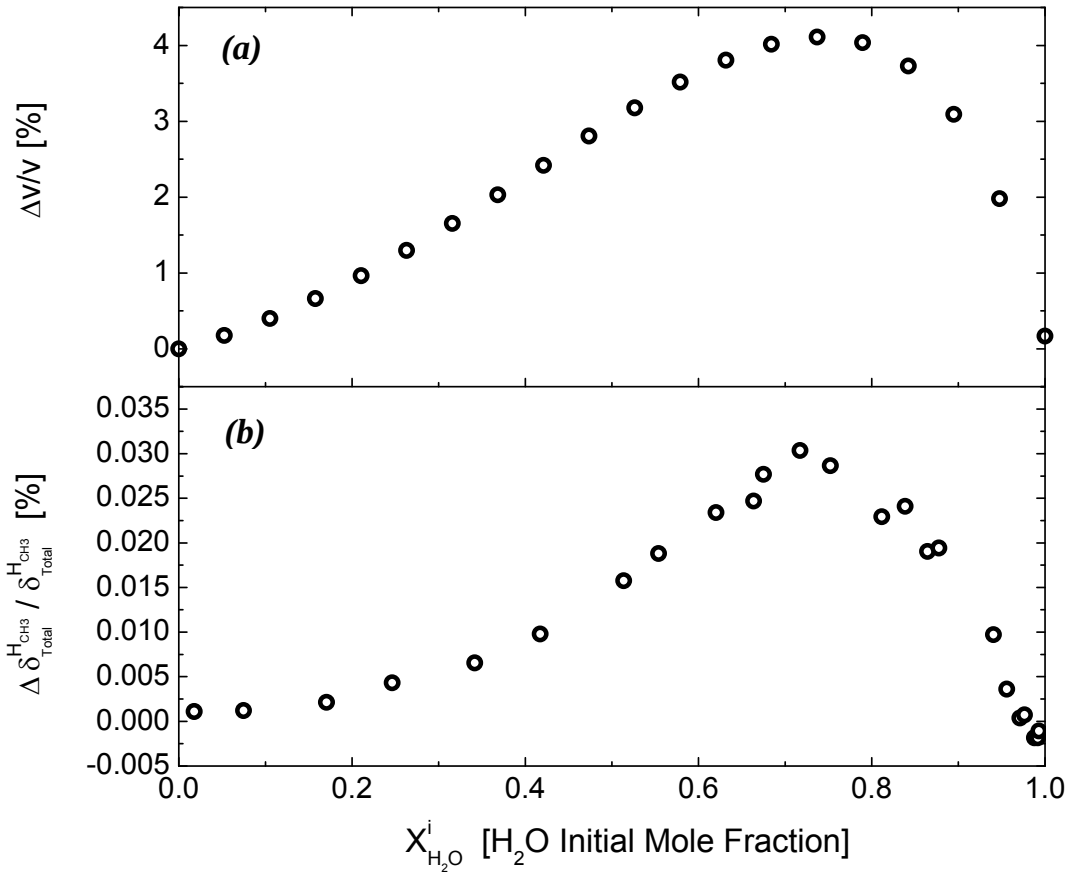

Figure 5-9: (a) *The relative difference between the experimental and ideal volumes of MSA-water mixtures versus the initial water mole fraction at room temperature* ***(b)*** *The relative difference between the experimental and the calculated chemical shift of H_{CH_3} for the same samples.*

5.1.3 Proton Diffusion

- **Spin lattice relaxation rate and the activation energies in MSA-water system**

Spin lattice relaxation times are very sensitive to changes in the molecular environment and the molecular mobility. The protonic relaxation provides important information about the medium.[110,111]

Therefore, spin lattice relaxation rate measurements have been performed in MSA-water samples with different water content between 290 and 350 K in order to gain information about the local proton dynamics. The temperature dependent spin lattice relaxation data of H_{OH} and H_{CH_3} are presented in Figure 5-10.

The difference in the chemical shifts between the protons in OH groups and the protons in CH groups in MSA and MSA-water mixtures allow us to separately investigate Γ_1 for both NMR lines in the NMR spectrum, and to obtain two independent Γ_1 values in every single measurement (see Figure 5-10).

The obtained experimental Γ_1 data cover only the high temperature side of the relaxation maximum. It is not possible to cover the peak and any part of the low temperature side in BPP curve because MSA-water samples freeze in the temperature range T = 290 - 310 K. As a consequence, the experimental Γ_1 data could not be fitted to BPP model, and then the second moment M_2 and the absolute hopping frequency τ_d that contain an important data about the system cannot be obtained. But, the data of Γ_1 is fitted to Arrhenius plot and the activation energy is obtained. The activation energy deduced from Γ_1 data are presented and discussed later in this chapter together with the activation energy deduced from self diffusion data.

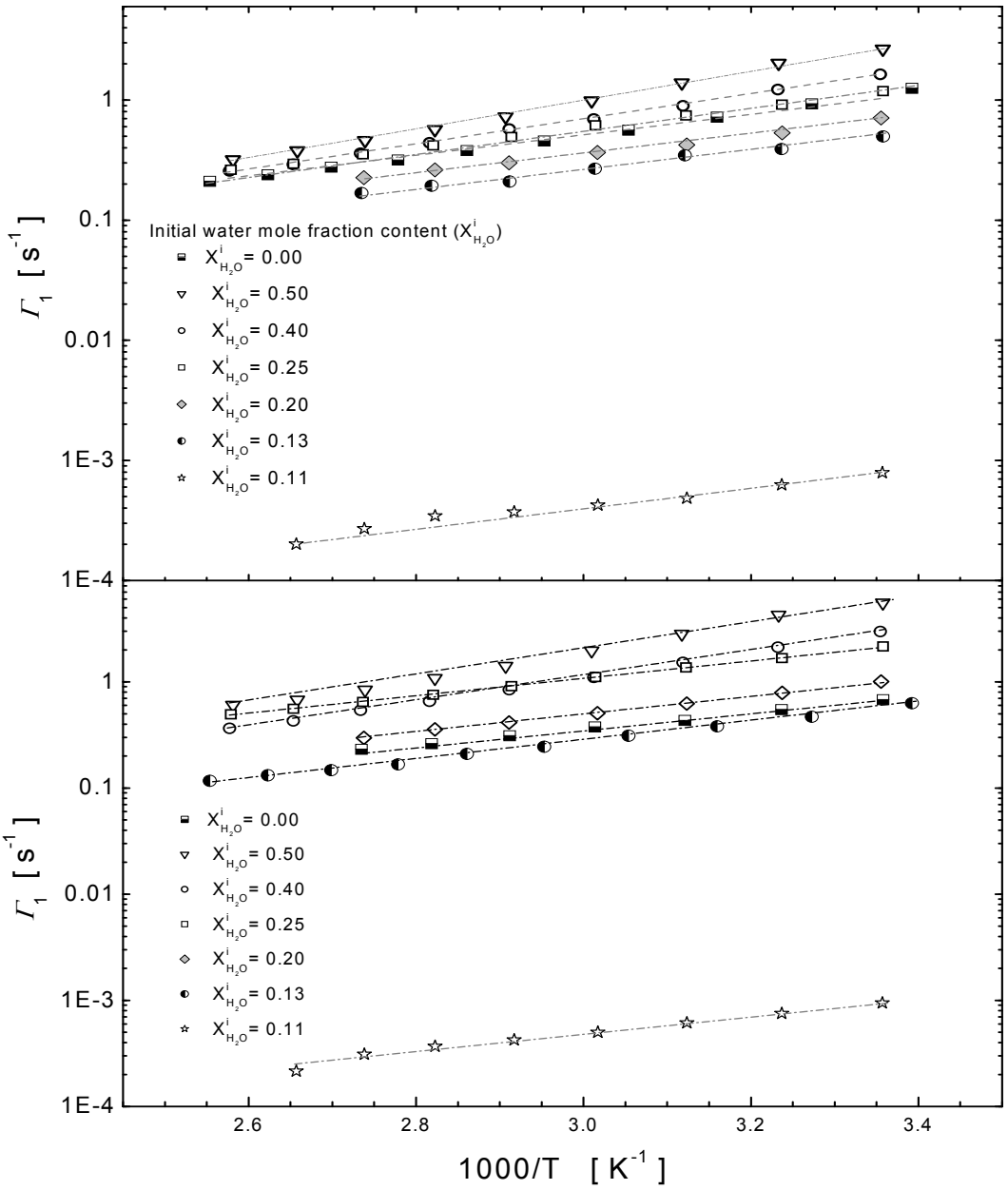

Figure 5-10: *Spin lattice relaxation rate of H_{OH} and H_{CH_3} in MSA-water mixtures. The data are taken at 49.5 MHz NMR resonance frequency. The solid lines are the Arrhenius fit of the data.*

Γ_1 data of H_{OH} and H_{CH_3} have been measured over a wide range of initial water contents at room temperature. The results are presented in Figure 5-11. The Γ_1 curves for both H_{OH} and H_{CH_3} pass through a broad maximum at a water mole fraction of about 0.6, and it is worth mentioning

that this maximum coincides with the maximum of the H_3O^+ concentration (see Figure 5-6) and the minimum of the proton diffusion coefficient (Figure 5-14). This behaviour suggests that i) Γ_1 is controlled by the diffusional behaviour of the system and that ii) the latter is strongly affected by the concentration of charged species, i.e. with increasing concentration of both anions ($MeSO_3^-$) and cations (H_3O^+) the global diffusion coefficient decreases as will be discussed later.

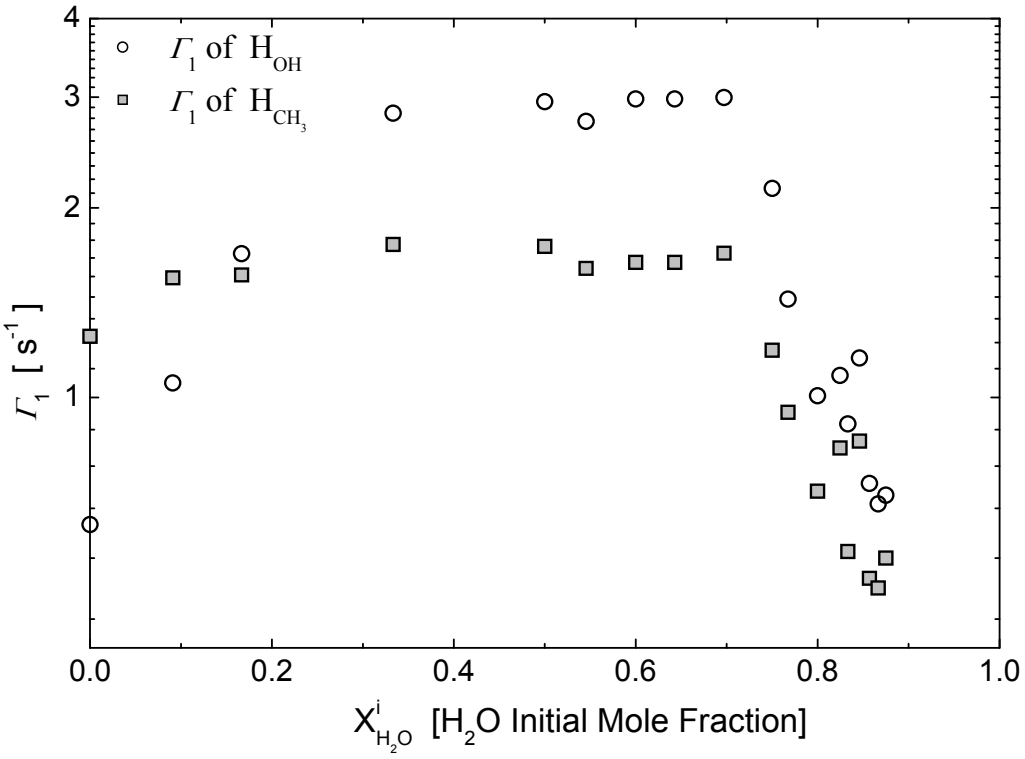

Figure 5-11: *Spin lattice relaxation rate of protons in H_{OH} and H_{CH_3} versus initial water mole fraction at room temperature.*

- **Proton PFG-NMR Self Diffusion (Long Range Diffusion).**

Self-diffusion of protons in water, MSA, and MSA-water mixtures have been measured by PFG-NMR. Diffusion coefficients of H_{OH}, H_{CH_3} have been obtained over the temperature range 300-380 K. The results are shown in the Arrhenius plot in Figure 5-12.

The activation energies derived from temperature dependent self diffusion Arrhenius plots for different initial water content samples are presented in

Figure 5-13. The activation energies obtained from Γ_1 are also shown in the same figure for comparison.

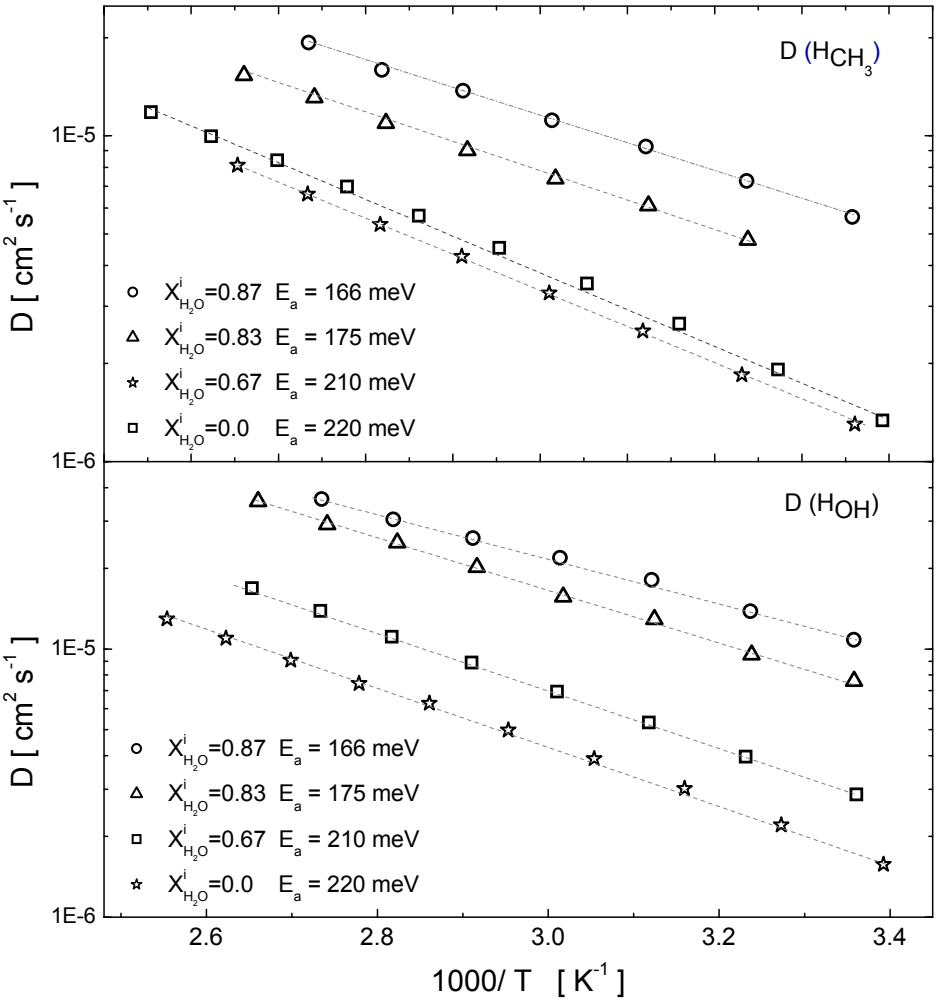

Figure 5-12: *Temperature dependent diffusion data for different water content MSA samples taken by PFG-NMR at 50 MHz. Different lines represent different water mole fractions in the sample. The dotted lines are the fitted Arrhenius plots.*

The activation energies of pure MSA deduced from self-diffusion and spin lattice relaxation data are close to 200 meV. With increasing water content the activation energies pass through broad maxima around 0.6 water mole fraction with values around 250 meV. Beyond these maxima, i.e. with further increasing water content, the activation energies monotonously decrease to

the values for pure water (~ 120 meV for both Γ_1 and the diffusion coefficients).

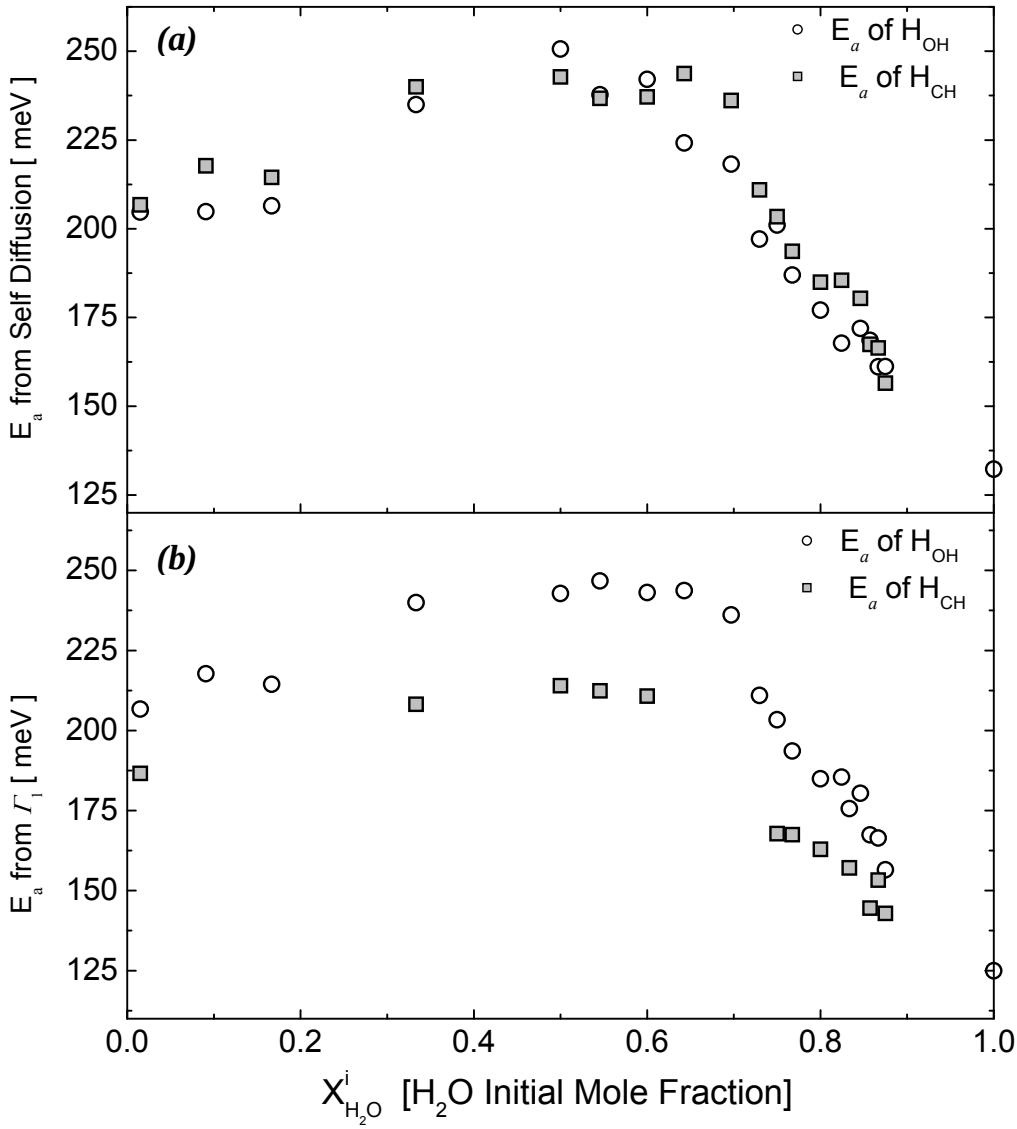

***Figure 5-13**: Activation energies of protons in OH and CH groups versus initial water mole fraction at room temperature. The data are obtained by fitting an Arrhenius law of **(a)** the self diffusion data and **(b)** the spin lattice relaxation data.*

Figure 5-14 shows the room temperature values of $D(H_{CH_3})$ and $D(H_{OH})$. Just as Γ_1 is passing through a maximum, both diffusion coefficients pass through a broad minimum around a water mole fraction of $X^i_{H_2O}=0.6$. At these concentrations the diffusion coefficients are about one order of magnitude

lower than that of pure water (2.2×10^{-5} cm^{-2} s^{-1}) [79] and they are only slightly lower than the diffusion coefficient of pure MSA (approx. 1.5×10^{-6} cm^2 s^{-1}).
The close relationship between the data describing $D(H_{CH_3})$, $D(H_{OH})$ and Γ_1 suggests a cooperative dynamics of all species in the systems (MSA, MSA^-, H_3O^+, H_2O), and that this dynamics is closely related the concentration of charge carriers (anions and cations), as discussed above. It is also anticipated that the viscosity of MSA-H_2O mixtures may follow the same pattern as will be discussed at the end of this chapter.
The question whether or not proton conductivity is related to the same underlying elementary processes, in other words, whether proton conduction is just a simple vehicle mechanism (e.g. diffusion of H_3O^+ and H_2O) or whether it also bears some structure diffusion requires precise data of the ionic conductivity of MSA-H_2O mixtures.

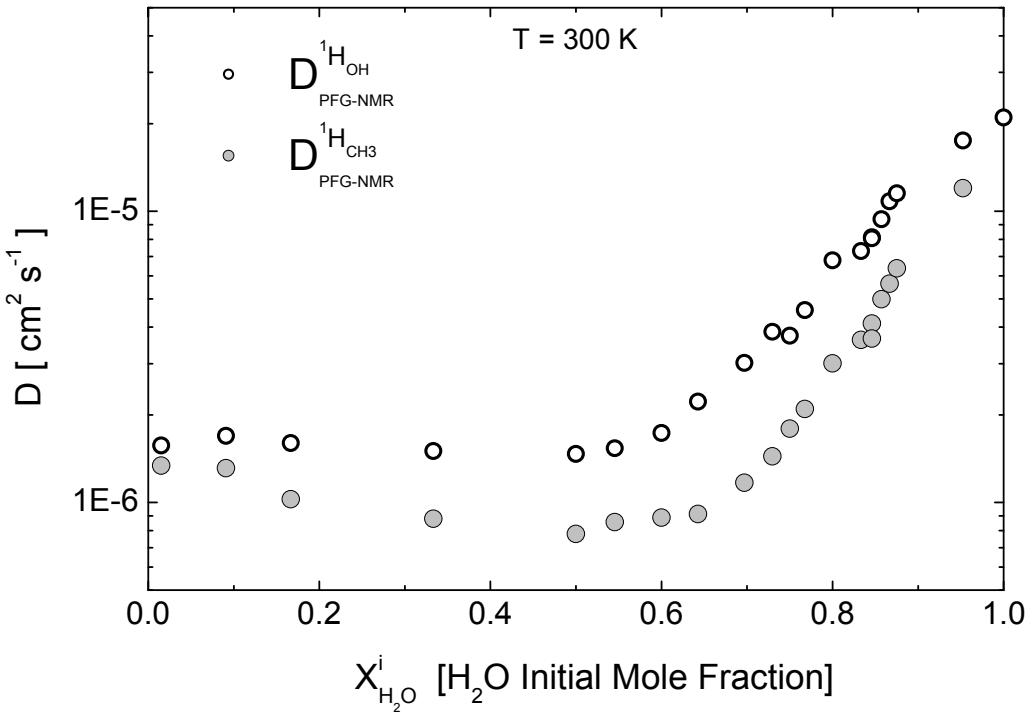

Figure 5-14: *Diffusion coefficients of ^1H in OH and CH_3 groups versus initial water mole fraction taken by PFG-NMR at room temperature.*

5.1.4 Proton Conductivity Mechanism

- **Protonic Conductivity of MSA-Water Mixtures**

MSA is a very strong acid (see Chapter 5.1.2), but because of the instability of $CH_3SO_3H_2^+$ its amphoteric properties are very weak. Therefore, the degree of self dissociation ($CH_3SO_3H + CH_3SO_3H \rightleftharpoons CH_3SO_3H_2^+ + CH_3SO_3^-$) is very low, and, as a consequence, also the ionic conductivity of dry MSA is low.[112] But with the addition of water, the concentration of charge carriers increases (Figure 5-6) and so does the ionic conductivity (Figure 5-15).

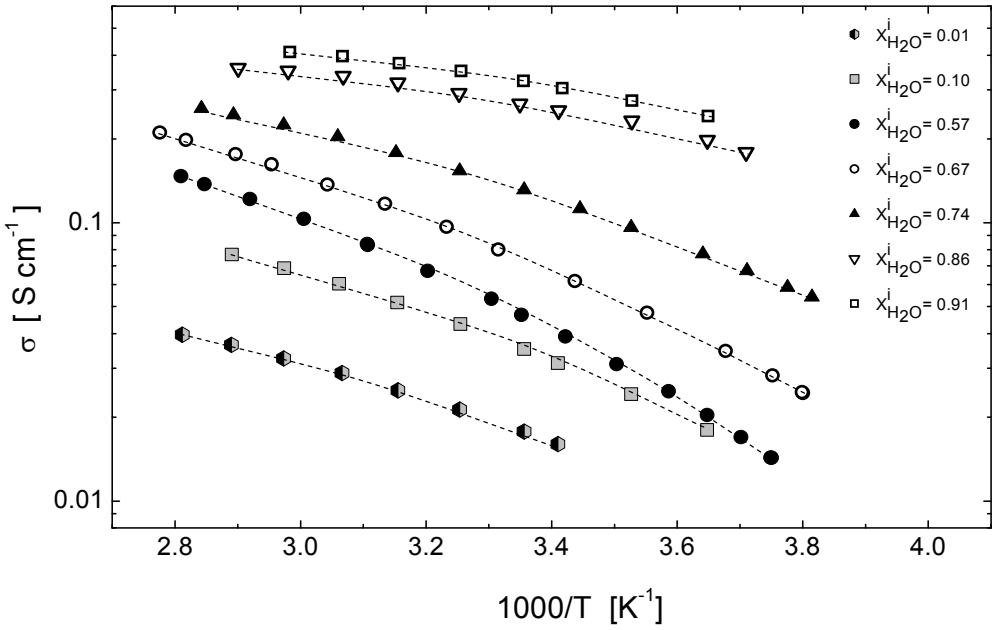

Figure 5-15: *Temperature dependent electrical ionic conductivity data versus initial water mole fraction obtained by AC-impedance spectrometer*

Since the ionic conductivities have been measured over a wider temperature range than the proton diffusion coefficients, the non-Arrhenius behaviour, which is typical for the transport of water based systems, is clearly visible. Because of its complexity, a quantitative analysis of the curvatures is not possible at this stage, but the data allow for a few qualitative conclusions.
The fact that for the highest water content ($X^i_{H_2O}$=0.91), at which the dissociation of MSA is virtually complete and therefore temperature independent, still some curvature is observed suggests, that the non-

Arrhenius behaviour has some contributions from the temperature dependence of the mobility of the charge carriers. It should be noted that the temperature dependence and even the absolute numbers of H_{CH_3} and H_{OH} diffusion are very close (Figure 5-12) , which also suggests similar mobilities for cations and anions in the complete temperature range. But in addition, the increasing curvature of the conductivity data with decreasing water content, suggests also some non-Arrhenius temperature dependence of the charge carrier concentrations. Charge carrier concentrations, which are decreasing with increasing temperature, are suggested by the average activation enthalpies (obtained by linearization) which are systematically lower than the activation enthalpies for proton diffusion (Figure 5-16). But such behaviour may also be the result of the presence of a conduction process (e.g. structure diffusion) which may have different temperature dependence than the hydrodynamic processes.[113,114,115]

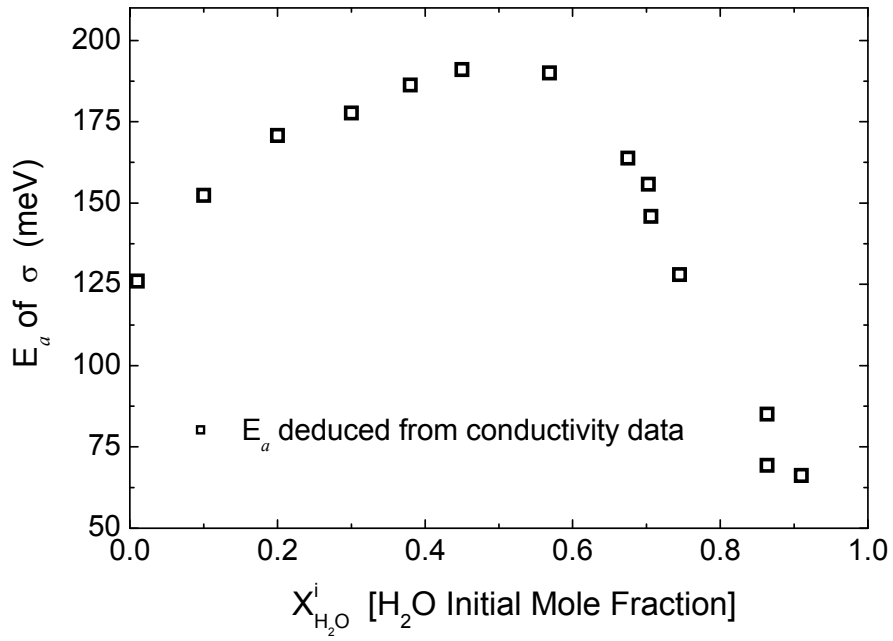

Figure 5-16: *Activation energies obtained from the temperature dependent conductivity measurements versus initial water mole fraction.*

Whether this is the case, can be answered at least for room temperature, at which charge carrier concentrations as a function of water contents are

available from the analysis of high resolution NMR data (see Chapter 5.1.2 and Figure 5-6 therein).

- **Proton Conduction Mechanism of MSA-Water Mixtures**

In the following, the question is addressed whether the ionic conductivity of MSA-water mixtures is simply of vehicle-type or whether structure diffusion of protonic defects has a relevant contribution to the total conductivity. With the concentration c_i of the charged species ($CH_3SO_3^-$ and H_3O^+, see Figure 5-6) and their diffusion coefficients D_i, the total conductivity may be calculated via the Nernst–Einstein relation ($\sigma = (F^2/RT) \sum_i z_i^2 c_i D_i$). For this, the diffusion coefficient of $CH_3SO_3^-$ has been assumed to be identical to this of $D(H_{CH_3})$ while the diffusion coefficient of H_3O^+ is assumed to equal $D(H_{OH})$. These assumptions are relying on the approximations that i) the diffusion coefficients of CH_3SO_3H and $CH_3SO_3^-$ are identical, that ii) the diffusion coefficient of CH_3SO_3H is smaller but not significantly smaller than the diffusion coefficients of the water like species and iii) that H_3O^+ and H_2O have virtually identical diffusion coefficients.

With these reasonable assumptions ionic room temperature conductivities have been calculated and compared to the corresponding experimental data.

The agreement is surprisingly good (Figure 5-17), i.e. the observed ionic conductivity can simply be explained by the mobilities of $CH_3SO_3^-$ and H_3O^+, which are present in high concentrations. In particular no inter-molecular proton transfer, typical for structure diffusion, has to be included into the description of the total ionic conductivity. This is also supported by the observation that Γ_1 of the ^{1}H-NMR and the diffusion coefficients of all species show very similar behaviour as a function of the water volume fraction and temperature (see above). In particular, there is no indication of a decoupling of the proton dynamics from this of the other species.

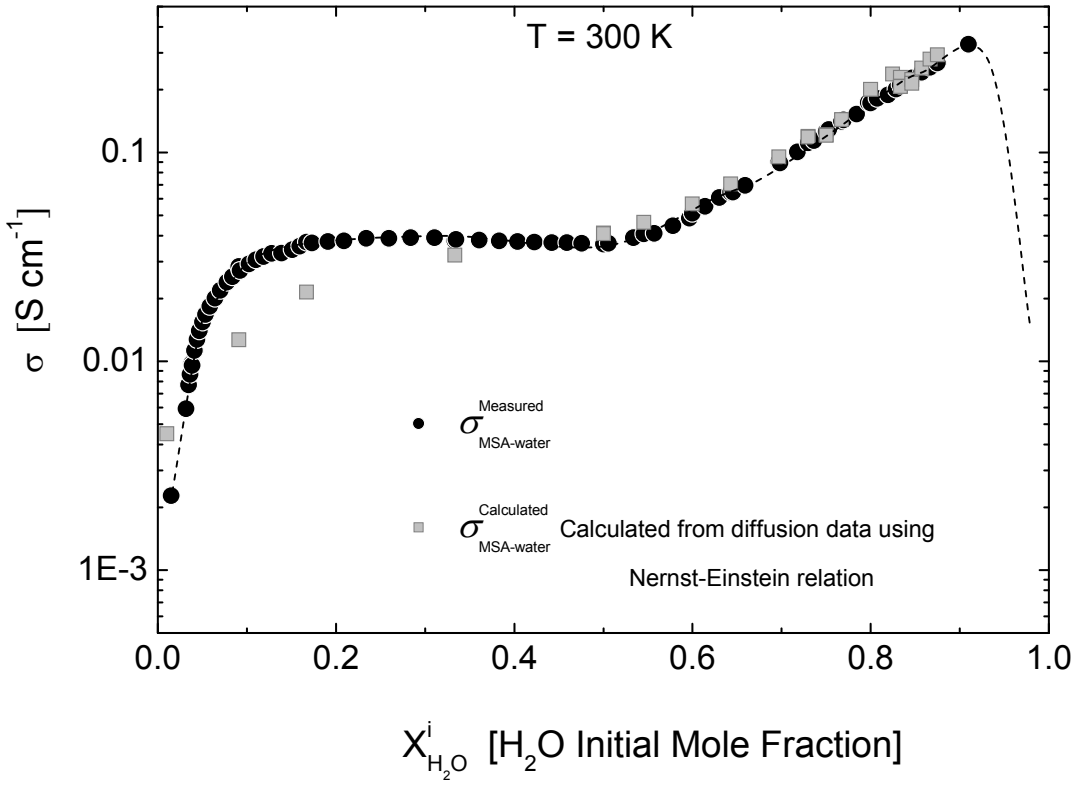

Figure 5-17: *Experimental data of electrical conductivity σ obtained by AC-impedance analyzer and the calculated data of the conductivity from the mass transportation σ_D (obtained by PFG-NMR diffusion) at room temperature. The dotted line is drawn to guide the eyes and it has no theoretical significance.*

It should be noted that the small deviations for low water mole fractions are within the error bars, which are particularly high in this range (uncertainty of charge carrier concentrations), and that for very high water contents, which have not been examined in this work, structure diffusion must come into play like for the dilute aqueous solution of any acid.

The important message at this point is that the total ionic conductivity of MSA-water mixtures is fully explained by assuming vehicle mechanism for the protonic contribution for any water volume fraction smaller than $X^i_{H_2O} = 0.9$.

6 Summary and Conclusions

The present thesis presents insight into the formation and mobility of protonic charge carriers in mixtures of methyl-sulfonic-acid (MSA) and water. The system has been chosen as model for proton conducting ionomers with sulfonic acid functionalisation, which are commonly used as separator material in polymer electrolyte membrane (PEM) fuel cell. Since the model system provides the highest possible concentration of sulfonic acid groups, the situation is expected to be optimum for obtaining high proton conductivity at low water contents. Therefore, the measured proton conductivities are considered to define an upper limit for the proton conductivity of any sulfonic acid functionalized ionomer, and the details of the conduction mechanism are expected to also hold for any ionomer of this type.

Especially the conductivity at low water content is of particular interest, because of the current trend to operate PEM fuel cells at higher temperature and lower relative humidity. This work was also be inspired by the observation that the proton conductivity of heptyl-sulfonic acid (S-C7, Figure 6-1) decreases with decreasing water content (as observed for any sulfonic acid functionalized ionomer), but for very low water contents ($\lambda \sim 0.5 - 1.5$) proton conductivity had been found to be virtually independent of the water content. This unexpected observation had been raising questions about a possible change of the proton conduction mechanism in this humidity range, which could become a basis for the development of sulfonic acid based ionomers with high proton conductivity at low humidification.

The present work provides a clear rational for the conductivity behaviour at low humidification. The conductivity "plateau" (Figure 6-1) observed at low λ-values is just the result of two compensating effects: a decrease of the concentration of protonic charge carriers and an increase of the molecular diffusion coefficient and mobility of charged molecular species with decreasing water content. The first has been determined from the NMR chemical shift of the chemically different protons and the latter by PFG-NMR and ac-impedance spectroscopy as a function of the water content. The "plateau" region is therefore just a signature of the transition from a situation

where the system is completely dissociated (ionic regime) to a situation where the sulfonic function is almost undissociated (molecular regime). One of the key results of this work is the volume density of protonic charge carriers (H_3O^+) as a function of the water content (Figure 6-1). This passes through a maximum which coincides with the centre of the "plateau" region. At this point, the water diffusion coefficient and the mobility of protonic charge carriers pass through a minimum (Figure 6-1).

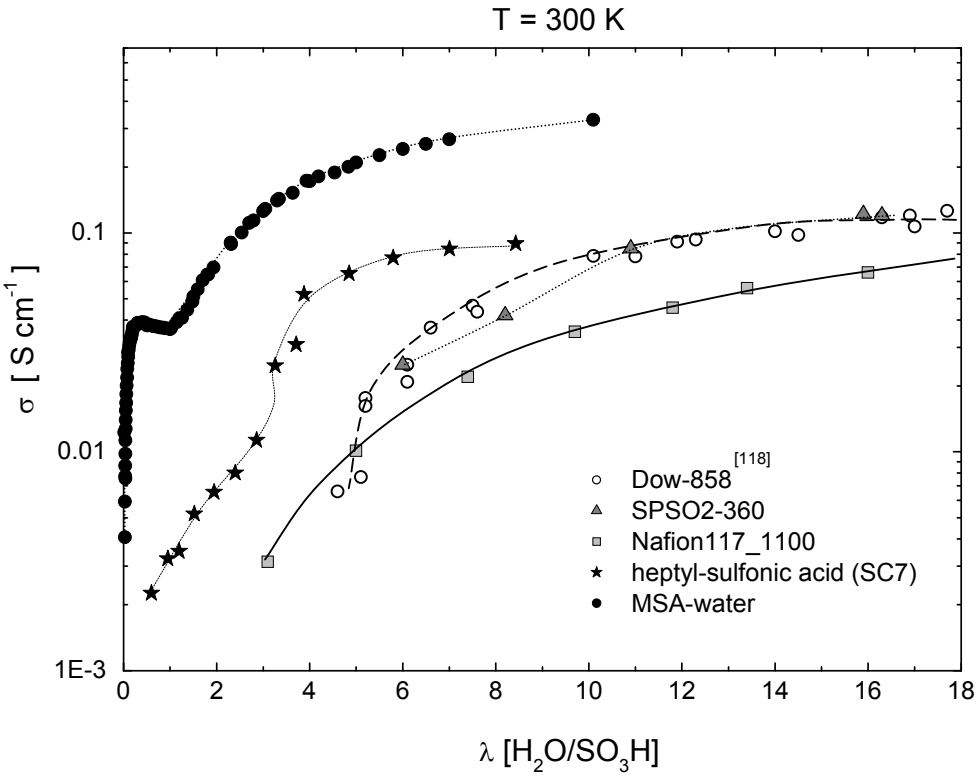

Figure 6-1: *Total room temperature conductivity of MSA-H_2O, heptyl-sulfonic acid (S-C7) and three state of the art ionomers as a function of the water content λ.*

These findings point towards the importance of electrostatic interactions and provide a rational for other experimental findings. The elastic modulus of hydrated sulfonic-ionmers increases with decreasing water content, which is generally attributed to the plasticizing effect of water. But recently F. Bauer[116] reported a drastic decrease of the elastic modulus of Nafion for water contents below λ~1.5. In the light of the present finding this may be

understood as a consequence of the drastically decreasing number of protonic charge carriers. These are most likely mediating electrostatic interactions between sulfonic acid anions immobilized on different polymer strands, which reaches its maximum around λ= 1.5. An increase of the water content then just dilutes the charge carriers, while a decrease of the water content reduces their concentration by decreasing the dissociation. In the case of the system MSA-H_2O investigated in this work, the maximum of the electrostatic interaction corresponds to the minimum of molecular diffusion and presumably to a maximum of the viscosity.

It is worth noting that the conductivity in this regime is fully explained by the mobility of H_3O^+ and $CH_3SO_3^-$ (vehicle mechanism). Only at extremely low water content (x < 0.2), proton mobilities obtained form conductivity measurements were somewhat higher than molecular diffusion coefficients which may indicate some proton transfer between the different species of the system (H_3O^+, H_2O, $CH_3SO_3^-$). But insecurities in the determination of the absolute water content and the determination of the dissociation constant may account for this finding.

At high water contents (λ > 10) the conductivities of the best conducting ionomers (such as Nafion, Dow-858, sulfonated polysulfone (S-SPP-360)) are only a factor of 3-5 lower than the conductivity of MSA-H_2O (Figure 6-1) which is fully explained by the lower concentration of acidic groups. In particular, there is no indication for significant geometrical restrictions of proton conductivity and water transport in these systems. But for lower water contents (λ< 10), the proton conductivity of ionomers decreases more rapidly than this of the MSA-H_2O system (Figure 6-1). This is definitely the regime, where percolation effects (geometrical restrictions) come into play, but there may be other effects which have to do with the fact that an increasing part of the water is forced into close contact with the hydrophobic polymer backbone. Within the framework of this thesis, it was also attempted to examine the effects on dissociation and diffusion, by simply substituting part of the water by higher alcohols (ethanol, isopropanol). So far, the accuracy of the measured chemical shift data (Figures 3-4, appendix) is not sufficient

to determine the dissociation constant of MSA in this environment, but the diffusion (Figures 5, appendix) and conductivity behaviour (Figures 6, 8, appendix) provide clear evidence for a significantly reduced MSA dissociation as a result of the addition of alcohol. While the average solvent (water / alcohol) diffusion coefficient is decreasing by a factor of two at the most, the total conductivity decreases by up to a factor of 15. Therefore, the decrease of the proton conductivity of ionomers at low water contents may be also the consequence of a decreasing degree of dissociation. Provided this is the case, the "plateau" regime observed in the conductivity of MSA-H_2O may be more spread and shifted to somewhat higher water contents in the case of ionomers.

In any case, it is clear that the conductivity of state of the art ionomers may be increased by increasing the concentration of acidic groups. While only linear effects are expected for high water contents, the conductivity increase at low humidification may be more pronounced, because both percolation effects and the effects of hydrophobic interaction are expected to be reduced, while the charge carrier concentration is increased. But it should also be noted, that the increased charge carrier concentration generally reduces the mobility of all species, but usually to a lower extend than the increase of the charge carrier concentration.

To be more specific, the water uptake of available ionomers (Figure 13, appendix) may provide an idea of the maximum possible conductivities. At a water pressure of p_{H2O} = 1 atm (which may be considered to be an upper limit in a fuel cell), the water uptakes at T = 110 and 140°C are λ= 6 and 3 respectively. For these two conditions, the conductivity of MSA-H_2O is somewhat higher than 0.4 and 0.2 S cm^{-1} (Figure 11, appendix). Based on above discussion, the conductivity of an ionomer of very high ion exchange capacity (concentration of sulfonic groups around 200 meq. g^{-1}) may be estimated to be a factor of four lower. Since conductivities around $5x10^{-2}$ to 10^{-1} S cm^{-1} are generally considered to be sufficient for fuel cell operation, the temperature limit for PEM fuel cells relying on the proton conductivity of

sulfonic acid based ionomers is therefore estimated to be in the range T = 110 - 140°C.

Considering maximum operation temperatures of state of the art PEM fuel cells around T = 80 - 90°C, this leaves still some space for optimization.

Finally it should be mentioned, that high proton conductivity is a key feature, but other properties such as morphological, chemical and electrochemical stability have to be considered as well.

Appendix

As a complementary for this work we have investigated MSA-water-alcohol (ethanol, isopropanol) systems as a comprehensive model system in order to fully interpret the diffusivity and the protonic conductivity in real fuel cell membranes.

Real sulfonated fuel cells membranes (Nafion117-1100, Dow-858, and $SPSO_2$-360) have been studied in the field of conductivity as a function of temperature under full water pressure. The data are shown in the following appendix.

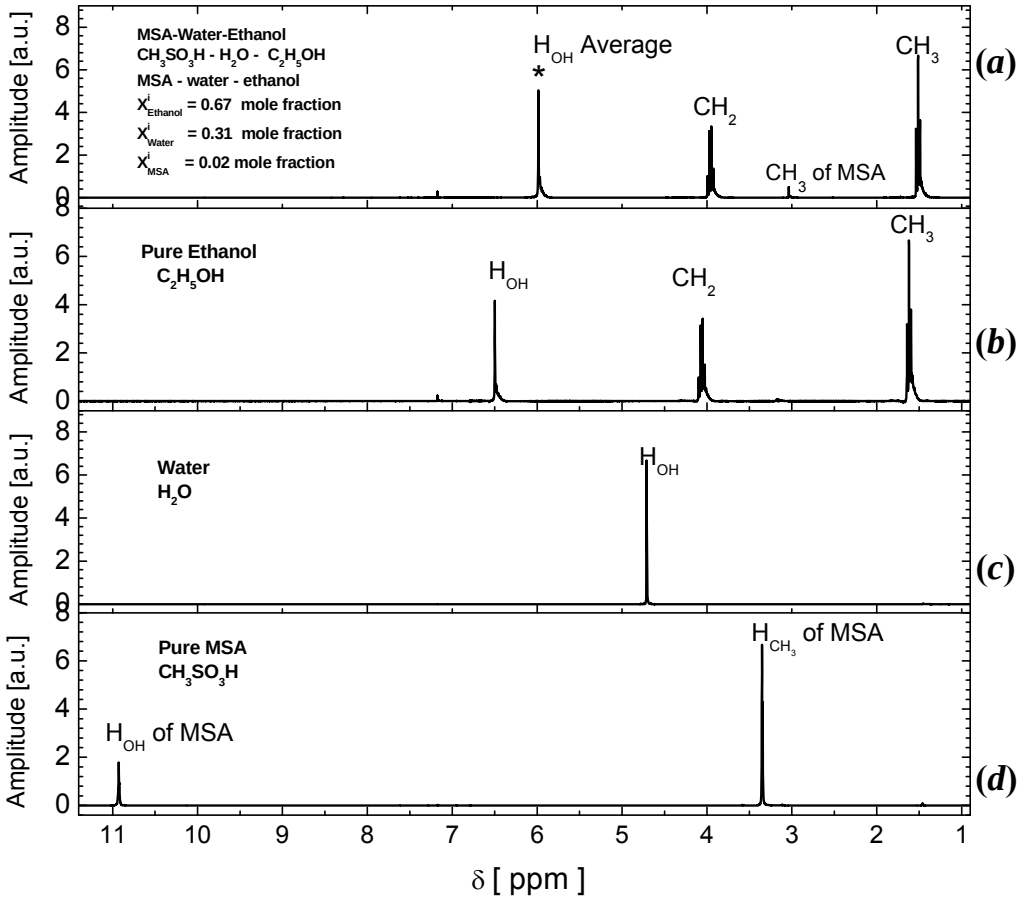

Figure App.-1: *300 MHz High resolution NMR spectra at room temperature for (**a**) MSA-water-ethanol ($X^i_{MSA} = 0.02$, $X^i_{water} = 0.31$, $X^i_{ethanol} = 0.67$) mole fraction (**b**) pure ethanol (**c**) pure water (**d**) pure MSA.*

(*)The fast exchange between the protons in OH group of MSA, water and ethanol leads to a single $H_{(OH)}$ -NMR line in the NMR spectrum.[117,118]

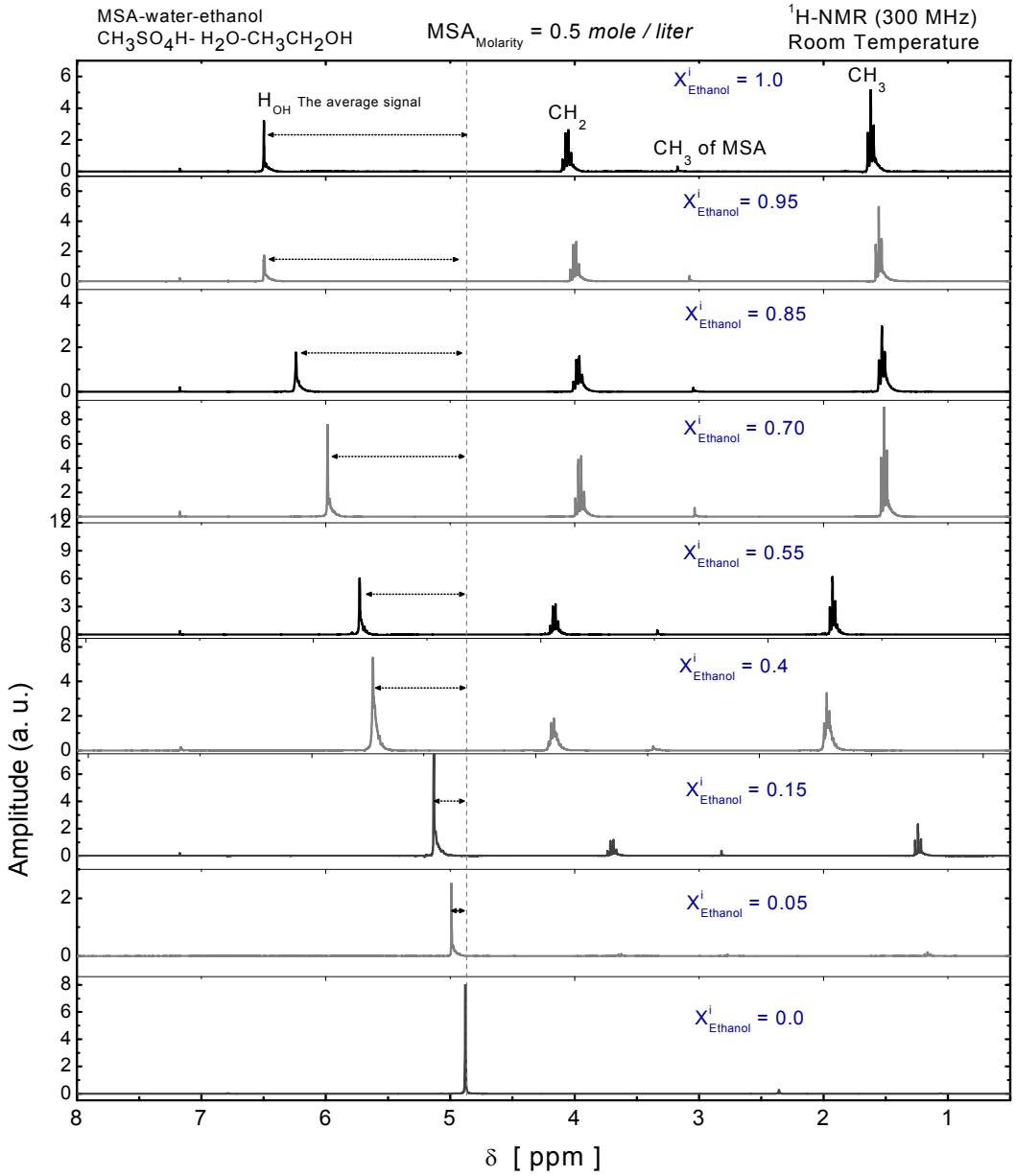

Figure App.-2: *High resolution ^{1}H-NMR spectra of a MSA-water-ethanol at room temperature and 300 MHz NMR frequency. The MSA concentration is 0.5 mole/liter and it is constant in all samples. Ethanol mole fraction has been varied from 0 to around 1 mole fraction.*

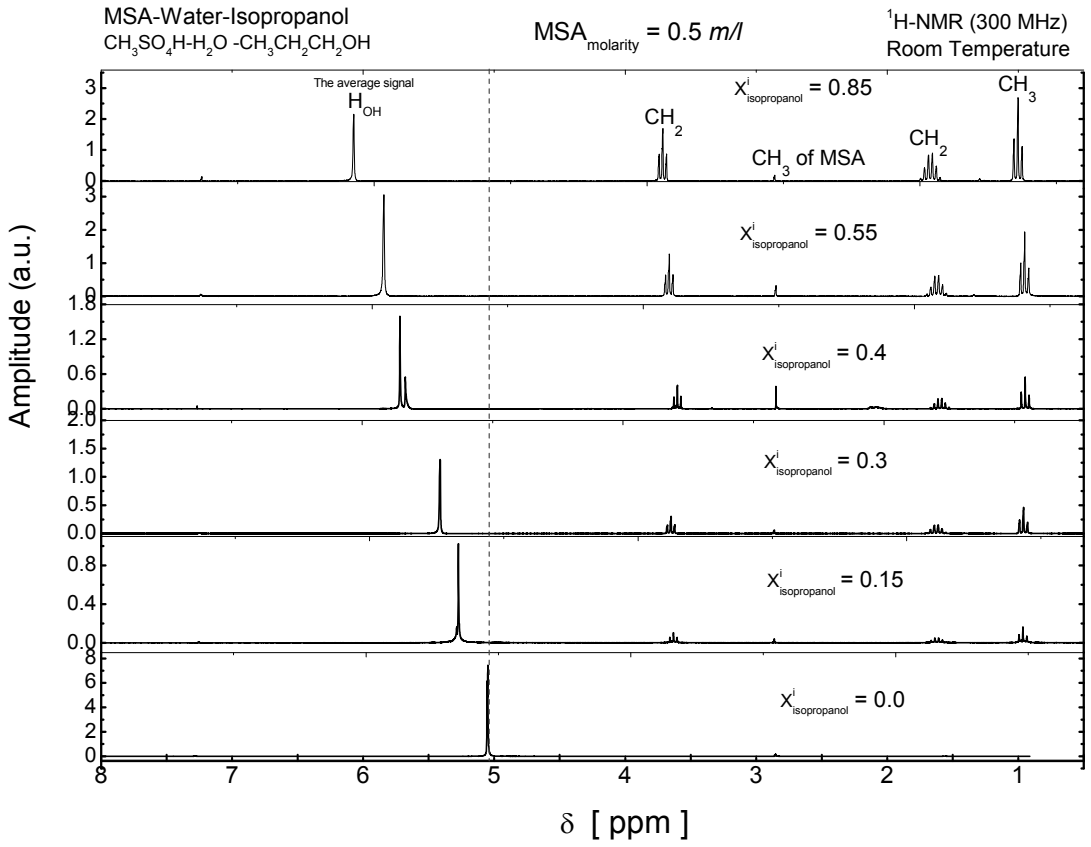

Figure App.-3: *High resolution ^{1}H-NMR spectra of a MSA-water-isopropanol at room temperature and 300 MHz NMR frequency. The MSA concentration is 0.5 mole/liter and it is constant in all of the samples. Ethanol mole fraction has been varied from 0 to almost 1 mole fraction.*

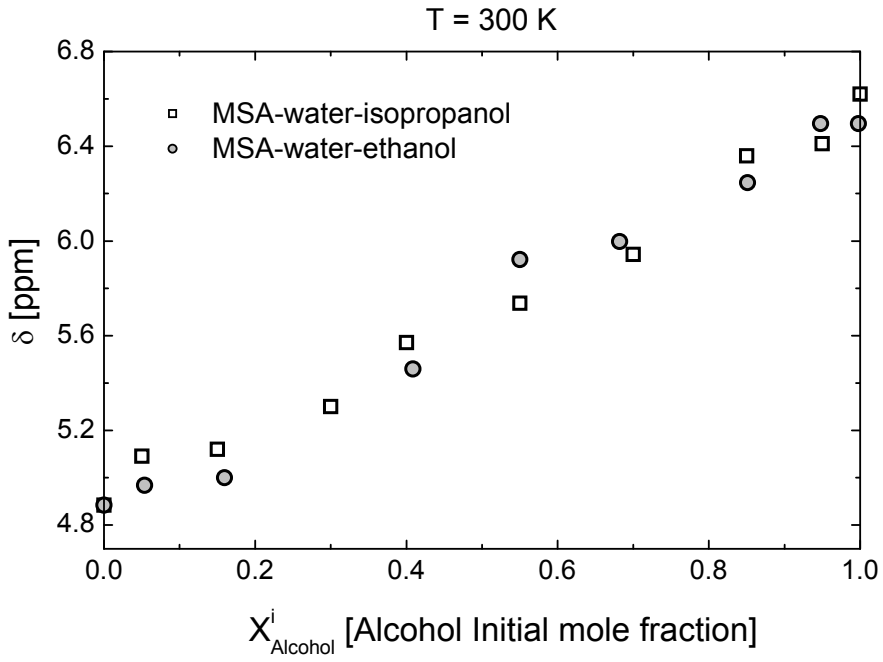

Figure App.-4: *Chemical shifts of H_{OH} in MSA-water-ethanol and MSA-water-isopropanol mixtures versus alcohol initial mole fraction.*

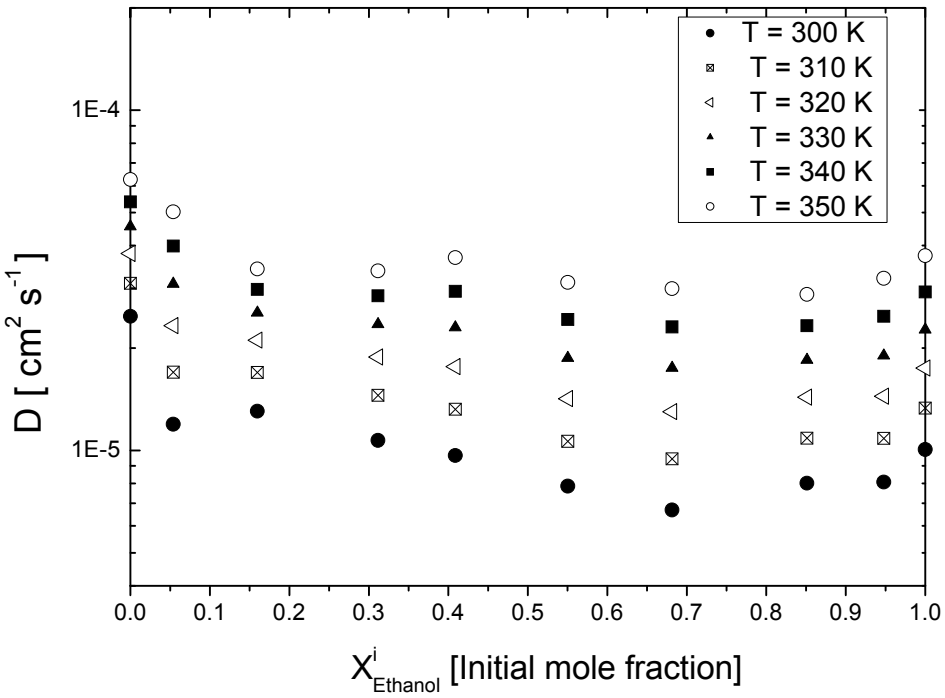

Figure App.-5: *Diffusion coefficients of H_{OH} in MSA-water-ethanol mixtures versus initial ethanol mole fraction for several temperatures. The MSA concentration is 0.5 mole/liter and it is constant in all samples.*

The uncertainty in these measurements is ranging between 4 to 12 percent, the error bars are not drawn for clarity.

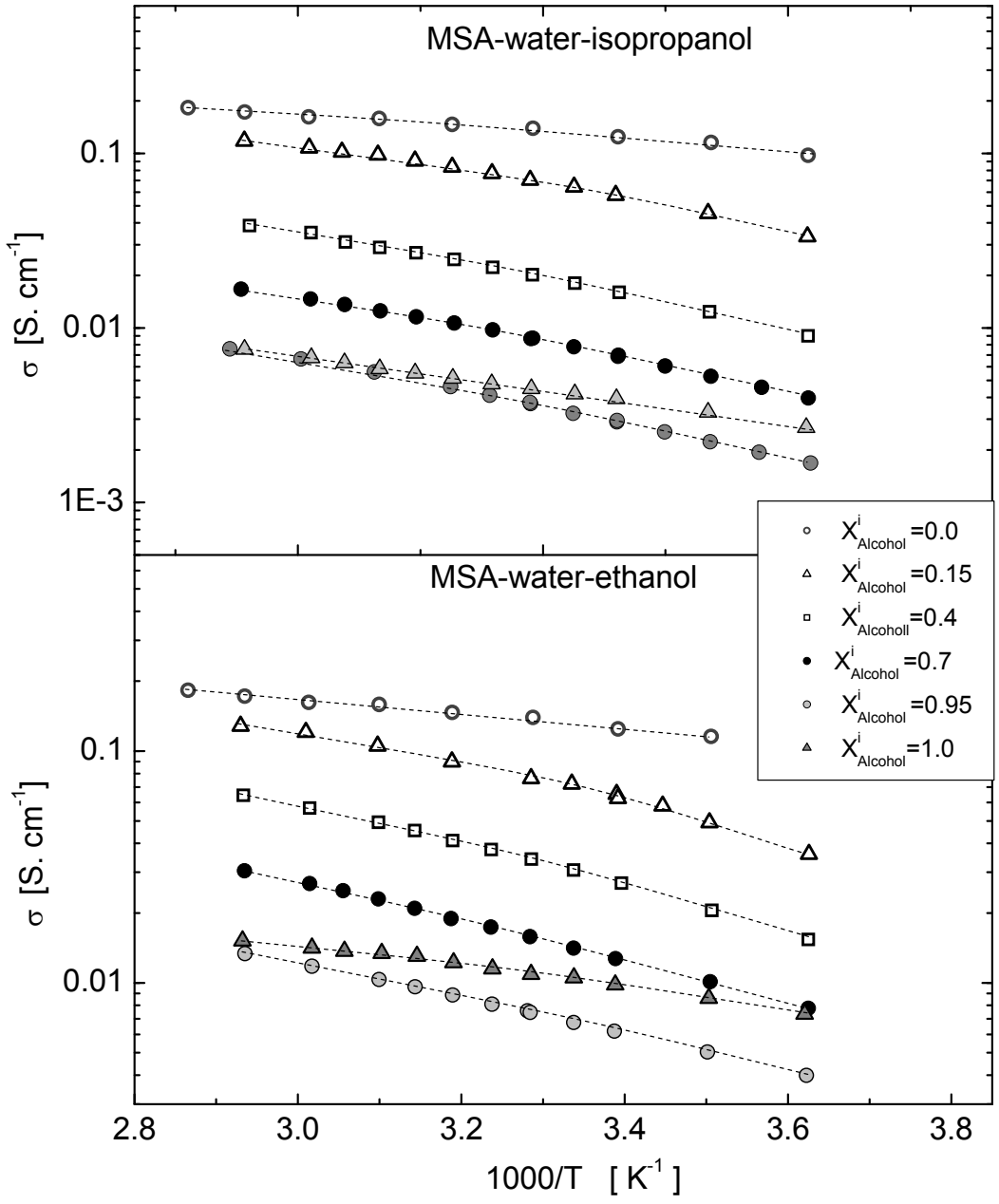

Figure App.-6: *Temperature dependent electrical conductivity of MSA-water-(ethanol, isopropanol) samples, the samples are with different alcohol initial content. MSA initial concentration is 0.5* mole/liter*, and it is constant for all samples. The dotted lines are to guide the eye (no theoretical significance).*

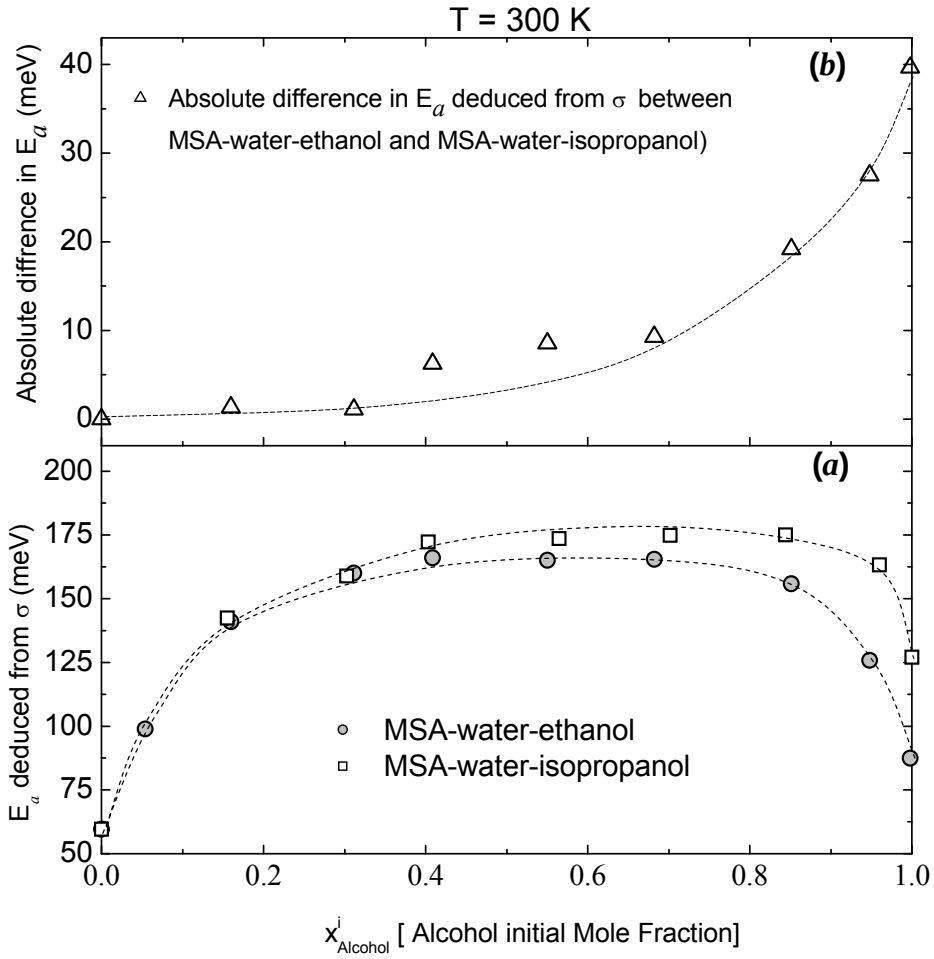

Figure App.-7: (a) *Activation energies deduced from the temperature dependent conductivity data for different samples with initial ethanol and isopropanol content. The results are ranging from 70 to190 meV. Both conductivity results of MSA-water in ethanol or isopropanol medium show the same trend.*

(b) *Absolute difference in E_a deduced from conductivity (σ) between MSA-water-ethanol and MSA-water -isopropanol.*

The dotted lines are to guide the eyes (no theoretical significance).

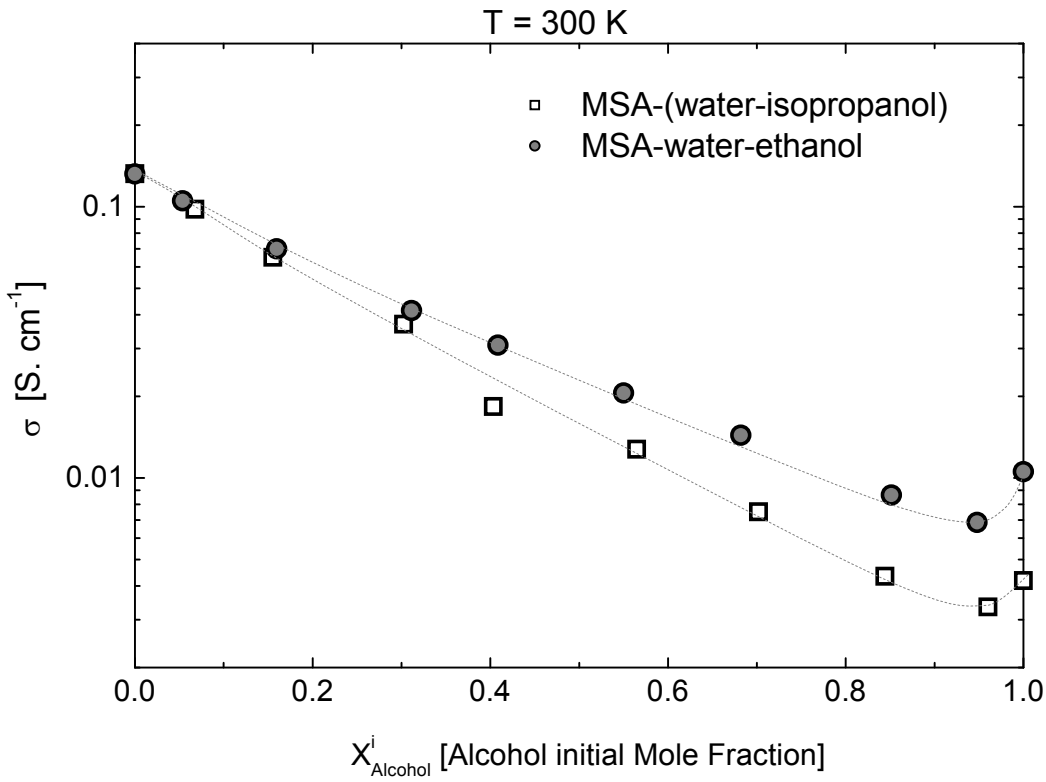

Figure App.-8: *Electrical conductivity of MSA-water-(ethanol, isopropanol) samples versus their initial mole fraction and at room temperature. MSA concentration 0.5 mole/liter. The electrical conductivity decreases with increasing alcohols concentration in both systems till 0.95 alcohol mole fraction and show an absolute minimum at 0.95 mole fractions. Furthermore the conductivity of MSA-water-ethanol shows higher values than the corresponding mixtures of MSA-water-isopropanol, Dotted lines are to guide the eyes (no theoretical significance).*

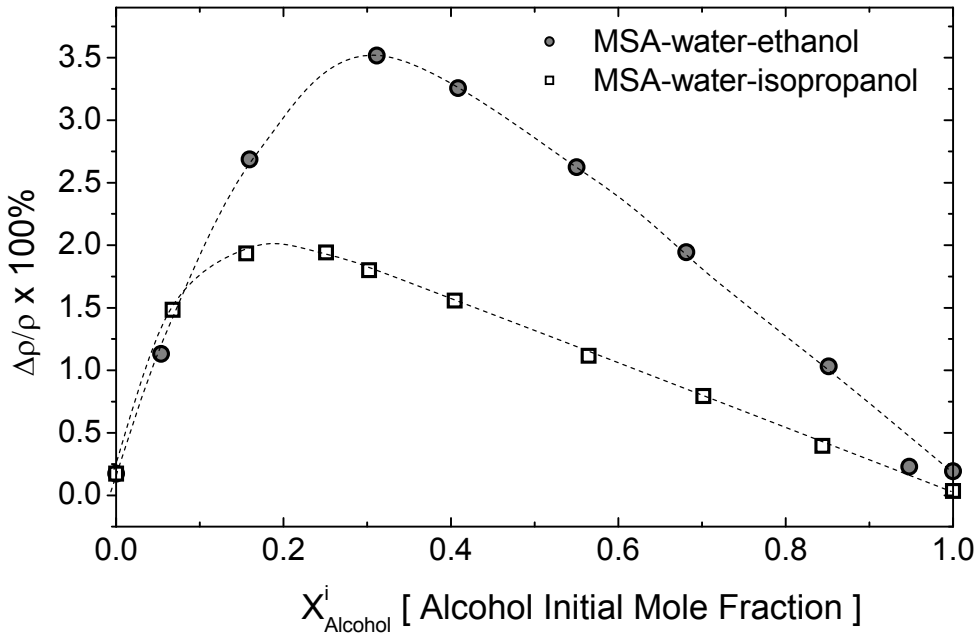

Figure App.-9: *The Relative difference between the experimental and the ideal mass density of MSA-water-(ethanol, isopropanol) samples versus their initial mole fraction at room temperature. MSA initial concentration 0.5 mole/liter.*
Dotted lines are to guide the eyes (no theoretical significance).

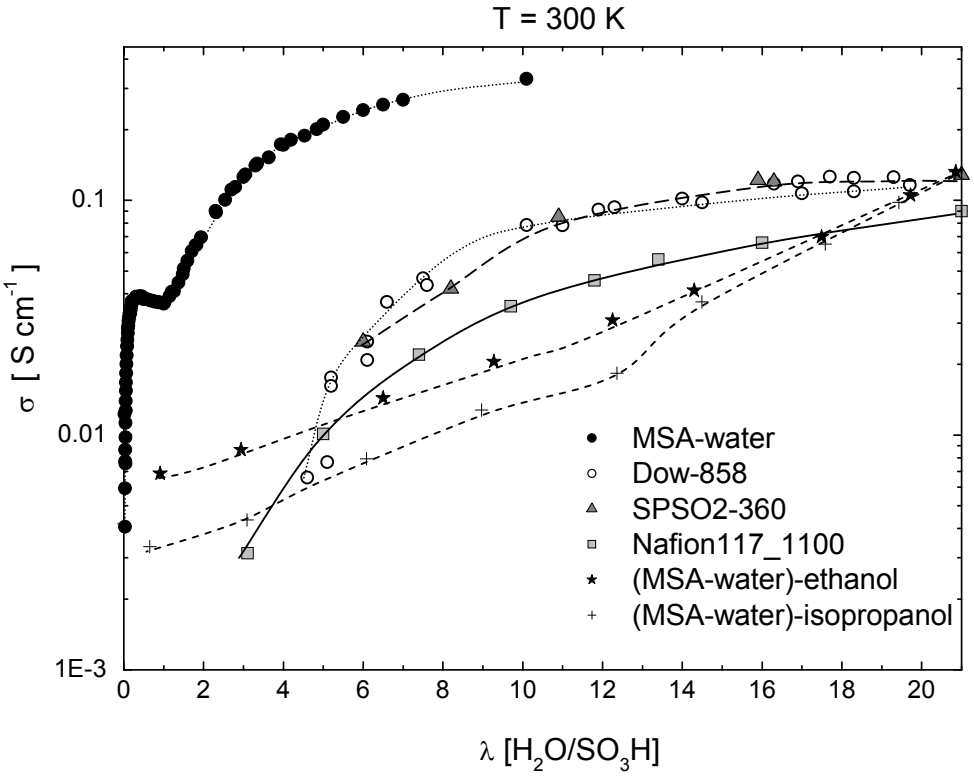

Figure App.-10: *Proton conductivity of DuPont's Nafion 117 (EW =1100 g/mol), SPSO2 (EW = 360 g/mol),*[119] *Dow (EW = 858 g/mol), and for MSA-water, MSA-water-ethanol and MSA-water-isopropanol systems at T = 300 K as a function of water content (λ).*

Alcohol-water solutions are considered as universal mixtures for theses measurements. Dotted lines are to guide the eyes (no theoretical significance).

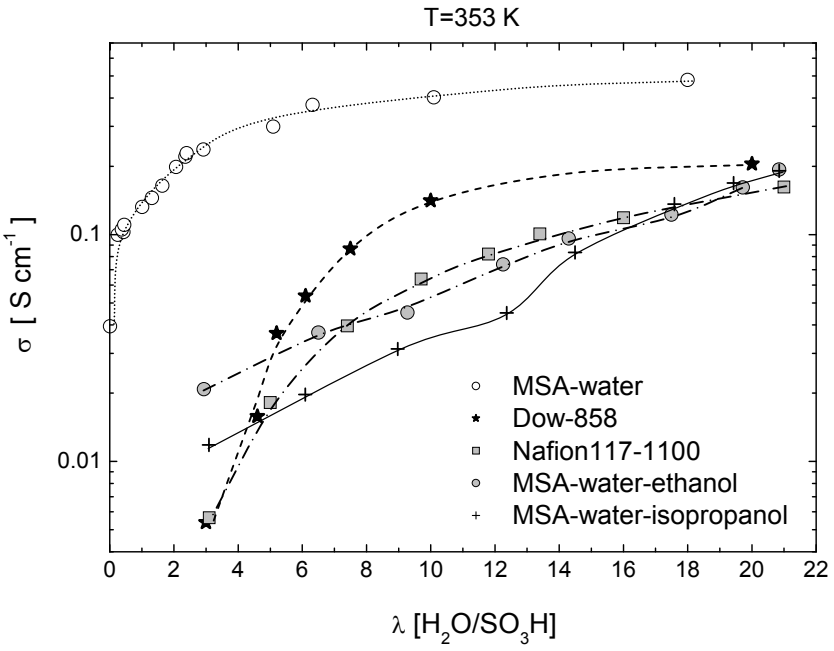

Figure App.11: *Proton conductivity of DuPont's Nafion117 (EW =1100 g/mol), Dow (EW = 858 g/mol)[119], and for the elementary and complementary model systems at T = 353 K as a function of water content λ [H_2O/SO_3H]. Alcohol-water solutions are considered universal mixtures for theses measurements. Dotted lines are to guide the eyes (no theoretical significance).*

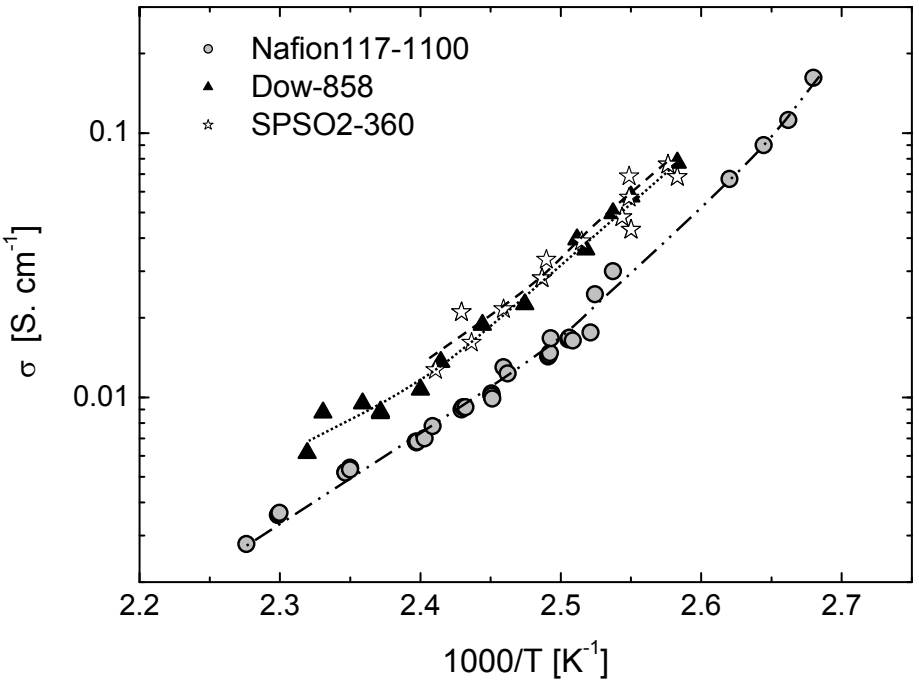

Figure App.-12: *Protonic conductivity of DuPont's Nafion117-1100 , Dow-858 and $SPSO_2$-360 samples, as a function of temperatures at full water pressure 1 atm Some of the data of $SPSO_2$-360 sample are partially published in ref.[119]. Dotted lines are to guide the eyes (no theoretical significance).*

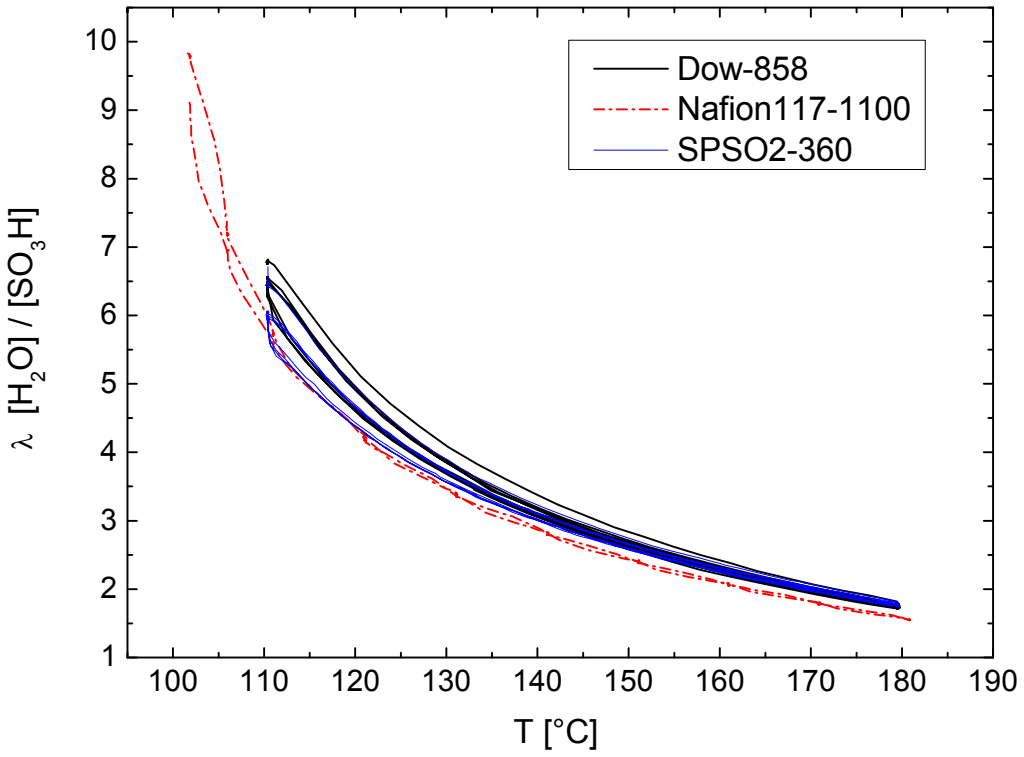

Figure App.-13: *Water molecules per sulfonic acid group content of DuPont's Nafion-1100, Dow-858 and $SPSO_2$-360 samples, as a function of temperatures at full water pressure 1 atm (10^5 Pa). TGA measurement has been also performed In order to ensure the stability of physiochemical properties these real membranes by performing several heating and cooling cycles, during theses heating cycles the water uptake is measured. Reproducibility of water uptake cycles and the origin mass of the polymer body can judge the stabilization of the membrane*.

References

[1] M. F. Mathias, R. Makharia, H. A. Gasteiger, J. J. Conley, T. J. Fuller, C. J. Gittleman, S. S. Kocha, D. P. Miller, C. K. Mittelsteadt, T. Xie, S. G. Yan, and P. T. Yu, Electrochem Soc. Interface, **14** (3) 24 (2005).

[2] R.K.A.M. Mallant. J. Power Sources **118**, pp. 424–429 (2003).

[3] M. Schuster, T. Rager, A. Noda, K.D. Kreuer, J. Maier, *Fuel Cells* (2005), online av.

[4] K.D. Kreuer, S.J. Paddison, E. Spohr, M. Schuster, *Chem. Rev.* **104**, 4637 (2004).

[5] H.E. Draling, *J. Chem. Eng. Data*, **9**, 421 (1964).

[6] H. J. V. Tyrell and K. R. Harris, *"Diffusion in Liquids: A Theoretical and Experimental Study"*, First Ed. Butterworths Monographs in Chemistry, Butterworths & Co Ltd, London, England, 1984, 448.

[7] R. S. Macomber, *"A Complete Introduction to Modern NMR Spectroscopy".* ISBN 0-471-15736-8 (1997).

[8] A. Abragam, *"The Principles of Nuclear Magnetism"*, Oxford University Press London (1985).

[9] J. B. Lambert and Eugene P. Mazzola, "Nuclear Magnetic Resonance Spectroscopy an Introduction to Principles", ISBN: 0130890669, 2002.

[10] C.P. Slichter, "*Principles of Magnetic Resonance*", Harper & Row, New York (1963).

[11] Thomas L. James, "*Fundamentals of NMR*"*, Department of Pharmaceutical Chemistry University of California San Francisco, CA 94143-0446 U.S.A*.

[12] T. C. Farrar and E. D. Becker: "*Pulse and Fourier Transform NMR, Introduction to Theory and Methods*", (Academic Press, New York and London, 1971).

[13] Malcolm H. Levitt, "*Spin Dynamics: Basics of Nuclear Magnetic Resonance*"*,* ISBN: 978-0-470-51118-6, 2007.

[14] J. Keeler, "*Understanding NMR Spectroscopy*", John Wiley & Sons, Chichester, ISBN 0470017872, 2005.

[15] R. G. Barnes, in *Hydrogen in Metals III*, edited by H. Wipf (Springer, Berlin, Heidelberg, 1997), p. 93.

[16] J. Korringa, Physica (Utrecht) **16**, 601 (1950).

[17] T. –T. Phua, B. J. Beaudry, D. T. Peterson, and D.R. Torgeson. Phys. Rev. *B.* **28**, 6227 (1983).

[18] N. Bloembergen, E. M. Purcell, R. V. Pound Physical Review **73**, 679 (1948).

[19] J. Bardeen, C. Herring "*Imperfections in Nearly Perfect Crystals*" ed. W. Shockley, Wiley New York (1952).

[20] J. R. Klauder and P. W. Anderson, Phys. Rev., **125**, 3, 912–930 (1962).

[21] C. Kittel, "*Introduction to solid state physics*", 7th ed. (1996).

[22] G. Alefeld and J. Voelkl. "*Topics in Applied Physics- Hydrogen in metals I*", vol. **28**, (1978).

[23] H. S. Gutowsky and B. R. McGarvey, J. Chem. Phys. **20**, 1472 (1952).

[24] W. S. Price, "*Pulsed-Field Gradient Nuclear Magnetic Resonance as a Tool for Studying Translational Diffusion*", John Wiley & Sons, 299-336 (1997).

[25] E. Hawlicka, *Chem*. *Soc*. *Re*¨. **34**, 13743-13750 (1995).

[26] R. J. Hunter, *Foundations of Colloid Science*, Oxford University Press, Oxford, 1986.

[27] M. A. Lauffer, "*Motion in Biological Systems*", Alan R. Liss, New York, 1989.

[28] A. G. Marshall, Biophysical Chemistry Principles, Techniques, and applications, Wiley, New York, 1978.

[29] F. Bloch, *Phys. Rev.* **70 (7-8)**, 460-474 (1946).

[30] E. M. Purcell. H. C. Torrey and R. V. Pound. *Phys. Rev.* **69 (1-2)**, 37-38 (1946).

[31] E. L. Hahn, Phys. Rev. **80 (40)**, 580-594 (1950).

[32] J. Crank, "*The Mathematics of Diffusion*", Oxford University Pres, Oxford, 1975.

[33] C. S. Johnson Jr, University of North Carolina, Chapel Hill, NC, USA, "*Diffusion Measurements by Magnetic Field Gradient Methods*", 2007 John Wiley & Sons, Ltd..

[34] A. G. Avent, "*Spin Echo Spectroscopy of Liquid Samples in Encyclopedia of Nuclear Magnetic Resonance*", D. M. Grant and R. K. Harris, Eds. Wiley, New York, 4524-4530 (1996).

[35] E. L. Hahn, Phys. Rev. **80**, 580-594 (1950).

[36] E. O. Stejskal and J. E. Tanner, J. Chem. Phys. **42**, 288-292 (1965).

[37] E. O. Stejskal, J. Chem. Phys. **43**, 3597-3603 (1965).

[38] H. Y. Carr and E. M. Purcell, Phys. Re¨. **94**, 630-638 (1954).

[39] R. L. Vold and R. R. Vold, J. AmChem. Soc. **96**, 4043 (1974).

[40] R. L. Vold and R. R. Vold, Prog. Nucl. Magn. Reson. Spectrosc. **12**, 79 (1978).

[41] J. Kaerger, H. Pfeifer, and W. Heink, Adv. Magn. Reson. **12,** 1 (1988).

[42] M. I. Hrovat and C. G. Wade, J. Magn. Reson. **44,** 62 (1981).

[43] M. I. Hrovat and C. G. Wade, J. Magn. Reson. **45,** 67 (1981).

[44] C.H. Hamann, A. Hamnett, W. Vielstich, "*Electrochemistry*",Wiley-VCH, Weinheim, 1998.

[45] J. N. Butler with chapter by David R. Cogley, "*Ionic equilibrium solubility and ph calculations*", Wiley-Interscience (1998).

[46] W. G. Cummings and K. Torrance, "*Chemical analysis- electrochemical techniques*", Butterworths, London, chapter 17 (1992).

[47] Y. C. Wu and P. A. Berezansky, J. Res. Natl. Inst. Stand. Technol. **100**, 521 (1995).

[48] M. Abraham, and R. Becker, "*The Classical Theory of Electricity and Magnetism*", Hafner Publishing Company, Inc., 1949, 2nd ed, pp. 70-72.

[49] L. Onsager, J. Am. Chem. Soc. **58**, 1486 (1936).

[50] J. G. Kirkwood, J. Chem. Phys. **7**, 911 (1939);

[51] G. Oster, and J. G. Kirkwood, J. Chem. Phys. **11**, 175 (1943).

[52] E. L. Cussler, "*Diffusion: Mass Transfer in Fluid Systems*", Cambridge University Press (2003).

[53] R. Byron Bird , Warren E. Stewart , Edwin N. Lightfoot, "*Transport* Phenomena", John Wiley & Sons Inc (2001).

[54] A. J. Bard, L. R. Faulkner, "*Electrochemical Methods – Fundamentals and Applications*", 2nd Ed., Wiley, New York, chap. 4 (2001).

[55] P. Stilbs, "*Progress in NMR Spectroscopy*", ed. J. W. Emsley, J. Feeney and L. H. Sutcliffe (Pergamon Press, Elmsford, New York, 1987) Vol. 19.

[56] P.J. Gellings, and H.J.M. Bouwmeester, "*Handbook of Solid State Electrochemistry*", 1997 by CRC press, Inc.

[57] P. Atkins, Julio de Paula, "*Physical Chemistry for the Life Sciences*", co-published with Oxford University Press (2006).

[58] K.-D. Kreuer, "*Conduction Mechanisms in Materials with Volatile Molecules In: Proton conductors. Solids, membranes and gels - materials and*

devices", Ph. Colomban, ed., Cambridge University Press, Cambridge, 474–486 (1992).

[59] Th. Dippel and K.D. Kreuer, Solid State Ionics, **46**, 3 (1991).

[60] Th. Dippel, K.D. Kreuer and J.C. Lassègues, D. Rodriguez, Solid State Ionics **61,** 41- 46 (1993).

[61] Y. Marechal, *"The Hydrogen Bond and the Water Molecule: The Physics and Chemistry of Water"*, Elsevier B. V. (2007).

[62] G.R. Desiraju (Editor), Thomas Steiner, *"The Weak Hydrogen Bond: In Structural Chemistry and Biology"*, Oxford University Press Inc., New York (1999).

[63] Charles Tanford, *"The Hydrophobic Effect"*, John Wiley & Sons Inc. (1980).

[64] C. J. T. de Grotthuss, *Ann. Chim.* **58**, 54-74 (1806).

[65] S. I. Cukierman, Biochim. Biophys. Acta, Bioenerg. **1757**, 876-885 (2006).

[66] E. Gileadi, E. Kirowa-Eisner, *"Electrolytic conductivity the hopping mechanism of the proton and beyond"*, Electrochim. Acta ***51***, 6003-6011 (2006).

[67] D. J. Anick, J. Chem. Phys. **119**, 12442-12456 (2003).

[68] P. L. Geissler, C. Dellago, D. Chandler, J. Hutter and M. Parrinello, *Science* **291**, 2121-2124 (2001).

[69] H. J. Bakker and H.-K. Nienhuys, *Science* **297** 587-590 (2002).

[70] R. M. Pashley, M. Rzechowicz, L. R. Pashley and M. J. Francis, J. Phys. Chem. B **109**, 1231-1238 (2005).

[71] C. A. Wraight, Biochim. Biophys. Acta **1757**, 886-912 (2006).

[72] N. Agmon, Chem. Phys. Lett. **319**, 247-252 (2000).

[73] M. E. Tuckerman, D. Marx and M. Parrinello, Nature **417,** 925-929 (2002). M. E. Tuckerman, A. Chandra and D. Marx, *Acc. Chem. Res.* **39,** 151-158 (2006).

[74] P. L. Geissler, T. Van Voorhis and C. Dellago, *Chem. Phys. Lett.* **324,** 149-155 (2000).

[75] A. Botti, F. Bruni. S. Imberti, M. A. Ricci and A. K. Soper, *J. Mol. Liq.* **117,** 77-79 (2004).

[76] A. A. Kornyshev, A. M. Kuznetsov, E. Spohr and J. Ulstrup, *J. Phys. Chem. B* **107,** 3351-3388 (2003).

[77] J. Han, X. Zhou and H. Liu, *J. Power Sources* **161,** 1420-1427 (2006).

[78] U. Kaess, Ph.D. Thesis, Universität Stuttgart (1998).

[79] Th. Dippel, Ph.D. Thesis, Universität Stuttgart (1991).

[80] M. Hampele, Ph.D. Thesis, Universität Stuttgart (1989).

[81] J. Gottwald, Ph.D. Thesis, Universität Stuttgart (2001).

[82] XWIN-NMR, Version 2.5, Bruker Analytik (1998).

[83] XWIN-PLOT, Version 2.6, Bruker Analytik (1998).

[84] R. K. Harris and E. D. Becker, Journal of Magnetic Resonance **156,** 323–326 (2002).

[85] T. Rager, M. Schuster, H. Steininger, K.D. Kreuer, Adv. Mater. **19**, Issue 20, 3317-3321 (2007).

[86] D.T. Sawyer, A. Sobkowiak, J.L. Roberts, Jr., "*Electrochemistry for Chemists*", second edn., John Wiley & Sons, Inc., New York, 1995.

[87] J. Braunstein and G. D. Robbins, J. Chem. Educ. **48**, 52 (1971).

[88] H. P. Schwan, Ann. Biomed. Eng. **20**, 269–288 (1992).

[89] G. J. Janz and R. P. T. Tomkins, J. Electrochem. Soc. 124, 55C (1977).

[90] G. Jones and B. C. Bradshaw, J. Am. Chem. Soc. 55, 1780 (1933).

[91] S. L. Schiefelbein, Naomi A. Fried, Kevin G. Rhoads, and D. R. Sadoway, Rev. Sci. Instrum. **69**, 9, 3308-3313 (1998).

[92] S. Patai, Z. Rappoport, "*The Chemistry of Sulphonic Acids, Esters and their Derivatives*", John Wiley and Sons, New York, 1991, p. 251.

[93] V. D. Maiorov and N. B. Librovich, Seriya Khimicheskaya **7**, 1694-1697 (1991).

[94] D. Lee and K. Char, **18***,* 6445-6448 (2002).

[95] E. M. Arnett and G. Seorrano, Adv. Phys. Org. Chem.,**13**, 83 (1976).

[96] A. I. Serebryanskaya, P. A. Maksimova, and A. I. Shatenshtein, Zh. Org. Khim., **13**, 479 (1977).

[97] V. G. Khutsishvili, Yu. S. Bogachev, V. I. Volkov, A. I. Serebryanskaya, V. M. Kurenkova, N. N. Shapet'ko, S. F. Timashev, and M. L. Orman, Zh. Fiz. Khim., **57**, 2524 (1983).

[98] U. Leuchs and G. Lundel, Can. J. Chem., 58, 311 (1880).

[99] J. H. R. Clark and L. A. Woodward, Trans. Faraday Soc., 62, 2226 (1966).

[100] W. A. Proell, C. E. Adams, and B. H. Shoemaker, Ind. Eng. Chem., 40, 1129 (1948).

[101] B. G. Paul, K. K. Paul, and K. C. Melhotra, J. Chem. Soc., A. 2712 (1970).

[102] S. Li, W. Qian, F. Tai, Chemical Physics Letter **438**, 190-195 (2007).

[103] L. Wang, J.Phys. Chem. A **111**, 3642-3651 (2007).

[104] A. Givan, A. Loewenschuss, C.J Nielsen, J. Mol. Struct. **748**, 77-90 (2005).

[105] V. D. Maiorov and N. B. Librovich, Zh. Fiz. Khim., **11**, 2819 (1975).

[106] A. P. Kirilova, V. D. Maiorov, A. I. Serebryanskaya, N. B. Librovich, and E. N. Gur'yanova,*Izv. Akad. Nauk SSSR, Ser. Khim.*, 1986, 2435 [*Bull. Acad. Sci. USSR, Div. Chem. Sci.* **35**, 2226 (1986), (Engl. Transl.)].

[107] A. P. Kirilova, V. D. Maiorov, A. I. Serebryanskaya, N. B. Librovich and E. N. Gur'yanova, Russian Chemical Bulletin, **34**, 7 (1985).

[108] A. K. Covington and T. H. Lilley, Trans. Faraday Soc.,**63**, 1749 (1967).

[109] E.P. Serjeant and B. Dempsey, Editors, "*Ionization Constants of Organic Acids in Solution*", *IUPAC Chemical Data Series No. 23*, Pergamon Press, Oxford, UK (1979).

[110] K. K. Aligizaki , *"Pore Structure of Cement-Based Materials, Published 2005 Taylor & Francis"*, ISBN 0419228004.

[111] J. Kowalewski, Lena Mäler, "*Nuclear Spin Relaxation in Liquids, Published 2006 CRC Press"*, ISBN 0750309644.

[112] M. D. Gernon, Min Wu, Thomas Buszta and Patrick Janney, Green Chemistry, 127-140 (1999).

[113] W.L. Jorgensen, J. Chem. Phys. **77,** 4156 (1982).

[114] G.E. Walrafen, M.R. Fisher, M.S. Hokmabadi and W.-H. Yang, J. Chem. Phys. **85,** 6970 (1986).

[115] E.W. Castner Jr., Y.J. Chang, Y.C. Chu and G.E. Walrafen, J. Chem. Phys. **102,** 653 (1995).

[116] F. Bauer, S. Denneler, M. Willert-Porada, J. Polym. Sci. B: Polym. Phys. **43,** 786-795 (2005).

[117] C. J. Pouchert The Aldrich library of FT NMR spectra 2nd ed. Aldrich Chemical Co.: Milwaukee, 1983.

[118] J. D. Roberts, "*Nuclear Magnetic Resonance: Applications to Organic Chemistry*", McGraw-Hill: New York, 1959.

[119] M. Schuster, K.-D. Kreuer, H. T. Andersen, J. Maier, Macromolecules **40**, 598-607 (2007).

Acknowledgements

This thesis would not have been possible without the guidance and support of my advisors, colleagues and my family.

I send my most sincere gratitude to my advisors, who are both colleagues and friends, for their indispensable efforts and involvement. During my study, I received strong scientific guidance and academic support from my supervisor Priv. Doz. Dr. G. Majer. Gratitude also goes to my second supervisor Priv. Doz. Dr. K.-D.Kreuer and Prof. Dr. D. Schweitzer for kindly accepting to write an examiner's report. I extend my sincere gratitude and appreciation to Dr. M. Schuster for kindly providing guidance throughout the research and the thesis.

I thank Prof. J. Maier for accepting me as a member of his department and for all his support.

I am very grateful for the comments, advices and time given by Dr. Sarmimala Hore, Dr. Giuliano Gregori and Dr. Rotraute Merkle. Their helps have greatly improved and clarified this work.

My special thanks go also to Dr. Hanna Steininger, Dr. Britta Obliers and Dr. Carla de Araujo for the important scientific discussion.

The effort in technical help by Ms. Annette Fuchs and Mr. Udo Klock from Prof. Maier's group and Mr. Helmut Kammerlander from the glass technique workshop is also gratefully acknowledged.

I would like to make special mention about my mother and my father, who are the most important people in my life. And about my sisters and brothers who constantly provide emotional support and took care of me in many aspects.

I am especially grateful to my respected wife who always supports and motivates me to do the best in my work.

I also would like to acknowledge the Graduated College of Magnetic Resonance and the Max-Planck-Institute for offering me the highly scientific environment and research groups and for the generous financial support as well.

My acknowledgement would not be complete without expressing due regards and gratitude to my colleagues in Prof. Maier's department for their appreciated friendship and my colleague Ms. Laura Valiente.

Ahmad D.S. Telfah
May 2008

Curriculum Vitae

Name	**Ahmad** Deaf-Allah Saleem **Telfah**
Nationality	Jordanian
Date of birth	September 1st, 1973
Place of birth	Juhfieah – Irbid - Jordan
09/1980 - 07/1991	Schools
08/1996	*B.Sc. in Physics from* Yarmouk University Irbid-Jordan
01/2003	M.Sc. in Physics from Al al-Bayt University Al-Mafraq-Jordan *"Optical Properties of Thin Film Polyaniline Poly(methylmeth-acrylate) Blend Using Spectroscopic Ellipsometry* "
02/2004	M.Sc. in Physics from Stuttgart University (Max Planck Institute), Stuttgart-Germany *"Dynamical properties of hydrogen in metals hydride (YH_3, LuH_3)"*
06/2008	Ph.D. in Physics from Stuttgart University (Max Planck Institute), Stuttgart-Germany *"Transport of Protonic Charge Carriers in Methyl-Sulfonic-Acid / Water Mixtures: A Model for Lowly Hydrated Sulfonic Acid Based Ionomers"*

Publications

- H.A. Al-Attar, A.D. Telfah, *Optical constants of polyaniline /poly(methylmethacrylate) blen,* Optics Communications 229 (2004) 263–270.

- G. Majer, A. Telfah, F. Grinberg, and R. G. Barnes, *Unusual doublet structure in proton magnetic-resonance spectra of yttrium and lutetium trihydrides*, Phys. Rev. B 70, 134111 (2004).

- A. Telfah, , G. Majer, K.-D. Kreuer, M. Schuster, J. Maier, *Transport of Protonic Charge Carriers in Methyl-Sulfonic-Acid / Water Mixtures: A Model for Lowly Hydrated Sulfonic Acid Based Ionomers, the paper in preparation.*

Conferences

- Diffusion Fundamentals, 21st-24th of September 2005, Leipzig, Germany. (Poster session 'PFG-NMR Studies of Diffusion in Sulfonic Acid Based Systems').

- SSPC-13, 4th - 6th of September 2006, St Andrews, Scotland, UK. (Poster Session 'Transport of Protonic Charge Carriers in Methyl-Sulfonic-Acid / Water Mixtures: A Model for Lowly Hydrated Sulfonic Acid Based Ionomers').

Workshops, Summer-schools and Other Activities

- The 5th Workshop of the Graduate College of Magnetic Resonance in Würzburg, Germany, 6th - 8th of October 2003 (Oral Presentation '*Trihydrides of Yttrium and Luteium'*).

- The 6th Workshop of the Graduate College of Magnetic Resonance in Hirschegg, Austria. 14th - 18th of February 2004, (Oral Presentation '*NMR studies of hydrogen in yttrium and lutetium trihydrides*').

- The 11th Day of Magnetic Resonance, Stuttgart, Germany, 5th of April 2005.

- The 7th Workshop of the Graduate College of Magnetic Resonance in Hirschegg, Austria. 18th - 21st of September 2005, (Poster session '*PFG-NMR Studies of Diffusion in Sulfonic Acid Based Systems*').

- The 13th 'Day of Magnetic Resonance'- Stuttgart, Germany. 23rd of March 2006. (Invited speaker '*Transport Mechanism of Protonic Charge Carriers in Sulfonic Acid Based Systems*')

- Department Workshop at Schloss Ringberg. 12th - 14th March 2007. (Oral presentation '*Conductivity and NMR-Studies of* CH_3SO_3H - H_2O *Systems: A Model for Sulfonic Acid Based Proton Conducting Fuel Cell Membranes*').

- The 9th Workshop of the Graduate College of Magnetic Resonance in Bukowina Tatrzańska, Poland, AMPERE NMR Summer School, 24th-30th of June 2007. (Poster Session '*Conductivity and NMR-Studies of* CH_3SO_3H - H_2O *Systems: A Model for Sulfonic Acid Based Proton Conducting Fuel Cell Membranes*').

- Carisma School on "*Proton Transport Mechanisms*", joined with Carisma Workshop on "Ionomer Membranes for Medium and High Temperature PEM Fuel Cells", Stuttgart. 08th & 09th of November 2007 (school).